



**NAVAL
POSTGRADUATE
SCHOOL**

MONTEREY, CALIFORNIA

THESIS

**SIMULATION OF PERFORMANCE OF QUANTUM WELL
INFRARED PHOTODETECTORS**

by

Eftychios Psarakis

June 2005

Thesis Advisor:

Co-Advisors:

Gamani Karunasiri

James Luscombe

Robert Hutchins

John Powers

Approved for public release; distribution is unlimited

THIS PAGE INTENTIONALLY LEFT BLANK

REPORT DOCUMENTATION PAGE

Form Approved OMB No. 0704-0188

Public reporting burden for this collection of information is estimated to average 1 hour per response, including the time for reviewing instruction, searching existing data sources, gathering and maintaining the data needed, and completing and reviewing the collection of information. Send comments regarding this burden estimate or any other aspect of this collection of information, including suggestions for reducing this burden, to Washington headquarters Services, Directorate for Information Operations and Reports, 1215 Jefferson Davis Highway, Suite 1204, Arlington, VA 22202-4302, and to the Office of Management and Budget, Paperwork Reduction Project (0704-0188) Washington DC 20503.

1. AGENCY USE ONLY (Leave blank)	2. REPORT DATE	3. REPORT TYPE AND DATES COVERED
	June 2005	Master's Thesis
4. TITLE AND SUBTITLE: Simulation of Performance of Quantum well Infrared Photodetectors		5. FUNDING NUMBERS
6. AUTHOR(S) Eftychios Psarakis		
7. PERFORMING ORGANIZATION NAME(S) AND ADDRESS(ES) Naval Postgraduate School Monterey, CA 93943-5000		8. PERFORMING ORGANIZATION REPORT NUMBER
9. SPONSORING /MONITORING AGENCY NAME(S) AND ADDRESS(ES) N/A		10. SPONSORING/MONITORING AGENCY REPORT NUMBER
11. SUPPLEMENTARY NOTES The views expressed in this thesis are those of the author and do not reflect the official policy or position of the Department of Defense or the U.S. Government.		
12a. DISTRIBUTION / AVAILABILITY STATEMENT Approved for public release; distribution is unlimited		12b. DISTRIBUTION CODE
13. ABSTRACT (maximum 200 words) In this thesis the performance of a step quantum well infrared photodetector, designed by Kevin Lantz (June 2002) and experimentally studied by Michael Touse (September 2003) and Yeo Hwee Tiong (December 2004), was simulated in Matlab using the transfer matrix method. The results obtained by the Matlab program are compared with the experimental results in a try to make inferences about the optimum way of designing QWIP detectors. Simulation of the above implies numerical solution of the Schrödinger equation, using algorithms and methods, which give accurate results. In our approach, the transfer matrix method is used with exponential and, Airy functions to represent the solutions to Schrödinger equation under zero and non-zero bias, respectively. In the final section of the thesis we examine and simulate in Matlab the application of the extended Kalman filtering (EKF) to an infrared photodetector as a target tracking mechanism to both maneuvering and non-maneuvering targets.		
14. SUBJECT TERMS Asymmetric quantum well, Quantum well infrared photodetector under electric field, Absorption, Probability current, Transfer matrix method, BOT, EKF.		15. NUMBER OF PAGES 157
16. PRICE CODE		
17. SECURITY CLASSIFICATION OF REPORT Unclassified	18. SECURITY CLASSIFICATION OF THIS PAGE Unclassified	19. SECURITY CLASSIFICATION OF ABSTRACT Unclassified
20. LIMITATION OF ABSTRACT UL		

NSN 7540-01-280-5500

Standard Form 298 (Rev. 2-89)
Prescribed by ANSI Std. Z39-18

THIS PAGE INTENTIONALLY LEFT BLANK

Approved for public release; distribution is unlimited

**SIMULATION OF PERFORMANCE OF QUANTUM WELL INFRARED
PHOTODETECTORS**

Eftychios V. Psarakis
Lieutenant, Hellenic Navy
B.A., Hellenic Naval Academy, 1996

Submitted in partial fulfillment of the
requirements for the degree of

**MASTER OF SCIENCE IN APPLIED PHYSICS
MASTER OF SCIENCE IN ELECTRICAL ENGINEERING**

from the

**NAVAL POSTGRADUATE SCHOOL
June 2005**

Author: Eftychios Psarakis

Approved by: Gamani Karunasiri
Thesis Advisor

James Luscombe
Co-Advisor

Robert Hutchins
Co-Advisor

John Powers
Co-Advisor

James Luscombe
Chairman

John Powers
Chairman, Department of Electrical and Computer Engineering

THIS PAGE INTENTIONALLY LEFT BLANK

ABSTRACT

In this thesis the performance of a step quantum well infrared photodetector, designed by Kevin Lantz (June 2002) and experimentally studied by Michael Touse (September 2003) and Yeo Hwee Tiong (December 2004), was simulated in Matlab using the transfer matrix method. The results, obtained by the Matlab program, are compared with the experimental results, in an attempt to make inferences about the optimum way of designing QWIP detectors.

Simulation of the above implies numerical solution of the Schrödinger equation, using algorithms and methods, which give accurate results. In our approach, the transfer matrix method (TMM) was used with exponentials and Airy functions to represent the solutions to Schrödinger equation under zero and non-zero bias, respectively. The calculated results were compared with the experimental data and found to provide a good agreement which validated the accuracy of the model employed.

In the final section of the thesis we examine and simulate in Matlab the application of the extended Kalman filtering (EKF) to an infrared photodetector as a target tracking mechanism to both maneuvering and non-maneuvering targets. When we used one sensor for tracking, the results were reliable provided that the target did not maneuver. In the case of a maneuvering target the results were significantly improved when we used both sensors for tracking.

THIS PAGE INTENTIONALLY LEFT BLANK

TABLE OF CONTENTS

I.	INTRODUCTION.....	1
	A. QUANTUM WELL INFRARED PHOTODETECTORS (QWIPS)-	
	BRIEF REVIEW.....	1
	B. PURPOSE OF THIS THESIS	3
	C. MILITARY RELEVANCE.....	4
	D. THESIS OUTLINE.....	4
II.	MATHEMATICAL AND PHYSICAL BACKGROUND	7
	A. INTRODUCTION.....	7
	B. SCHRODINGER EQUATION.....	7
	C. EFFECTIVE MASS MODEL	8
	D. TRANSFER MATRIX METHOD (TMM)	9
	1. General.....	9
	2. Quantum Well Structure without Applied Electric Field	9
	3. Quantum Well Structure under Applied Electric Field.....	11
	a. General	11
	b. <i>Solution of the Schrödinger Equation in a Linear Potential</i>	12
	c. <i>Square Quantum Well Under an Electric Field</i>	16
	E. SUMMARY	20
III.	IMULATION ANALYSIS AND DATA	21
	A. INTRODUCTION.....	21
	B. DESCRIPTION OF QWIP SAMPLE	21
	C. DESCRIPTION OF THE COMPUTER MODEL	22
	1. Simulation Parameters	23
	D. STEP QUANTUM WELL WITHOUT AN APPLIED ELECTRIC	
	FIELD	24
	1. Bound State Energies.....	24
	2. Continuum State Energies	25
	E. STEP QUANTUM WELL STRUCTURE UNDER AN APPLIED	
	ELECTRIC FIELD	28
	1. General.....	28
	2. Bound State Energies.....	28
	3. Continuum State Energies	32
	F. BOUND-TO-CONTINUUM TRANSITIONS IN A QUANTUM WELL	34
	1. Fermi's Golden Rule.....	34
	2. Oscillator Strength.....	35
	3. Absorption Coefficient.....	37
	G. COMPARISON WITH EXPERIMENT	39
	1. Responsivity	39
	2. Absorption	41
	3. Photocurrent.....	41
	H. SUMMARY	45

IV. PERFORMANCE OF QUANTUM WELL INFRARED PHOTODETECTORS IN TARGET TRACKING	47
A. INTRODUCTION.....	47
B. DESCRIPTION OF THE MODEL.....	47
C. INITIAL ESTIMATE OF THE TARGET POSITION	48
D. EXTENDED KALMAN FILTERING CONSIDERATIONS	52
1. General.....	52
2. Bearing Tracking Expansion of EKF.....	53
3. Maneuvering Target Considerations	55
4. Trajectory Error and Measurement-Angle Chi-square Formulation.....	55
E. PROBLEM FORMULATION AND RESULTS.....	56
1. Non-Maneuvering Target BOT using One or Two IR Sensors in Noise Presence.....	56
2. BOT of Low Maneuvering Target using IR Sensors in Noise Presence	58
3. BOT of High Maneuvering Target using IR Sensors in Noise Presence.	61
F. SUMMARY	65
V. CONCLUSIONS AND FUTURE WORK.....	67
A. CONCLUSIONS	67
B. FUTURE WORK	68
APPENDIX A: QWIP SIMULATION PROGRAMS.....	69
APPENDIX B: EKF INITIALIZATION AND TRACKING.....	97
APPENDIX C: ASYMPTOTIC EXPRESSIONS.....	105
A. AIRY FUNCTION ANALYSIS.....	105
1. General.....	105
2. Asymptotic Expressions of Airy Functions	106
APPENDIX D: BOT COMPLETE CASE SET	109
LIST OF REFERENCES	129
INITIAL DISTRIBUTION LIST	133

LIST OF FIGURES

Figure 1.1	(a) excitation of bound electrons due to incident photon energy $\hbar\omega$. (b) Quantum well formation by sandwiching the appropriate bandgap material (From Ref. [5].).....	1
Figure 1.2	Conduction band diagram of a QIWP in an external electric field. Excited electrons escape from the ground state creating a photocurrent (From Ref. [4].).....	2
Figure 1.3	Energy band diagram showing B-B, B-QB, B-C, and B-M QWIP structures (From Ref. [4].).....	3
Figure 2.1:	Effective mass as a function of x for $Al_xGa_{1-x}As$ and $In_xGa_{1-x}As$	8
Figure 2.2:	Multilayered quantum well structure with zero applied bias.....	9
Figure 2.3	Multilayered quantum well structure with forward applied bias (left), and reverse applied bias (right).....	12
Figure 2.4:	Linear potential.	12
Figure 2.5:	Airy functions of the first kind.....	14
Figure 2.6:	Airy functions of the second kind.....	14
Figure 2.7:	Classical turning point at $x = -E/a$ and $y = E$	15
Figure 2.8:	Single quantum well structure with forward applied bias.	16
Figure 2.9:	Single quantum well structure with large forward applied bias (2×10^7 V/m).....	19
Figure 2.10:	Zeros of the matrix element m_{22} determines the energy characteristic values..	20
Figure 3.1:	Diagram of the designed and simulated QWIP (From [26].).....	22
Figure 3.2:	Potential diagram of simulated $In_xGa_{1-x}As$ quantum well structure.....	22
Figure 3.3:	$In_xGa_{1-x}As$ step quantum well ground state energy without applied bias.....	25
Figure 3.4:	Coefficients of the continuous states vs. energy difference.....	27
Figure 3.5:	Continuum wavefunctions (blue) and ground state wavefunction (red).....	28
Figure 3.6:	Ground energy and wavefunction in the step quantum well under an electric field of 10^6 V/m	29
Figure 3.7:	Ground energy and wavefunction in a $In_xGa_{1-x}As$ quantum well under -10^6 V/m applied field.	30
Figure 3.8:	Ground energy and wavefunction in a quantum well under 7×10^4 V/m	31
Figure 3.9:	Ground energy and wavefunction in a quantum well under -7×10^4 V/m	31

Figure 3.10:	Absolute value of coefficients under 10^6 V/m forward bias	33
Figure 3.11:	Continuum wavefunctions (blue) and ground state wavefunction (red) for the step quantum well under 10^6 V/m forward bias.	34
Figure 3.12:	Oscillator strength versus energy for bound-to-continuum transitions in an unbiased $In_xGa_{1-x}As$ step quantum well.	35
Figure 3.13:	Oscillator strength under 10^6 V/m applied bias vs. energy.	36
Figure 3.14:	Oscillator strength under 7×10^4 V/m applied bias vs. energy.	37
Figure 3.15:	Oscillator strength and density of states vs. energy.....	38
Figure 3.16:	Absorption coefficient vs. photon energy under 10^6 V/m applied bias.....	39
Figure 3.17:	Experimental responsivity vs. wavelength at $T = 40$ K (From [27].).....	40
Figure 3.18:	Computer simulation of absorption vs. wavelength for the step quantum well structure.....	41
Figure 3.19:	Calculated photocurrent vs. wavelength.....	44
Figure 3.20:	Measured responsivity, simulation photocurrent density and absorption vs. photon wavelength for 0.81 V forward bias.	45
Figure 4.1:	Encounter geometry of the Sensors and the target.....	47
Figure 4.2:	Encounter geometry of the initialization problem.	48
Figure 4.3:	Encounter geometry for the determination of the diagonal lengths.....	50
Figure 4.4:	Matlab initialization using two sets of synchronous bearings.	51
Figure 4.5:	The position of the target is located inside the uncertainty bearing box.	52
Figure 4.6:	True position and track position of straight line moving target using two IR sensors in the presence of measurement noise.....	56
Figure 4.7:	Track position error and chi-squared values vs. sample number for non-maneuvering target - two IR sensors in the presence of measurement noise. .	57
Figure 4.8:	True position and track position of a low g turning target using one IR sensor in the presence of measurement noise.	58
Figure 4.9:	Track position error and chi-squared values vs. sample number for low g maneuvering target - single IR sensor in the presence of measurement noise.59	59
Figure 4.10:	True position and track position of a low g turning target using two IR sensors in the presence of measurement noise.	60
Figure 4.11:	Track position error and chi-squared values vs. sample number for low g maneuvering target – two IR sensors in the presence of measurement noise..61	61
Figure 4.12:	True position and track position of a high g turning target using one IR sensor in the presence of measurement noise.	62

Figure 4.15:	Track position error and chi-squared values vs. sample number for high g maneuvering target – single IR sensor in the presence of measurement noise.	64
Figure C.1:	Airy functions of the first kind, $Ai(-z)$ and $Ai(z)$	105
Figure C.2:	Airy functions of the second kind, $Bi(-z)$ and $Bi(z)$	106
Figure C.3:	Matlab Airy functions vs. asymptotic expressions of the first kind	107
Figure C.4:	Matlab Airy functions vs. asymptotic expressions of the second kind	108

THIS PAGE INTENTIONALLY LEFT BLANK

LIST OF TABLES

Table 1.	Specifications of the test QWIP (From [26].).....	21
----------	---	----

THIS PAGE INTENTIONALLY LEFT BLANK

LIST OF ACRONYMS AND/OR ABBREVIATIONS

QWIP	Quantum Well Infrared Photodetector
MBE	Molecular Beam Epitaxy
B-B	Bound to Bound
B-QB	Bound to Quasibound
B-C	Bound to Continuum
B-M	Bound to Miniband
WKB	Wentzel -Kramer- Brillouin
EKF	Extended Kalman Filter
BOT	Bearing Only Tracking
IR	Infra-Red
FLIR	Forward Looking Infra-Red
FEM	Finite Element Method
TMM	Transfer Matrix Method
InGaAs	Indium Gallium Arsenide
AlGaAs	Aluminum Gallium Arsenide
DFB	Distributed Feed Back

THIS PAGE INTENTIONALLY LEFT BLANK

LIST OF SYMBOLS

\hbar	Reduced Plank's constant
m_e	Electron mass
Ψ	Wavefunction
U	Potential energy
m^*	Effective electron mass
E	Energy
k	Wavevector
Ai	Airy functions of the first kind
Bi	Airy functions of the second kind
F	Electric field
$V(x, 0)$	Potential profile
ξ_j	Effective masses ratio
$\% x_j$	Mole fraction
E_g	Bandgap energy
L	Length
W	Transition probability
I	Initial state
Ψ_F	Final wavefunction
Ψ_I	Initial wavefunction
E_F	Final energy
E_I	Initial energy

V_p	Interaction potential
$\hbar\omega$	Interaction photon
I_p	Incident photon flux
ϵ_o	Electric permittivity
c	Speed of light
ω	Photon frequency
p_e	Electron momentum
$\vec{\varepsilon}$	Photon polarization vector
f_{osc}	Oscillator strength
z	Direction of growth
ΔE	Energy change
Δz	Path difference
a	Absorption coefficient
N_d	Doping density
R	Responsivity
η	Quantum efficiency
$h\nu$	Average photon energy
g	Photoconductive gain
I_{det}	Test detector photocurrent
P_{det}	Test detector incident optical power
R_{ref}	Reference detector responsivity
$d \cdot S_w$	Reference detector surface area
V_{ref}	Reference detector voltage
A_{det}	Own detector surface area
T_{ZnSe}	Zinc Selenide transmittance
T_{GaAs}	Gallium Arsenide transmittance

J	Current density
W	Wronskian
θ	Measured angle
(x_{true}, y_{true})	True Cartesian position
f, h	Nonlinear valued functions
g	Non-linear matrix valued function
v_k	Uncorrelated Gaussian process
ω_k	Uncorrelated Gaussian process
$\hat{x}_{k+1 k}$	State vector
$P_{k+1 k}$	Covariance prediction matrix
F_k	Gradient of f
F'_k	Transpose gradient of f
H_{k+1}	Gradient of $h(k+1, \hat{x}_{k+1 k})$
R_{k+1}	Measurement uncertainty
dt	Time between the measurements
ω	Turn rate
Δ	Sampling interval

THIS PAGE INTENTIONALLY LEFT BLANK

ACKNOWLEDGMENTS

Though it is not in my idiosyncrasy to thank the people that help me through hard paths using just words, I can not help doing this. So, primarily I must thank my spiritual inspirator and my true friend, my wife, Florentia Maretta. I am grateful not only because she stood by me supporting my decisions throughout our stay in a foreign country, but also because she gave me the most precious gift I have ever been given, our daughter, Eleni – Ioanna.

I must also thank my parents, Basileios and Ioanna, that taught me never stop believing that a “good” fight is what matters, and it is always better than a winning fight.

Last but not least, I am grateful and eulogize my four advisors, Dr. Gamani Karunasiri, Dr. James Luscombe, Dr. Robert Hutchins and Dr. John Powers, who stood by me as both friends and teachers, leading me in the correct way to achieve knowledge. Without their help this thesis would not have been possible.

“Τα πάντα ρει” Ηράκλείτος 575-435 π.Χ

THIS PAGE INTENTIONALLY LEFT BLANK

I. INTRODUCTION

A. QUANTUM WELL INFRARED PHOTODETECTORS (QWIPS)-BRIEF REVIEW

In the recent years there has been a considerable increase in research activities towards the development of quantum well based infrared sensors [1-4]. The use of quantum wells made of larger bandgap materials, can overcome the difficulties associated with smaller bandgap materials, typically used in conventional infrared detectors [1]. The smaller bandgap materials are relatively unstable, and difficult to process, resulting in non-uniformities when focal plane arrays are made [1]. The infrared detectors have many commercial and military applications.

The operation of quantum well infrared photodetectors (QWIPs) is based on the excitation of bound electrons in a quantum well by infrared, as illustrated in Figure 1.1a. The quantum wells are formed by sandwiching a small bandgap material between large bandgap materials, as shown in Figure 1.1b. It is possible to use the quantum well formed either in the conduction band or valence band to fabricate QWIPs. In the case of conventional infrared detectors, the electrons in the valence band are excited across the bandgap, while in QWIP detectors it is necessary to dope the quantum well to populate the ground state using either n-type (for the conduction band well), or p-type (for the valence band well).

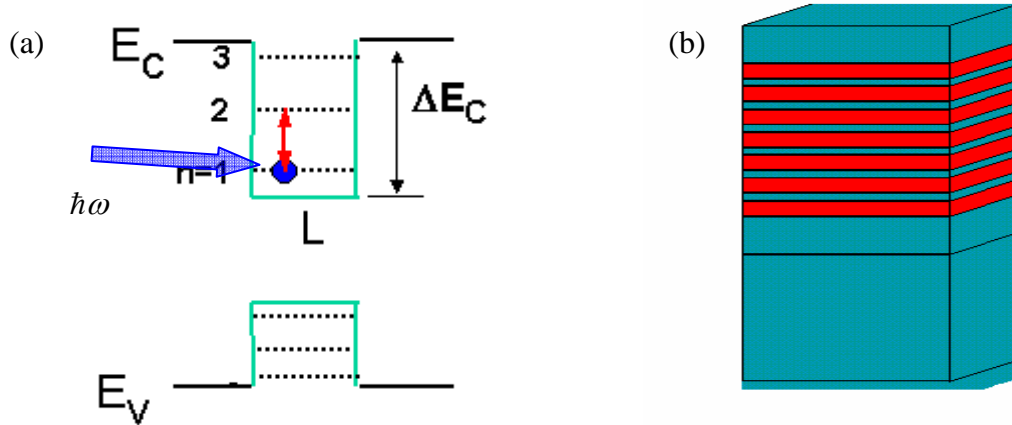


Figure 1.1 (a) excitation of bound electrons due to incident photon energy $\hbar\omega$. (b) Quantum well formation by sandwiching the appropriate bandgap material (From Ref. [5].)

In the design of quantum wells, the parameters, such as its dimension, and the composition of each structure material used, allow us to manipulate the behavior of the photoexcited carriers, so that they escape from the potential wells (quantum leak) and are collected as current by the application of an external bias, as shown in Figure 1.2.

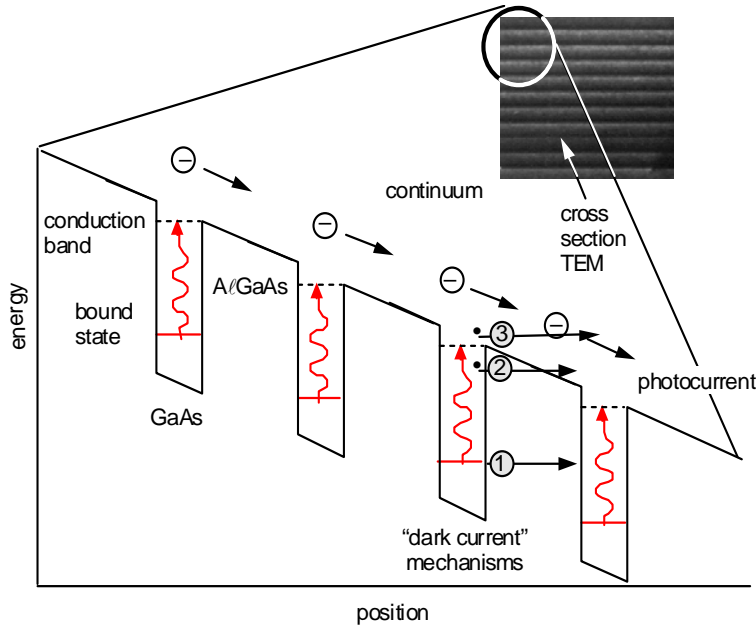


Figure 1.2 Conduction band diagram of a QIWP in an external electric field. Excited electrons escape from the ground state creating a photocurrent (From Ref. [4].)

The layers of QWIP detectors are primarily grown by molecular beam epitaxy (MBE), which gives thickness control in atomic scale [2, 4]. For achieving good material quality, the lattice constant of different materials used in QWIPs should be nearly the same. This avoids the dislocations generated by the lattice mismatch.

The usual wavelength coverage of QWIPs is between 3 and 20 microns [1, 8]. By controlling the barrier height and well width, it is possible to adjust the energy level separation and, hence, the wavelength dependence of the detector response. For example, the longer wavelength response can be achieved using shallow quantum wells.

QWIPs can be categorized according to the electron resulting state in four types: bound to bound (B-B), bound to quasibound (B-QB), bound to continuum (B-C), and bound to miniband (B-M), as schematically shown in Figure 1.3.

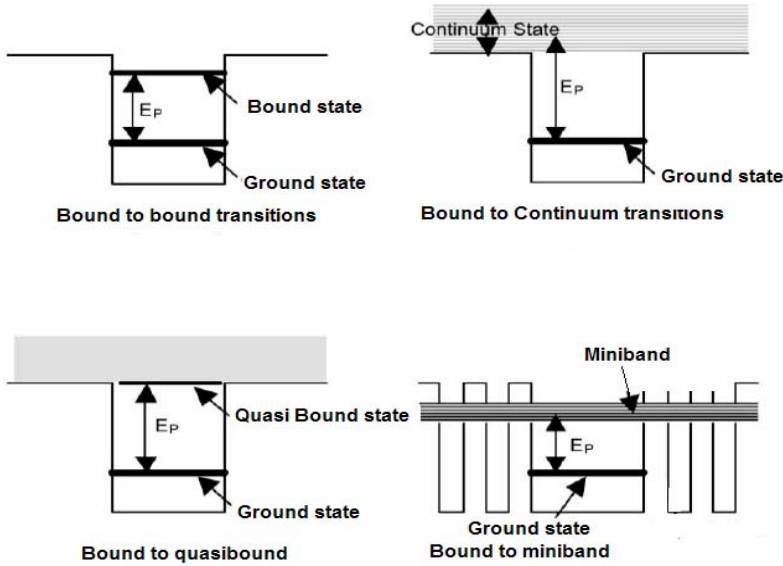


Figure 1.3 Energy band diagram showing B-B, B-QB, B-C, and B-M QWIP structures (From Ref. [4].)

The main factor which limits the QWIP performance is the dark current (the current that flows through a biased detector in the dark with no photons impinging on it), which plagues all infrared detectors. At temperatures above 45 K, the dark current of the QWIP is entirely dominated by classic thermionic emission of ground state electrons directly out of the well into the energy continuum. There are several theoretical techniques of minimizing it [3], most importantly the positioning of the first excited state to align with the barrier.

Recent studies indicate that multicolor operation of QWIPs is possible by simply stacking different types of quantum wells. A four-color QWIP was reported [5], based on stacked *InGaAs / AlGaAs* and *GaAs / AlGaAs* multi-quantum wells. In addition, a great deal of QWIP focal plane arrays have been analyzed and demonstrated by many groups [6-8], showing excellent performance in LWIR atmospheric window.

B. PURPOSE OF THIS THESIS

The purpose of this thesis was to simulate in Matlab the performance of symmetric and asymmetric quantum well structures under both zero bias and non-zero bias. It uses a design made in earlier thesis by Kevin R. Lantz [25] and experimental measurements made by Michael P. Touse [26] and Yeo Hwee Tiong [27]. The results obtained by

the MATLAB program are compared with the experimental results, in an attempt to make inferences about the optimum way of designing QWIP detectors. Simulation of the above implies numerical solution of the Schrödinger equation, using algorithms and methods which give accurate results. Various methods have been presented to solve the Schrödinger equation numerically including the WKB approximation, the Monte Carlo method and the finite element method, which all basically deal with solving second order differential equations. In our approach, the transfer matrix method will be used [12, 16] with exponential and Airy functions to represent the solutions to Schrödinger equation under zero and non-zero bias, respectively.

In the final section of the thesis, we will examine and simulate in Matlab the application of the extended Kalman filtering (EKF) to an infrared photodetector as a target tracking mechanism, to both maneuvering and non-maneuvering targets. Using a recursive type algorithm such as EKF, we will examine the bearing only tracking (BOT) problem classically. The main drawback of BOT is that the research is closed, meaning that the publication available is limited.

C. MILITARY RELEVANCE

QWIPs have a great deal of military and security applications. The most common are night vision, remote sensing and satellite IR imaging, FLIR, surveillance, targeting in a variety of terrains (air sea ground) and weapon delivery [4,7]. They are also widely used in search and rescue situations, mine detection, missile seeker formulation, smart munitions, weapon sights, preventive maintenance, non-destructive testing, medical imaging and surveillance [4]. Finally, the bearing-only-tracking application examined in the last chapter of the thesis, is considered a modern real-world problem featuring the advantage of passive target acquisition and surveillance. Since modern military needs are oriented in systems which can track targets without being noticed, the use of a modern QWIP sensor combined with a classic tracking algorithm, such as EKF, could result to a reliable surveillance system.

D. THESIS OUTLINE

The present thesis starts with a general discussion of the necessity of QWIPs, followed by a brief review of how these devices are formulated and where they find applications of military interest. Next, the reader is led, through the mathematical background, to

the simulation program, and the comparison to the laboratory case. Finally a “real world” application is investigated through BOT.

In particular, the outline of the present thesis is as follows:

Chapter II discusses the Schrödinger equation and the formulation of the transfer matrix method. The Schrödinger equation is applied in solving the unbiased and biased quantum well, and the transfer matrix method is applied in order to expand the solution in more than one region of the structure.

Chapter III provides information about the constructed Matlab code, and the laboratory semiconductor, while simulations are presented to show the QWIP behavior to several conditions of bias. Ideas such as probability current and bound-to-continuum transitions are presented, and finally the comparison to the laboratory case takes place.

Chapter IV is focused into the BOT problem. The used initialization of the state vector is presented, as long as the EKF algorithm, with emphasis into bearing tracking. Finally, we present and discuss several cases of sensor-target geometry.

Chapter V is a summary of the results, followed by suggestions for probable future research.

Appendix A includes the Matlab coding used to model the QWIP.

Appendix B includes the Matlab coding used to model the BOT problem.

Appendix C is an overview of Airy functions and their asymptotic expressions used to model the QWIP in the low bias cases.

Finally, Appendix D includes the complete set of resulting graphs of the BOT problem.

THIS PAGE INTENTIONALLY LEFT BLANK

II. MATHEMATICAL AND PHYSICAL BACKGROUND

A. INTRODUCTION

The infrared photodetectors examined in this thesis are quantum mechanical devices. Modeling this type of device requires solution of the key quantum mechanical equation, Schrödinger's equation. Given the potential and boundary conditions, we determine the shape and the temporal evolvement of the wave function by solving this second-order, partial differential equation. Due to the one dimensional nature of quantum well structures used in QWIPs, it is sufficient to solve the Schrödinger equation along the growth direction of the layers.

Over the years, various methods have been used for numerical solution of the Schrödinger equation, namely, the WKB approximation [9], the variational calculation method [10, 11], the Monte Carlo method [12], the finite element method (FEM) [13], and the transfer matrix method (TMM) [14]. In the present work, we employed the transfer matrix method (TMM) due to its flexibility in analyzing complex quantum well structures under external bias.

B. SCHRODINGER EQUATION

The one dimensional time-dependent Schrödinger equation for an electron can be written as:

$$-\frac{\hbar^2}{2m_e} \frac{\partial^2}{\partial x^2} \Psi(x, t) + U(x) \Psi(x, t) = i\hbar \frac{\partial}{\partial t} \Psi(x, t), \quad (2.1)$$

where \hbar is the reduced Plank's constant, m_e is the electron mass, x is the coordinate (usually taken along the direction of the growth), Ψ is the wavefunction and U is the potential energy.

Since the quantum well potential is independent of time, it is possible to separate the spatial and temporal dependencies with the spatial dependence satisfying the time-independent Schrödinger equation:

$$-\frac{\hbar^2}{2m} \frac{\partial^2}{\partial x^2} \Psi(x) + U(x) \Psi(x) = E \Psi(x). \quad (2.2)$$

C. EFFECTIVE MASS MODEL

The periodic potential of the atoms in semiconductor materials influences the propagation of an electron inside. In order to include the effect of the periodic potential, the electron mass m is usually replaced by an effective mass m^* , and treats the electron as a free particle [1]. The effective mass m^* is related to the band structure by:

$$m^* = \frac{\hbar^2}{d^2 E / dk^2}, \quad (2.3)$$

where \hbar is the Plank's constant, E is the conduction band energy and k the wavevector.

The QWIPs are usually made using potential wells in the conduction band well due to smaller effective mass which gives higher absorption [1]. For the materials used in this thesis ($InGaAs$, $AlGaAs$) the effective mass of electrons for various compositions is shown in Figure 2.1

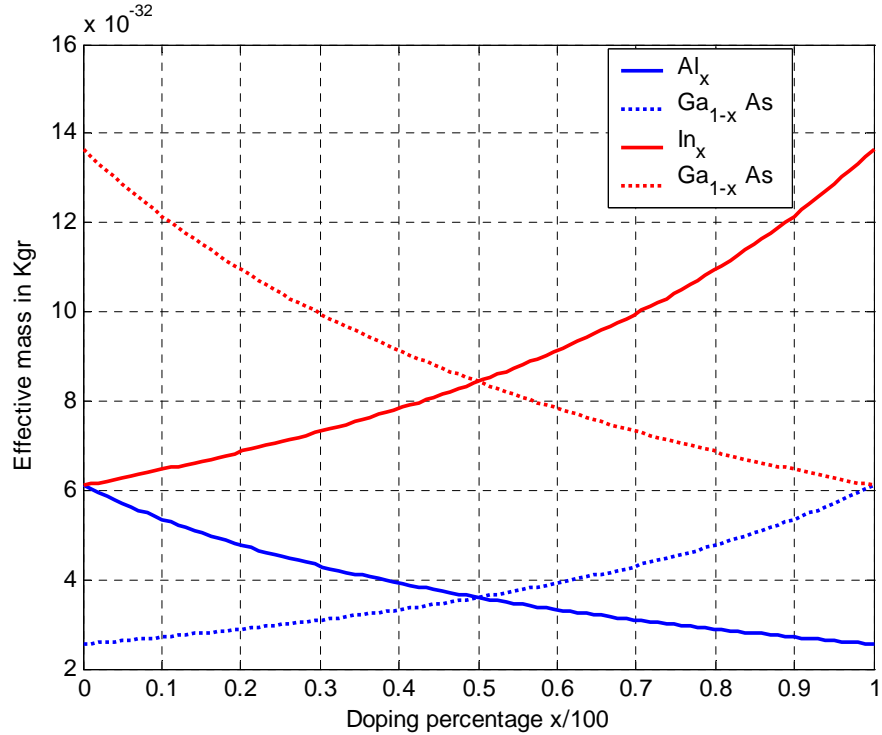


Figure 2.1: Effective mass as a function of x for $Al_xGa_{1-x}As$ and $In_xGa_{1-x}As$.

D. TRANSFER MATRIX METHOD (TMM)

1. General

The transfer matrix method is a relatively simple approach for solving Schrödinger equation for quantum well structures. It is generally used for a number of problems mostly involving second-order, partial differential equations (e.g., propagation characteristics in planar waveguides, spontaneous emission in DFB lasers) [12-14, 16].

Comparing this method with the other methods usually used for solving the same problems, TMM has the advantage both of simplicity and usage in low processing ability computers. Its simplicity mainly involves multiplication of 2×2 matrices which are straightforward to implement on a computer. We will examine two cases using the TMM, quantum well structures with and without the application of an external electric field.

2. Quantum Well Structure without Applied Electric Field

We assume an arbitrary multilayered quantum well structure as shown in Figure 2.2

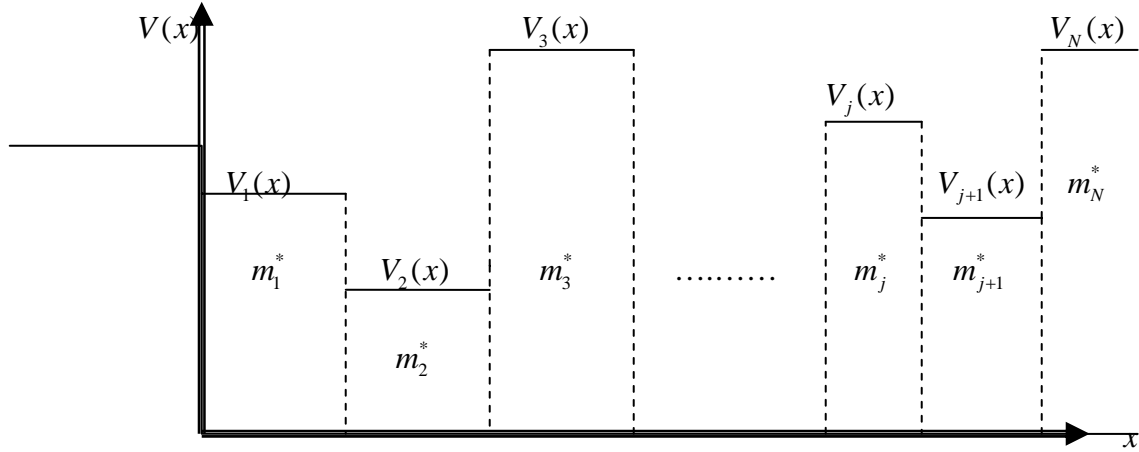


Figure 2.2: Multilayered quantum well structure with zero applied bias.

The time independent Schrödinger equation for each square quantum well region of the multilayered quantum well structure reads:

$$-\frac{\hbar^2}{2m_j^*} \frac{\partial^2 \Psi_j(x)}{\partial x_j^2} + V_j(x) \Psi_j(x) = E \Psi_j(x) . \quad (2.4)$$

where \hbar is the reduced Plank's constant, m_j^* is the electron effective mass in the region j , x is the coordinate (usually taken along the direction of the growth), Ψ is the wave- function, V_j is the potential energy in region j , and E stands for the associated electron energy. The general solution of Equation (2.17) in each region is a superposition of the left and the right traveling waves and is given by:

$$\Psi_j(x) = C_j e^{ik_j x} + D_j e^{-ik_j x}, \quad (2.5)$$

where k_j is implemented from the separation of variables and represents the wavenumber and C_j, D_j are arbitrary constants. The value of k_j depends on the region effective mass m_j^* and the potential height V_j in the region j as:

$$k_j = \frac{\sqrt{2m_j^*(E - V_j)}}{\hbar}. \quad (2.6)$$

At each boundary the probability current should be continuous which implies:

$$\Psi_j(x_j) = \Psi_{j+1}(x_j), \quad (2.7)$$

$$\frac{1}{m_j^*} \frac{d}{dx} [\Psi_j(x_j)] = \frac{1}{m_{j+1}^*} \frac{d}{dx} [\Psi_{j+1}(x_{j+1})], \quad (2.8)$$

where x_j is the coordinate at the boundary between j and $j+1$ layers.

Applying the solution of Equation (2.4), given by Equation (2.5), to Equations (2.7) and (2.8), we can find after some algebra:

$$C_{j+1} = \frac{k_{j+1}m_j^* + k_jm_{j+1}^*}{2k_{j+1}m_j^*} e^{ik_j x_j} e^{-ik_{j+1} x_j} C_j + \frac{k_{j+1}m_j^* - k_jm_{j+1}^*}{2k_{j+1}m_j^*} e^{-ik_j x_j} e^{-ik_{j+1} x_j} D_j, \quad (2.9)$$

$$D_{j+1} = \frac{k_{j+1}m_j^* - k_jm_{j+1}^*}{2k_{j+1}m_j^*} e^{ik_j x_j} e^{ik_{j+1} x_j} C_j + \frac{k_{j+1}m_j^* + k_jm_{j+1}^*}{2k_{j+1}m_j^*} e^{-ik_j x_j} e^{+ik_{j+1} x_j} D_j. \quad (2.10)$$

The results in Equations (2.9) and (2.10) can be expressed in a matrix form as

$$\begin{bmatrix} C_{j+1} \\ D_{j+1} \end{bmatrix} = M_j \begin{bmatrix} C_j \\ D_j \end{bmatrix}, \quad (2.11)$$

where M_j is given by as

$$M_j = \frac{1}{2} \begin{pmatrix} \left(1 + \frac{k_j m_{j+1}^*}{k_{j+1} m_j^*}\right) e^{i(k_j - k_{j+1})x_j} & \left(1 - \frac{k_j m_{j+1}^*}{k_{j+1} m_j^*}\right) e^{-i(k_j + k_{j+1})x_j} \\ \left(1 - \frac{k_j m_{j+1}^*}{k_{j+1} m_j^*}\right) e^{i(k_j + k_{j+1})x_j} & \left(1 + \frac{k_j m_{j+1}^*}{k_{j+1} m_j^*}\right) e^{-i(k_j - k_{j+1})x_j} \end{pmatrix}. \quad (2.12)$$

Repeatedly applying Equation (2.11), it is possible to relate the coefficients if the outermost layers as:

$$\begin{bmatrix} C_N \\ D_N \end{bmatrix} = M_j M_{j-1} \dots M_2 M_1 \begin{bmatrix} C_1 \\ D_1 \end{bmatrix} = \begin{pmatrix} m_{11} & m_{12} \\ m_{21} & m_{22} \end{pmatrix} \begin{bmatrix} C_1 \\ D_1 \end{bmatrix}. \quad (2.13)$$

In the case of bound states, the wavefunction must decrease exponentially to zero at the outermost boundaries. This implies that exponential growing coefficients in Equation (2.5), namely (D_N, C_1) , should equate to zero. Under this condition Equation (2.13) reduces to:

$$\begin{bmatrix} C_N \\ 0 \end{bmatrix} = \begin{pmatrix} m_{11} & m_{12} \\ m_{21} & m_{22} \end{pmatrix} \begin{bmatrix} 0 \\ D_1 \end{bmatrix}. \quad (2.14)$$

It can be easily seen from Equation (2.14) that, to satisfy the boundary conditions, we demand the matrix element $m_{22} = 0$. Since m_{22} depends only on energy E , the bound states can be found by plotting $m_{22}(E)$ and identifying the zero crossings.

3. Quantum Well Structure under Applied Electric Field

a. General

During the QWIP operation, it is necessary to apply external bias to extract photoexcited electrons. Under an external electric field, the quantum well potential tilts, as illustrated in Figure 2.3. The amount of the tilt depends on the strength and the direction of the applied field. The bias alters the energy levels in the quantum well structure, and hence, the photoresponse. In the section following, the effect of an external electric field on QWIP operation is analyzed by solving Schrödinger equation with a linear potential in addition to the quantum well potential.

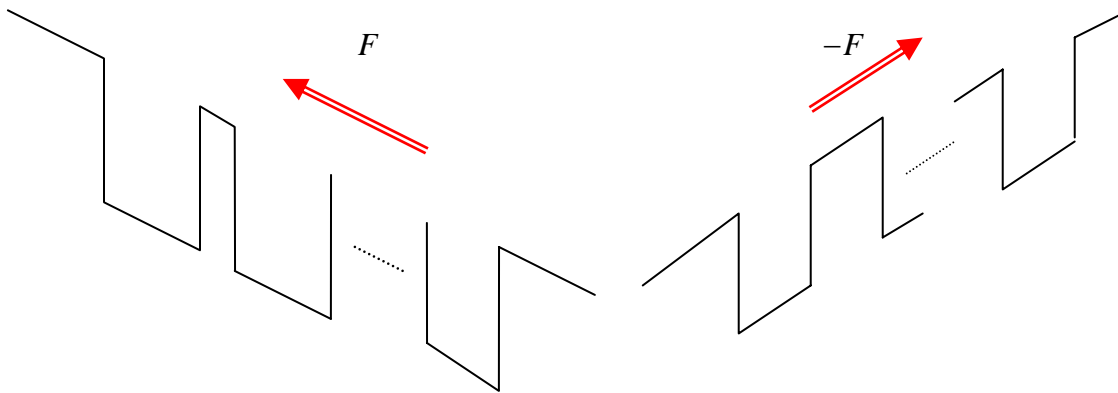


Figure 2.3 Multilayered quantum well structure with forward applied bias (left), and reverse applied bias (right).

b. *Solution of the Schrödinger Equation in a Linear Potential*

We first consider the solution of Schrödinger equation in a linear potential as shown in Figure 2.4.

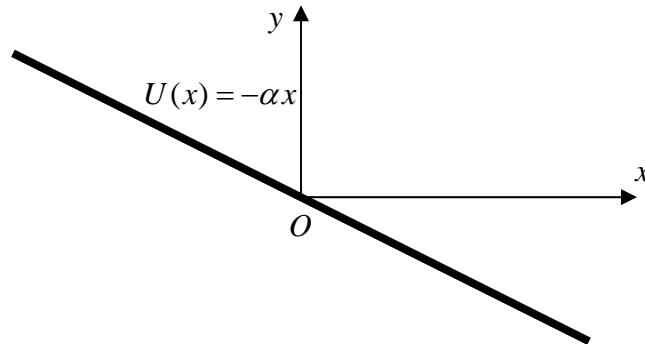


Figure 2.4: Linear potential.

Using Schrödinger's Equation (2.2) and substituting the value of $U(x) = -\alpha x$ we can get to the following form:

$$-\frac{\hbar^2}{2m} \frac{\partial^2}{\partial x^2} \Psi(x) - \alpha x \Psi(x) = E \Psi(x). \quad (2.15)$$

It is possible to convert Equation (2.15) to a standard differential equation by using the following change of variables.

$$x = \beta y + \gamma \Leftrightarrow y = \frac{x - \gamma}{\beta}, \quad (2.16)$$

where β and γ have units of length, while y is considered dimensionless.

Differentiating (2.16) with respect to x and substituting back into (2.15) yields:

$$\frac{d}{dx} \left(\frac{x-\gamma}{\beta} \right) = \frac{dy}{dx} \frac{d}{dy} \left(\frac{x-\gamma}{\beta} \right) = \frac{1}{\beta} \frac{d}{dy}, \quad (2.17)$$

$$\frac{1}{\beta^2} \frac{d^2}{dy^2} \Psi + \frac{2ma}{\hbar^2} (\beta y + \gamma) \Psi = -\frac{2m}{\hbar^2} E \Psi(x), \quad (2.18)$$

$$\frac{d^2}{dy^2} \Psi + \frac{2ma\beta^3}{\hbar^2} y \Psi + \frac{2m\beta^2}{\hbar^2} (a\gamma + E) \Psi = 0. \quad (2.19)$$

The variables β and γ can be chosen as given in Equation (2.16) to further simplify Equation (2.19), so:

$$\begin{aligned} a\gamma + E = 0 &\Rightarrow \gamma = -\frac{E}{a}, \\ \frac{2ma\beta^3}{\hbar^2} = -1 &\Rightarrow \beta = -\left(\frac{\hbar^2}{2ma} \right)^{1/3}. \end{aligned} \quad (2.20)$$

Using the parameters as defined in Equation (2.20), the Equation (2.19) can be transformed into the Airy's differential equation:

$$\frac{d^2}{dy^2} \Psi - y \Psi = 0, \quad (2.21)$$

which has two linearly independent solutions and are given in terms of Airy functions of the first and the second kind (Ai and Bi). The general solution can be written as a linear combination of the two Airy function multiplied by two arbitrary constants C and D [16]:

$$\Psi(y) = CAi(y) + DBi(y). \quad (2.22)$$

Figures (2.5) and (2.6) show the Airy functions of the first kind, Ai , and the second kind, Bi , as a function of y for both positive and negative directions.

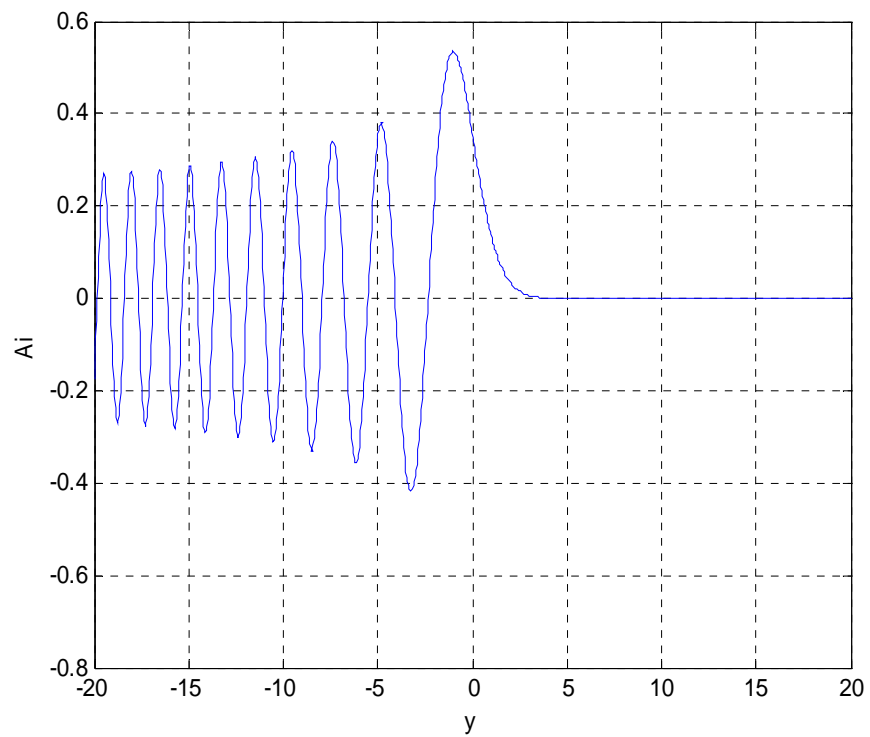


Figure 2.5: Airy functions of the first kind.

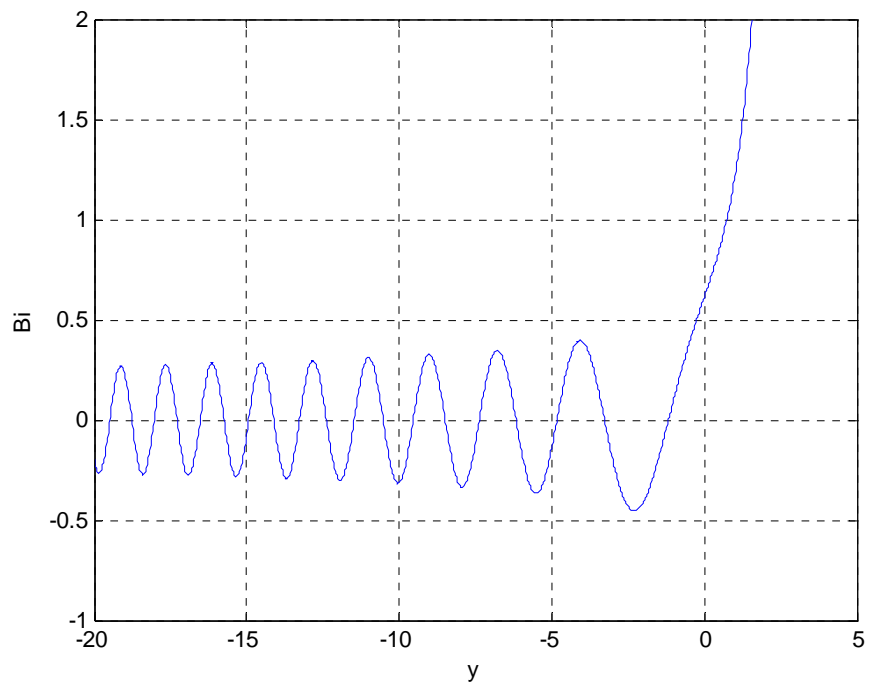


Figure 2.6: Airy functions of the second kind.

In Equation (2.16) by replacing the values of γ and β we get:

$$y = -\frac{x + \frac{E}{\alpha}}{\left| \left(\frac{\hbar^2}{2ma} \right)^{1/3} \right|}, \quad (2.38)$$

where $y = 0$ or $x = -E/\alpha$ corresponding to the classical turning point as shown in Figure 2.7.

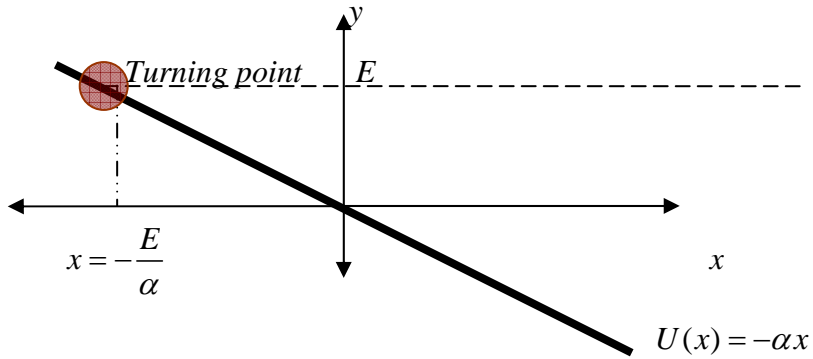


Figure 2.7: Classical turning point at $x = -E/\alpha$ and $y = E$.

Using the solutions of the Airy equation given by (2.22) and replacing the variable y , the solution in terms of the original coordinate x , the energy E , the constants α and \hbar , the particle mass m and the constants C and D can be written as:

$$\Psi(x) = CAi \left(-\frac{x + \frac{E}{\alpha}}{\left| \left(\frac{\hbar^2}{2ma} \right)^{1/3} \right|} \right) + DBi \left(-\frac{x + \frac{E}{\alpha}}{\left| \left(\frac{\hbar^2}{2ma} \right)^{1/3} \right|} \right). \quad (2.39)$$

The constants C and D are determined by the boundary conditions and for the above potential $D = 0$ since Bi is exponentially growing in the barrier region or negative x direction.

c. Square Quantum Well Under an Electric Field

Generally, when an electric field is applied to a quantum well structure as schematically illustrated in Figure 2.8, the profile of the potential will be changed [1, 12].

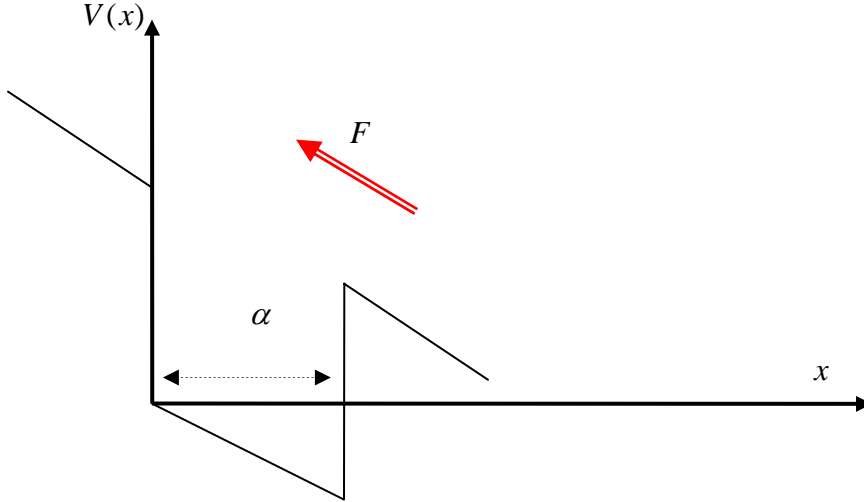


Figure 2.8: Single quantum well structure with forward applied bias.

This change is given by the equation:

$$V(x, F) = V(x, 0) - exF, \quad (2.40)$$

where $V(x, 0)$ is the potential profile of the quantum well, F is the applied electric field in V/m , e is the electron charge and x is the associated spatial coordinate.

By substitution of Equation (2.40) into the Schrödinger equation we arrive at the following formula:

$$-\frac{\hbar^2}{2m_j^*(x)} \frac{\partial^2 \Psi_j(x)}{\partial x^2} + (V_j - exF)(x) \Psi_j(x) = E \Psi_j(x). \quad (2.41)$$

Since the potential energy V_j is a constant within the j^{th} layer of the quantum well, the solution to Equation (2.41) can be written as a linear combination of Airy functions [16] as:

$$\Psi(x) = C_j Ai(\rho_j(x)) + D_j Bi(\rho_j(x)), \quad (2.42)$$

and $\rho_j(x)$ is defined as

$$\rho_j(x) = \frac{-Fx - \eta_j}{\left(\frac{\hbar^2 F^2}{2m_j^* e}\right)^{1/3}}, \quad (2.43)$$

where m_j^* is the effective mass associated with the j^{th} layer and η_j is given by:

$$\eta_j = \left(\frac{E - V_j}{e} \right), \quad (2.44)$$

where E is the energy of the electron.

The boundary conditions given by Equations (2.7) and (2.8) are still applicable to the Airy functions solution, given by Equation (2.42). An arbitrary coordinate system was chosen to be at the upper left end of the potential well, for simplicity purposes, as we illustrated in Figure 2.8.

The boundary conditions between two neighbor layers j and $j+1$ of the quantum well, give the following relations between the coefficients:

$$\frac{C_j}{\pi} = C_{j+1} \left\{ Ai(\beta_{j+1}) Bi'(\beta_j) - \xi_j Ai'(\beta_{j+1}) Bi(\beta_j) \right\} + D_{j+1} \left\{ Bi(\beta_{j+1}) Bi'(\beta_j) - \xi_j Bi(\beta_j) Bi'(\beta_{j+1}) \right\} \quad (2.45)$$

$$\frac{D_j}{\pi} = C_{j+1} \left\{ \xi_j Ai(\beta_j) Ai'(\beta_{j+1}) - Ai'(\beta_j) Ai(\beta_{j+1}) \right\} + D_{j+1} \left\{ \xi_j Ai(\beta_j) Bi'(\beta_{j+1}) - Ai'(\beta_j) Bi(\beta_{j+1}) \right\} \quad (2.46)$$

where β_{j+1} and β_j are defined as:

$$\beta_{j+1} = (-x_j - \eta_{j+1}) \left\{ \frac{2m_{j+1}^* ef}{\hbar^2} \right\}^{1/3},$$

$$\beta_j = (-x_j - \eta_j) \left\{ \frac{2m_j^* ef}{\hbar^2} \right\}^{1/3}, \quad (2.47)$$

and ξ_j is the ratio between the effective masses of the two layers.

$$\xi_j = \left(\frac{m_j^*}{m_{j+1}^*} \right)^{2/3}. \quad (2.48)$$

Equations (2.45) and (2.46) can be written in matrix form as:

$$\begin{pmatrix} C_j \\ D_j \end{pmatrix} = \pi \begin{pmatrix} Ai(\beta_{j+1})Bi'(\beta_j) - \xi_j Ai'(\beta_{j+1})Bi(\beta_j) & Bi(\beta_{j+1})Bi'(\beta_j) - \xi_j Bi(\beta_j)Bi'(\beta_{j+1}) \\ \xi_j Ai(\beta_j)Ai'(\beta_{j+1}) - Ai'(\beta_j)Ai(\beta_{j+1}) & \xi_j Ai(\beta_j)Bi'(\beta_{j+1}) - Ai'(\beta_j)Bi(\beta_{j+1}) \end{pmatrix} \begin{pmatrix} C_{j+1} \\ D_{j+1} \end{pmatrix}. \quad (2.49)$$

A repeated application of boundary conditions, similar to that of the unbiased case, the coefficients of the outermost layers can be related as:

$$\begin{bmatrix} C_1 \\ D_1 \end{bmatrix} = M_1 M_2 \dots M_{j-1} M_j \begin{bmatrix} C_N \\ D_N \end{bmatrix} = \begin{pmatrix} m_{11} & m_{12} \\ m_{21} & m_{22} \end{pmatrix} \begin{bmatrix} C_N \\ D_N \end{bmatrix}. \quad (2.50)$$

In the case of bound states, the wavefunctions in the outermost layers should decay, which implies that the coefficients that make them grow (D_1 and C_N) should equate to zero. Thus, Equation (2.50) reduces to:

$$\begin{bmatrix} C_1 \\ 0 \end{bmatrix} = \begin{pmatrix} m_{11} & m_{12} \\ m_{21} & m_{22} \end{pmatrix} \begin{bmatrix} 0 \\ D_N \end{bmatrix}. \quad (2.51)$$

This implies that,

$$m_{22}(E) = 0, \quad (2.52)$$

which corresponds to quantized energy states E inside the well under the electric field.

Figure 2.9 represents a single $Al_{0.3}Ga_{0.7}As$ quantum well of 40 Angstroms width where the applied field is 2×10^7 V/m. We represent the potential of the well using a blue line, the wavefunction with the black line, and the energy level with the red line.

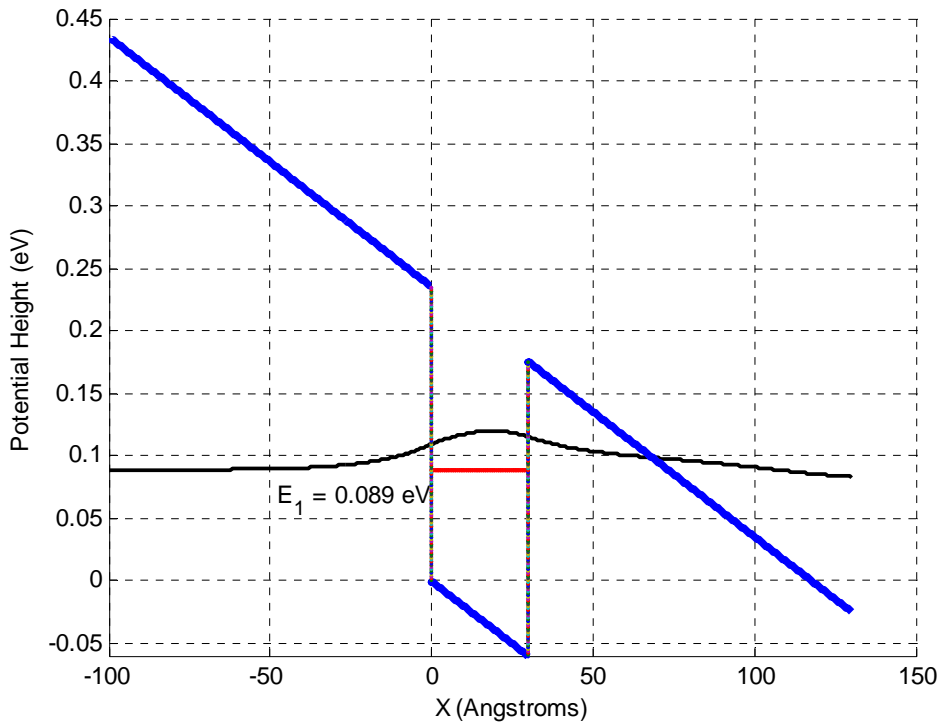


Figure 2.9: Single quantum well structure with large forward applied bias (2×10^7 V/m).

For example, the bound state energies in the quantum well were obtained by plotting $m_{22}(E)$ as a function of energy, as shown in Figure 2.10, and identifying the energies where $m_{22}(E) = 0$. For the parameters used, there was one bound state in the quantum well, at energy of about 0.089 eV. The extent of the wavefunction beyond the right side of the barrier indicates tunneling through the barrier due its finite width. This is responsible for leakage current in quantum well detectors at low temperatures.

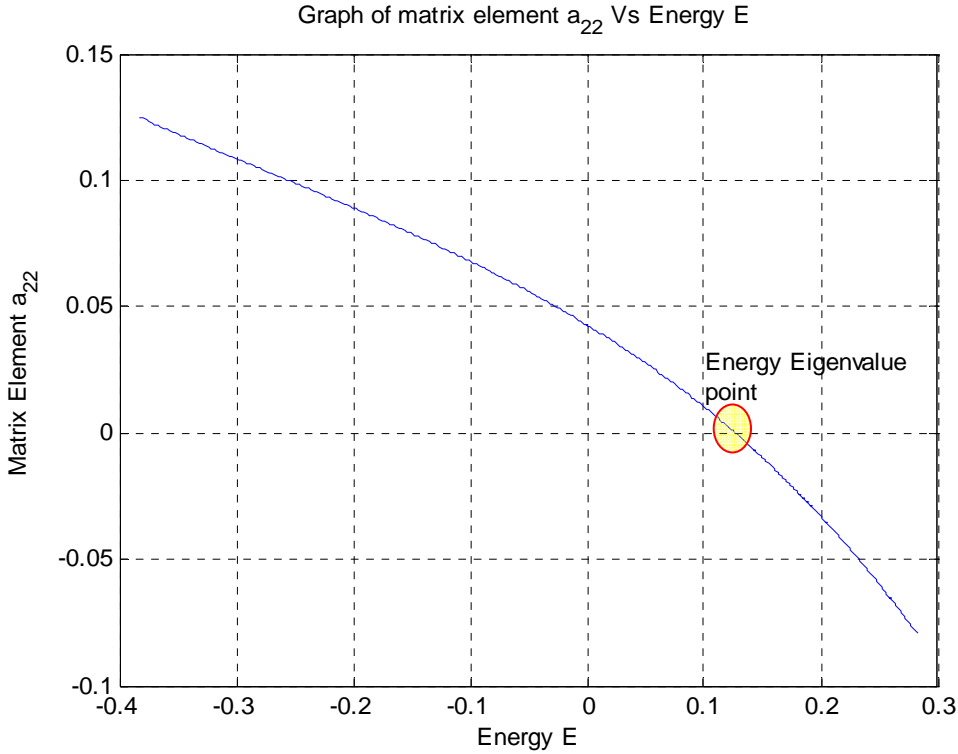


Figure 2.10: Zeros of the matrix element m_{22} determines the energy characteristic values.

E. SUMMARY

In this chapter, we developed the necessary tools to comprehend the solution of the Schrödinger equation in a quantum well structure, with and without the presence of electric field. The use of transfer matrix method with Airy functions enabled the analysis of quantum well structures under external bias. In the next chapter, response of a QWIP made from $In_x Ga_{1-x} As / GaAs$ step quantum well will be simulated and compared with available experimental data. Ideas such as continuous states and “normalization” of them, Fermi’s golden rule for optical transitions and probability current will be developed.

III. IMULATION ANALYSIS AND DATA

A. INTRODUCTION

The simulation program developed in Chapter II was employed to analyze a QWIP detector designed by Kevin Lantz [25] and experimentally studied by Michael Touse [26], and Yeo Hwee Tiong [27]. The comparison between the analysis and experimental results is focused on the infrared absorption and detector responsivity.

B. DESCRIPTION OF QWIP SAMPLE

The fabricated step QWIP consists of a multiple quantum well structure. The layer specification of the complete detector is presented in Table 1.

Substance	Mole %	Thickness (Å)	Si Doping Concentration (cm ⁻³)
GaAs	25x	5000	1E+18
GaAs		300	
InGaAs		40	
InGaAs		40	1E+18
GaAs		500	
GaAs		8000	1E+18
GaAs		6.35E+06	

Table 1. Specifications of the test QWIP (From [26].)

To increase the active layer thickness of the detector, 25 step $In_xGa_{1-x}As$ quantum wells were employed. A single period of the step quantum well is schematically shown in Figure 3.1. The width of the well, and the step, are 40 Angstroms each, while a 300-Angstrom barrier of $GaAs$ was placed between, in order to reduce the tunneling losses. The sample was grown by molecular beam epitaxy (MBE), which offers high accuracy for the design parameters, such as doping and layer thickness, since we have disposition of one or more pure materials onto the crystal wafer, one layer of atoms at the time, under ultra-high vacuum. The preliminary design of the QWIP predicted an IR absorption peak at 10.2 μm [26].

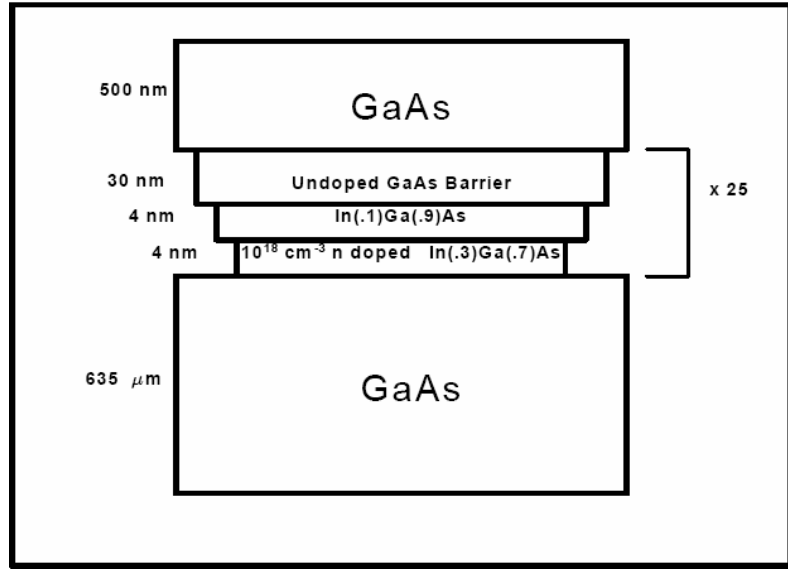


Figure 3.1: Diagram of the designed and simulated QWIP (From [26].)

C. DESCRIPTION OF THE COMPUTER MODEL

The structure used in simulation is a $In_x Ga_{1-x} As$ single step quantum well as shown in Figure 3.2.

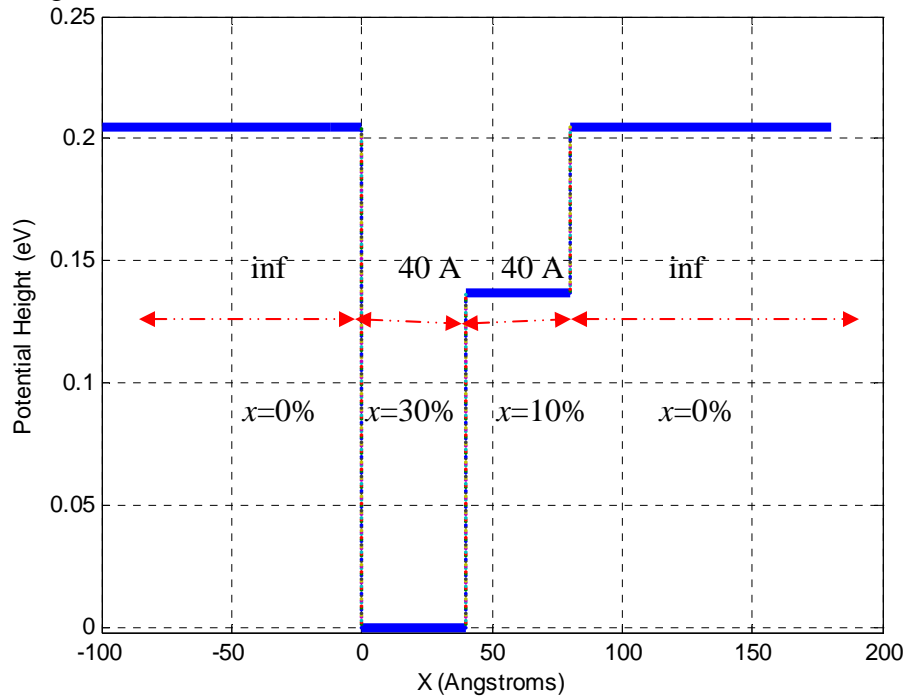


Figure 3.2: Potential diagram of simulated $In_x Ga_{1-x} As$ quantum well structure.

This quantum well is divided into four regions. The percentage of In_x in the first, and the fourth regions is zero, while for regions two and three is 30 and 10 percent, respectively. Similarly the width of the regions one and four is considered infinite, while regions two and three are 40 Angstroms wide each.

The behavior of a $In_xGa_{1-x}As$ single quantum well was investigated in the three main cases. In the first case we have studied the $In_xGa_{1-x}As$ quantum well without the application of an electric field, in the second case the electric field is present, and finally in the third case the electric field is present but its value is relatively small, which needed a special treatment. The main difference between these three cases, is that, in the first case, we have used the exponential solution of the Schrödinger equation, while in the case of large and small bias we took advantage of the Airy and asymptotic Airy solutions, respectively (Appendix C).

1. Simulation Parameters

For our numerical calculations, the values of the effective mass m_j^* , potential height V , and energy gap E_g for the $In_xGa_{1-x}As$ quantum well, were employed as:

$$m_j^* = \frac{1}{\left(\frac{\% x_j}{0.028m_0} \right)} + \frac{1 - \% x_j}{(0.067m_0)}, \quad (3.1)$$

where m_0 is the rest mass of the electron and $\% x_j$ is the mole fraction of In in the region j . The bandgap energy E_g (in eV) of the four layers and the corresponding barrier heights V_j can be obtained by the following formulas according to [1]:

$$E_g^1 = E_g^4 = 1.519 + 1.247(\% x_j), \quad (3.2)$$

$$E_g^2 = E_g^3 = 1.519 - 1.102(\% x_j), \quad (3.3)$$

$$V_j = 0.62(E_g^j - E_g^2). \quad (3.4)$$

Equations (3.1) through (3.3) characterize the physical, structural and electronic properties of $In_xGa_{1-x}As$ under specific conditions.

D. STEP QUANTUM WELL WITHOUT AN APPLIED ELECTRIC FIELD

1. Bound State Energies

The bound state energies are calculated using the transfer matrix method (TMM), according to the derivation of Subsection E-2 of the Chapter II. The energy eigenvalues are derived by the condition $m_{22}(E) = 0$, given in Equation (2.14). In order to find the values of E that satisfy the above condition, $m_{22}(E)$ was evaluated for energies from the bottom of the quantum well ($E = 0$), to the top ($E = V_1 = V_4$), using small increments ΔE . In the numerical analysis, the $m_{22}(E)$ derived at each energy was multiplied by the corresponding value at the previous energy and, if the resulting quantity is negative, then $m_{22}(E)$ had crossed a zero. This procedure allowed us to determine the bound state energies in the quantum well.

In the case of the step quantum well, there are four layers, which require three matrices to relate the coefficients of the outermost layers as given in Equations (3.5) to (3.7):

$$\begin{pmatrix} C_2 \\ D_2 \end{pmatrix} = M_1 \begin{pmatrix} C_1 \\ D_1 \end{pmatrix} = M_1 \begin{pmatrix} 0 \\ D_1 \end{pmatrix} = \begin{pmatrix} m_{11}^1 & m_{12}^1 \\ m_{21}^1 & m_{22}^1 \end{pmatrix} \begin{pmatrix} 0 \\ D_1 \end{pmatrix} = \begin{pmatrix} m_{12}^1 D_1 \\ m_{22}^1 D_1 \end{pmatrix}, \quad (3.5)$$

$$\begin{pmatrix} C_3 \\ D_3 \end{pmatrix} = M_2 \begin{pmatrix} C_2 \\ D_2 \end{pmatrix} = M_2 M_1 \begin{pmatrix} C_1 \\ D_1 \end{pmatrix} = \begin{pmatrix} m_{11}^{21} & m_{12}^{21} \\ m_{21}^{21} & m_{22}^{21} \end{pmatrix} \begin{pmatrix} 0 \\ D_1 \end{pmatrix} = \begin{pmatrix} m_{12}^{21} D_1 \\ m_{22}^{21} D_1 \end{pmatrix}, \quad (3.6)$$

$$\begin{pmatrix} C_4 \\ D_4 \end{pmatrix} = M_3 \begin{pmatrix} C_3 \\ D_3 \end{pmatrix} = M_3 M_2 M_1 \begin{pmatrix} C_1 \\ D_1 \end{pmatrix} = \begin{pmatrix} m_{11}^{321} & m_{12}^{321} \\ m_{21}^{321} & m_{22}^{321} \end{pmatrix} \begin{pmatrix} 0 \\ D_1 \end{pmatrix} = \begin{pmatrix} m_{12}^{321} D_1 \\ m_{22}^{321} D_1 \end{pmatrix}, \quad (3.7)$$

where M_j , $j = 1, 2, 3$, is given by Equation (2.12) and $m_{\mu\nu}^1$, $m_{\mu\nu}^{21}$, $m_{\mu\nu}^{321}$, where $\mu, \nu = 1, 2$, are the matrix elements of M_1 , the resulting elements of the multiplication of $M_2 M_1$, and the resulting elements of the multiplication of $M_3 M_2 M_1$, respectively.

The next step involves normalization of the bound wavefunction, which allows the determination of D_1 . Normalization implies:

$$\int_{-\infty}^{+\infty} \Psi_j(x) \Psi_j^*(x) dx = 1, \quad (3.8)$$

where $\Psi(x)$ and $\Psi^*(x)$ are the wavefunction and its complex conjugate, respectively.

For the parameters used for the step quantum well, there was only one bound state in the well as shown in Figure 3.3, alone with the normalized wave function.

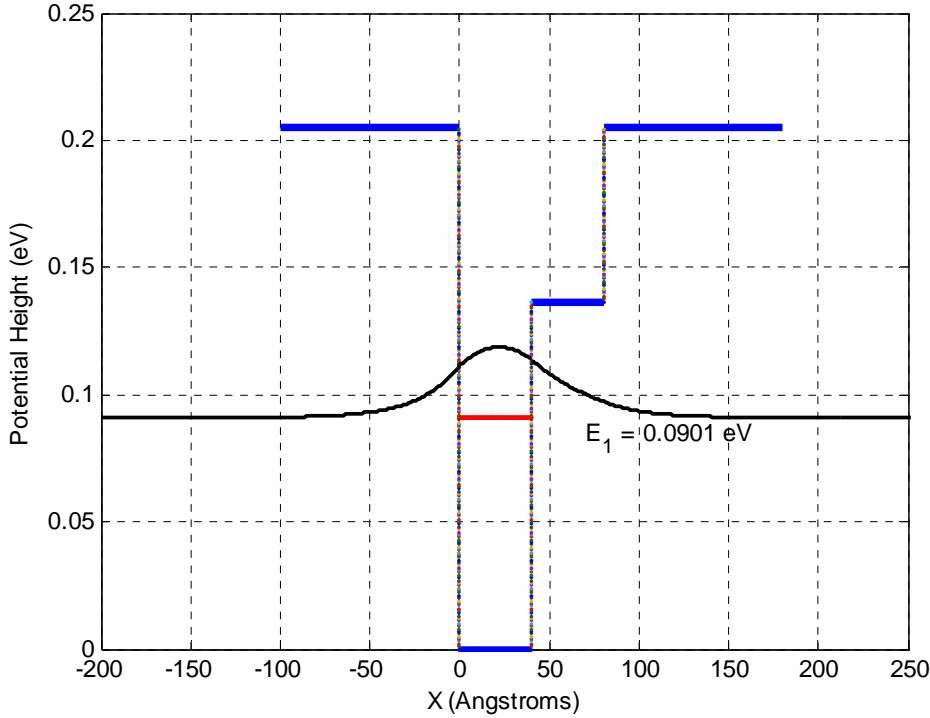


Figure 3.3: $In_xGa_{1-x}As$ step quantum well ground state energy without applied bias.

2. Continuum State Energies

The responsivity of QWIP detectors is strongly dependent on the location of the excited state [1, 17, 18]. To avoid the suppression of photocurrent due to tunneling, the excited state is usually aligned with the barrier which also minimizes the thermionic emission of ground state electrons [1]. It is possible to calculate the continuum state wavefunctions by using the transfer matrix method, with proper boundary conditions. If the electron is incident from the left side of the potential well, as shown in Figure 3.2, then the coefficient $D_4 = 0$, since it is not possible to have a left moving wave in the right side of the well.

Using the transfer matrix method, the coefficients of the fourth and the first regions can be related as:

$$\begin{pmatrix} C_4 \\ 0 \end{pmatrix} = M_3 M_2 M_1 \begin{pmatrix} C_1 \\ D_1 \end{pmatrix} = \begin{pmatrix} m_{11}^{321} & m_{12}^{321} \\ m_{21}^{321} & m_{22}^{321} \end{pmatrix} \begin{pmatrix} C_1 \\ D_1 \end{pmatrix}. \quad (3.9)$$

The coefficients D_1 and C_4 can be obtained in terms of the matrix elements defined earlier as:

$$D_1 = -\frac{m_{21}^{321}}{m_{22}^{321}} C_1, \quad (3.10)$$

$$C_4 = m_{11}^{321} C_1 + m_{12}^{321} D_1 = m_{11}^{321} C_1 - \frac{m_{12}^{321} m_{21}^{321}}{m_{22}^{321}} = \frac{m_{11}^{321} m_{22}^{321} C_1 - m_{12}^{321} m_{21}^{321}}{m_{22}^{321}}. \quad (3.11)$$

Similarly, the transfer matrix method gives the coefficients of the continuum wavefunctions for the second and third regions:

$$\begin{pmatrix} C_2 \\ D_2 \end{pmatrix} = M_1 \begin{pmatrix} C_1 \\ D_1 \end{pmatrix} = \begin{pmatrix} m_{11}^1 & m_{12}^1 \\ m_{21}^1 & m_{22}^1 \end{pmatrix} \begin{pmatrix} C_1 \\ -\frac{m_{21}^{321}}{m_{22}^{321}} \end{pmatrix} = \begin{pmatrix} m_{11}^1 C_1 - \frac{m_{12}^1 m_{21}^{321}}{m_{22}^{321}} \\ m_{21}^1 C_1 - \frac{m_{22}^1 m_{21}^{321}}{m_{22}^{321}} \end{pmatrix}, \quad (3.12)$$

$$\begin{pmatrix} C_3 \\ D_3 \end{pmatrix} = M_2 M_1 \begin{pmatrix} C_1 \\ D_1 \end{pmatrix} = \begin{pmatrix} m_{11}^{21} & m_{12}^{21} \\ m_{21}^{21} & m_{22}^{21} \end{pmatrix} \begin{pmatrix} C_1 \\ -\frac{m_{21}^{321}}{m_{22}^{321}} \end{pmatrix} = \begin{pmatrix} m_{11}^{21} C_1 - \frac{m_{12}^{21} m_{21}^{321}}{m_{22}^{321}} \\ m_{21}^{21} - \frac{m_{22}^{21} m_{21}^{321}}{m_{22}^{321}} \end{pmatrix}. \quad (3.13)$$

Figure 3.4 shows the dependence of coefficients in different layers as a function of energy, for the step quantum well structure.

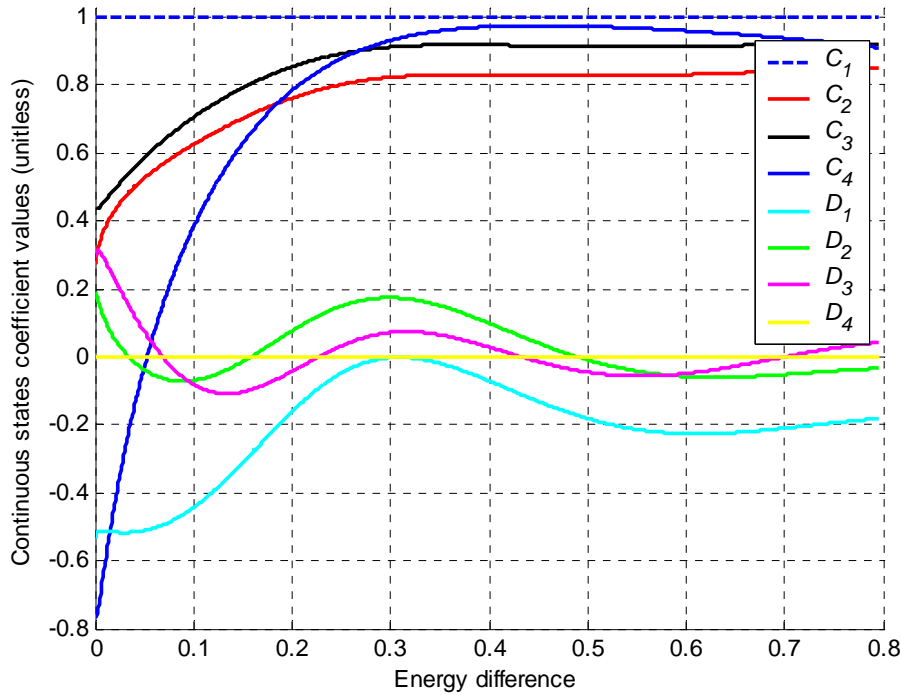


Figure 3.4: Coefficients of the continuous states vs. energy difference.

Normalization of the continuum wavefunctions cannot be executed using Equation (3.8), since these wavefunctions extend to infinity. The normalization of the continuum wavefunctions are usually done either using a hypothetical box around the quantum well [18], or using momentum space δ function normalization as described in [20]. Figure 3.5 illustrates 100 continuum wavefunctions up to 0.285 eV above the ground state using an arbitrary scale. The red curve in Figure 3.5, illustrates the ground state wavefunction. The oscillatory behavior of continuum wavefunctions represents the free motion of in the continuum.

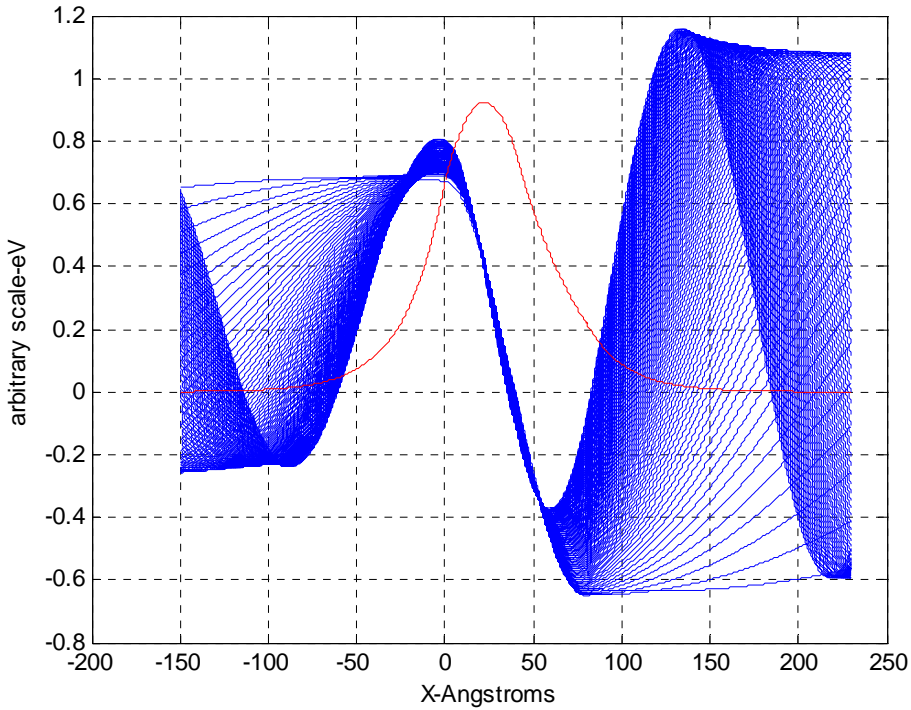


Figure 3.5: Continuum wavefunctions (blue) and ground state wavefunction (red).

E. STEP QUANTUM WELL STRUCTURE UNDER AN APPLIED ELECTRIC FIELD

1. General

As described in Chapter II, it is necessary to use Airy functions to represent wavefunctions when the quantum well is under bias. The implementation of Airy's function routines in a computer proved to be a relatively complicated task, especially when the electric field is small. Thus, a “weak field limit” was placed where the built-in Matlab Airy functions give numerical overflows, so lower biases than this threshold were treated using the asymptotic expressions of Airy functions. This limit was found to be about 10^5 V/m . The analytic coding used for this case, along with the previously examined cases is presented in the Appendix A.

2. Bound State Energies

The following shows the calculation of bound state energies in the step quantum well under a moderate electric field of 10^6 V/m . The energy eigenvalues can be found by

satisfying the condition (2.52), while the coefficients of Airy functions for different regions can be obtained as:

$$C_1 = m_{12}^{123}, C_2 = m_{12}^{23}, C_3 = m_{11}^3, C_4 = 0, \quad (3.14)$$

$$D_1 = 0, D_2 = m_{21}^{23}, D_3 = m_{21}^3, D_4 = 1, \quad (3.15)$$

where $m_{\mu\nu}^3, m_{\mu\nu}^{23}, m_{\mu\nu}^{123}$, $\mu, \nu = 1, 2$, are elements of $M_3, M_2 M_3, M_1 M_2 M_3$ matrices, respectively. There was only one bound state in the well as shown in Figure 3.6:

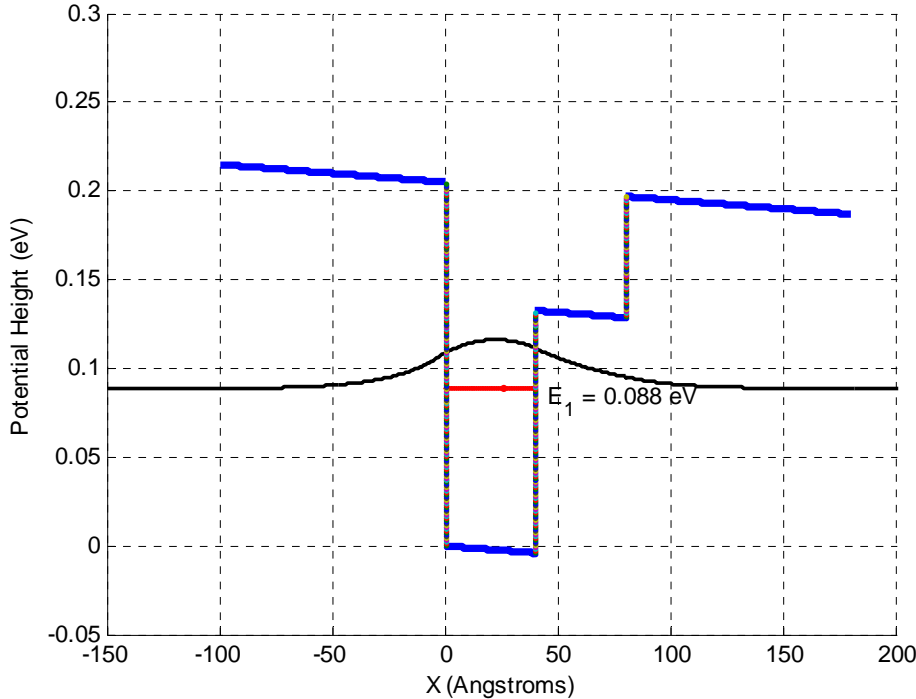


Figure 3.6: Ground energy and wavefunction in the step quantum well under an electric field of 10^6 V/m.

In the case of negative applied electric field of -10^6 V/m the ground state energy increases compared to the unbiased quantum well as shown in Figure 3.7.

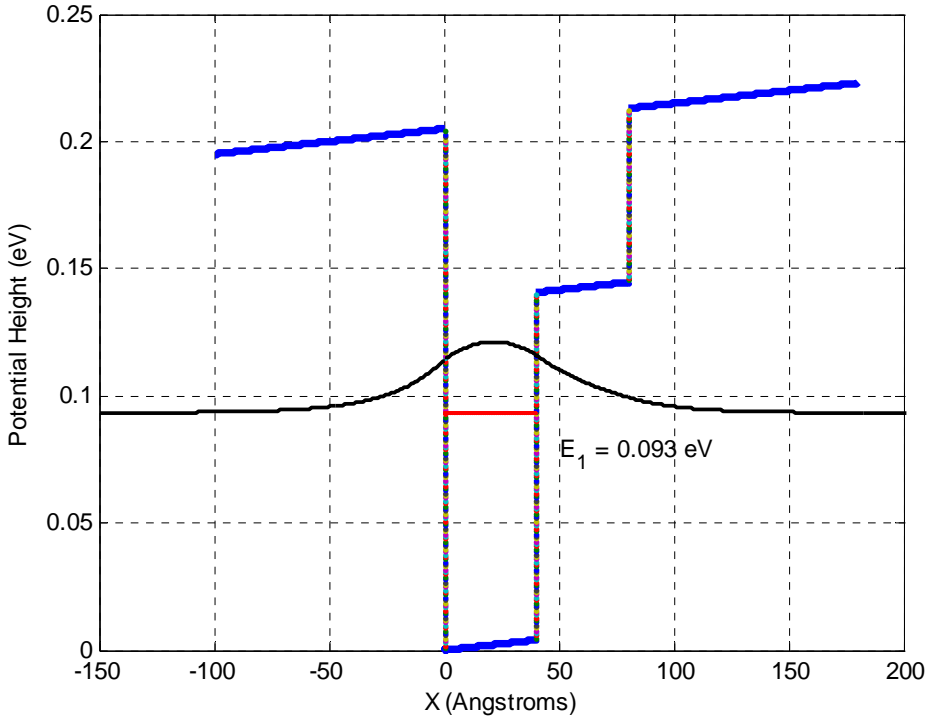


Figure 3.7: Ground energy and wavefunction in a $In_xGa_{1-x}As$ quantum well under -10^6 V/m applied field.

It is well known that the bound state energies in a quantum well do not shift when measured from the center of the well [1, 17]. Since our origin is at the edge of the well, the amount of the energy shift can be estimated using:

$$\text{shift} = -\frac{|e|FL}{2}, \quad (3.16)$$

where e is the electron charge, F is the applied bias, L is the length of the well which confines the energy state. This implies that for a 10^6 V/m applied field, the shift is about -0.002 eV from the unbiased position, and for -10^6 V/m the shift is about 0.002 eV .

This gives an energy separation of 0.004 eV for $\pm 10^6 \text{ V/m}$ field which is very close to the simulated value of 0.005 eV .

In the case of application of an electric field of $7 \times 10^4 \text{ V/m}$, the asymptotic expressions of Airy functions were needed to obtain the ground state energy and the associated wavefunction are illustrated in Figure 3.8.

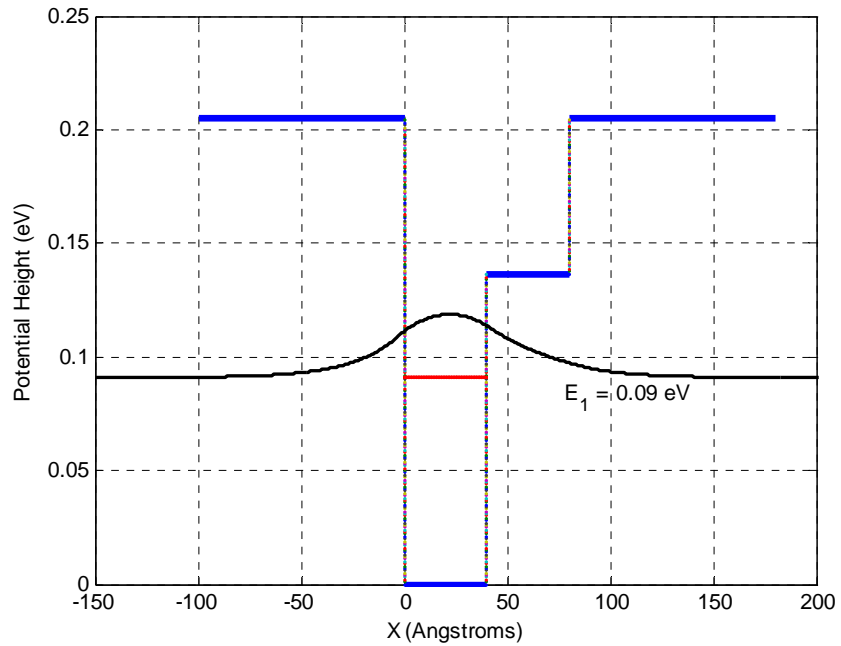


Figure 3.8: Ground energy and wavefunction in a quantum well under 7×10^4 V/m.

In the case of the same bias applied in the negative direction, the program gives that the ground energy E_1 lies at 0.091 eV, as shown in Figure 3.9.

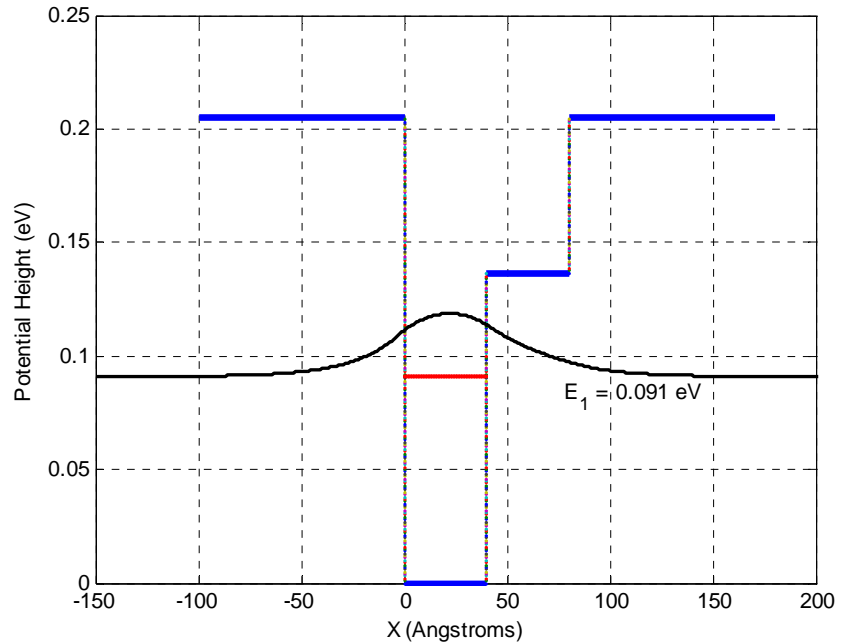


Figure 3.9: Ground energy and wavefunction in a quantum well under -7×10^4 V/m.

Again, the difference between the values of the ground energy level can be explained by Equation (3.18) since, for an 7×10^4 V/m applied field, the shift is about -7×10^{-4} eV from the unbiased position, and for -7×10^4 V/m is about 7×10^{-4} eV. This gives an energy separation of 0.00143 eV for $\pm 7 \times 10^4$ V/m field which is very close to the simulated value of 0.00137 eV. Finally the lowest bias that we have achieved in our simulation was $\pm 7 \times 10^4$ V/m or ± 0.7 kV/cm, which is much smaller than typically used in QWIP detector operation (10 kV/cm) [1, 16].

3. Continuum State Energies

The continuum state wavefunctions are obtained by assuming the electron is incident from the right side and setting the following boundary conditions for the coefficients of the outermost layers:

$$D_1 = 0. \quad (3.17)$$

Then applying the TMM, the coefficients in each layer can be obtained as:

$$D_4 = -\frac{m_{21}^{123}}{m_{22}^{123}} C_4, \quad (3.18)$$

$$C_3 = m_{11}^3 C_4 + m_{21}^3 D_4 = m_{11}^3 C_4 - m_{21}^3 \frac{m_{21}^{123}}{m_{22}^{123}} = \left(\frac{m_{11}^3 m_{22}^{123} C_4 - m_{21}^3 m_{21}^{123}}{m_{22}^{123}} \right), \quad (3.19)$$

$$D_3 = m_{21}^3 C_4 + m_{22}^3 D_4 = m_{21}^3 C_4 - m_{22}^3 \frac{m_{21}^{123}}{m_{22}^{123}} = \left(\frac{m_{21}^3 m_{22}^{123} C_4 - m_{22}^3 m_{21}^{123}}{m_{22}^{123}} \right), \quad (3.20)$$

$$C_2 = m_{11}^{23} C_4 + m_{12}^{23} D_4 = m_{11}^{23} C_4 + m_{12}^{23} \frac{m_{21}^{123}}{m_{22}^{123}} = \left(\frac{m_{11}^{23} m_{22}^{123} C_4 + m_{12}^{23} m_{21}^{123}}{m_{22}^{123}} \right), \quad (3.21)$$

$$C_1 = m_{11}^{123} C_4 + m_{12}^{123} D_4 = m_{11}^{123} C_4 - m_{12}^{123} \frac{m_{21}^{123}}{m_{22}^{123}} = \left(\frac{m_{11}^{123} m_{22}^{123} C_4 - m_{12}^{123} m_{21}^{123}}{m_{22}^{123}} \right). \quad (3.22)$$

For the normalization of the continuous wavefunctions, the technique described in the Appendix of Ref. [21] was used, since δ function normalization was not valid due to spatial dependence of the potential energy.

The absolute values of the coefficients as a function of continuum energy are illustrated in Figure 3.10. In the same figure, we observe the oscillatory behavior of the coefficients due to the resonances formed in the continuum region, due to constructive interference of incident and reflected waves.

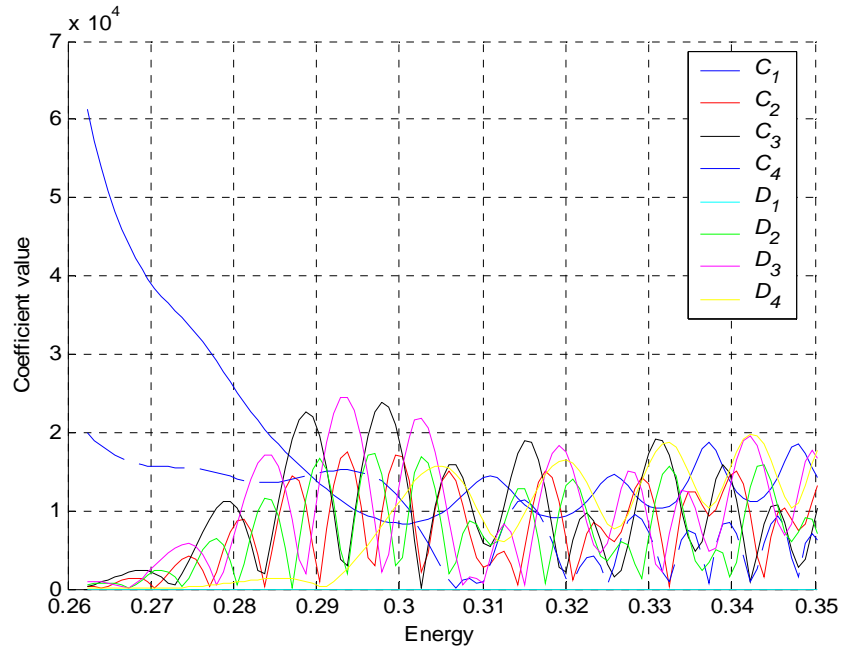


Figure 3.10: Absolute value of coefficients under 10^6 V/m forward bias.

The first 100 continuum wavefunctions of the tilted well are illustrated in Figure 3.11, along with the ground state wavefunction.

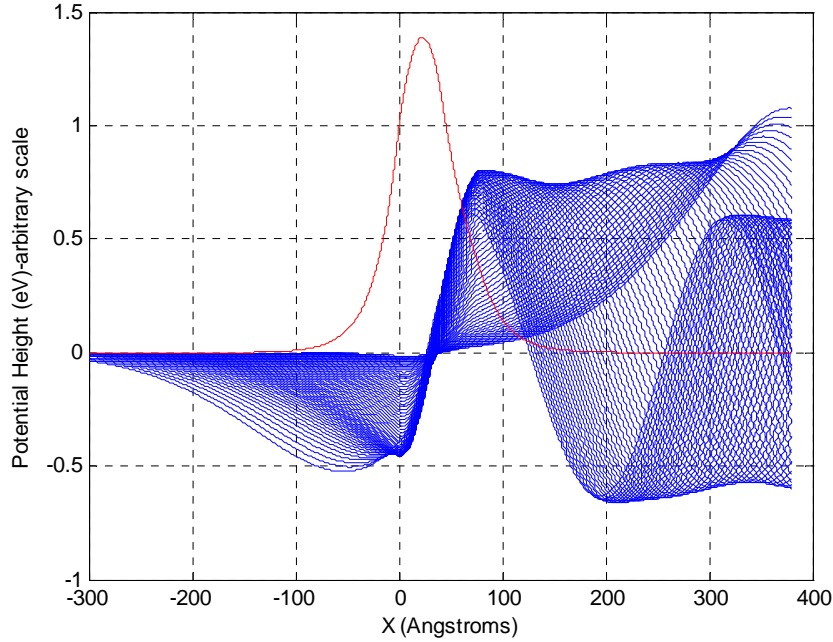


Figure 3.11: Continuum wavefunctions (blue) and ground state wavefunction (red) for the step quantum well under 10^6 V/m forward bias.

F. BOUND-TO-CONTINUUM TRANSITIONS IN A QUANTUM WELL

1. Fermi's Golden Rule

It was shown by Enrico Fermi [9], that the transition probability W of a quantum system from an initial state I to a final state F is given by:

$$W_{I \rightarrow F} = \frac{2\pi}{\hbar} \sum_F \left| \left\langle \Psi_F | V_p | \Psi_I \right\rangle \right|^2 \delta(E_F - E_I - \hbar\omega), \quad (3.23)$$

where Ψ_F and Ψ_I are the final and the initial wavefunctions, respectively, E_F and E_I the associated energies, V_p is the interaction potential and $\hbar\omega$ the interaction photon energy. The photon interaction potential in dipole approximation is given by [2]:

$$V_p = \frac{e}{m^*} \left(\frac{I_p \hbar}{2\epsilon_0 \epsilon \omega c} \right)^{1/2} \vec{\epsilon} \cdot \vec{p}_e, \quad (3.24)$$

where e is the electron charge, m^* the electron effective mass, I_p is the incident photon flux, ϵ_0 and ϵ characterize the electric permittivity, c is the speed of light, ω is the

frequency of the photon, p_e defines the momentum of the electron and $\vec{\epsilon}$ is the polarization vector of the photon.

2. Oscillator Strength

The oscillator strength f_{osc} for a transition from an initial state to a final state is defined as [1]:

$$f_{osc} = \frac{2m^*}{\hbar} (E_F - E_I) \langle z \rangle^2 = \frac{2m^*}{\hbar} (E_F - E_I) \int_{z_1}^{z_2} \Psi_I^*(z) z \Psi_F(z) dz, \quad (3.25)$$

where E_F and Ψ_F are the final energy and wavefunction, respectively, E_I and Ψ_I are the initial energy and wavefunction, m^* is the effective mass, \hbar is Plank's constant and z is the direction of growth.

Generally the oscillator strength is an indication of how strong the transition is, which directly translates to the performance of a QWIP detector.

Figure 3.12 shows the calculated oscillator strength for the step quantum well, under zero bias, using the wavefunctions derived in Subsection D-2. The energy was measured from the ground state.

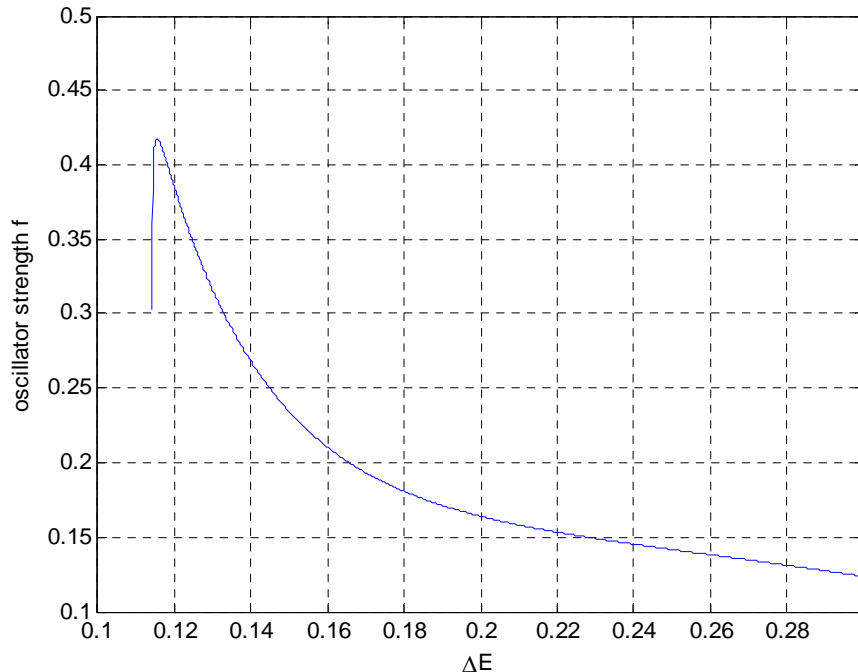


Figure 3.12: Oscillator strength versus energy for bound-to-continuum transitions in an unbiased $In_xGa_{1-x}As$ step quantum well.

Under an applied electric field the oscillator strength can be calculated using the wavefunctions derived in Subsection D-3. Figure 3.13 shows the oscillator strength for 10^6 V/m applied bias.

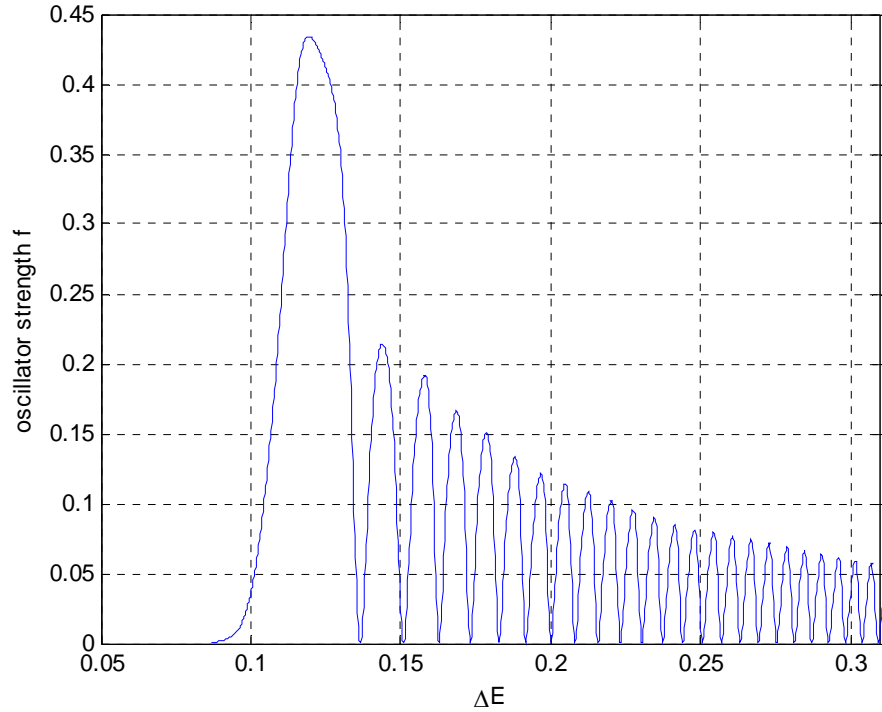


Figure 3.13: Oscillator strength under 10^6 V/m applied bias vs. energy.

The oscillatory behavior of the oscillator strength is due to the constructive interference of incident and reflected electron waves, from the tilted left quantum well barrier.

This oscillatory behavior becomes denser, as the strength of the electric field was reduced, as illustrated in Figure 3.14. As the bias approaches zero, the oscillations become closer and closer, to form a continuous curve as shown in Figure 3.12.

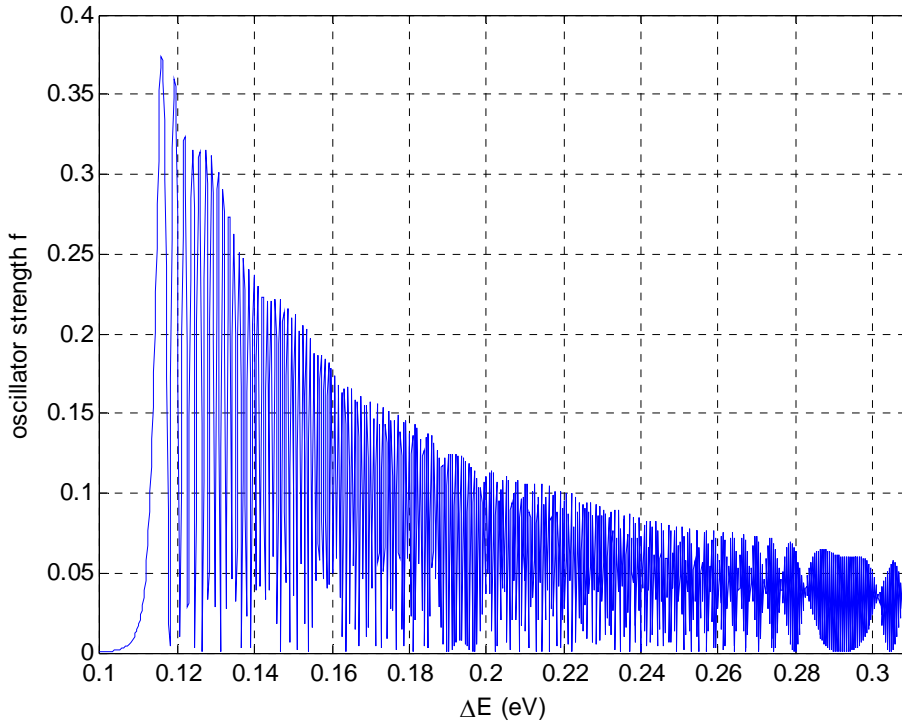


Figure 3.14: Oscillator strength under 7×10^4 V/m applied bias vs. energy.

The origin of oscillations as a function of electric field can be understood by estimating the amount of energy change (ΔE) required for obtaining path difference between incident and reflected electron waves (Δz) by one wavelength. This can be estimated by using the linear potential generated by the electric field as:

$$\Delta E = |e| F \Delta z. \quad (3.26)$$

It can be seen from Equation (3.26) that as the electric field becomes smaller, the amount of energy change needed to get one wavelength path difference reduces. This implies that the constructive interference occurs at a rapid rate, as the energy of the electron goes up, resulting a rapid oscillation of the oscillator strength.

3. Absorption Coefficient

The performance of photodetectors can be conveniently characterized using the absorption coefficient which is defined as:

$$a(h\omega) = \frac{h\omega \times (\text{number of transitions per unit volume and time})}{\text{incident energy flux}}. \quad (3.34)$$

For a QWIP detector the absorption coefficient can be expressed using the density of states and oscillator strength as [1, 2]:

$$a(h\omega) = \frac{N_d e^2 \hbar^2 L}{2(m^*)^2 \epsilon_0 n_r c} \sqrt{\frac{2m_b^*}{(\hbar\omega)^2 (E_F - V_b)}} \left| \left\langle \Psi_F \left| \frac{d}{dx} \right| \Psi_I \right\rangle \right|^2, \quad (3.35)$$

where N_d is the doping density in the well, L is the total length of the doped region, m_b^* and V_b are the barrier effective mass and potential height, respectively, and $\hbar\omega$ is the incident photon energy. Figure 3.15 shows the oscillator strength and the density of states for the step quantum well under a 10^6 V/m electric field.

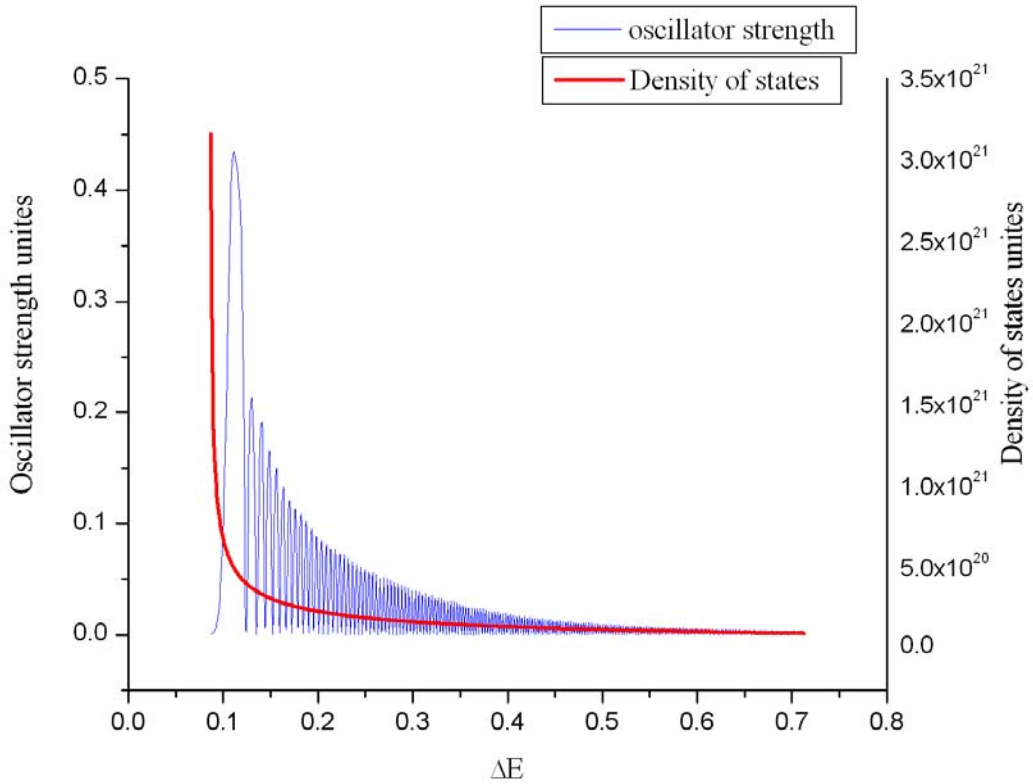


Figure 3.15: Oscillator strength and density of states vs. energy.

The absorption coefficient was calculated for the step quantum well assuming the doping density to be 10^{18} cm⁻³ and the result is shown in Figure 3.16. The calculated

absorption coefficient is in good agreement with that typically observed experimentally ($\square 800 \text{ cm}^{-1}$) [22].

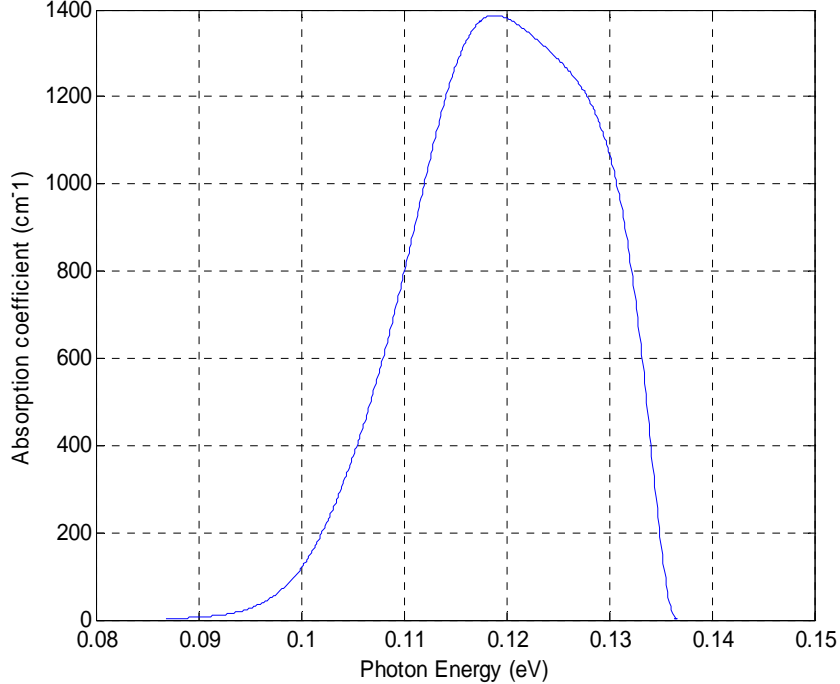


Figure 3.16: Absorption coefficient vs. photon energy under 10^6 V/m applied bias.

G. COMPARISON WITH EXPERIMENT

The step quantum well structure used for the simulation in the present Chapter was fabricated and characterized by Touse [26] and Yeo [27] using photocurrent spectroscopy. In this section, the measured responsivity of the detector is compared with the simulated responsivity using the absorption coefficient and outgoing probability current of the excited electron.

1. Responsivity

For a detector the normalized voltage or current signal per incident optical power is called responsivity [24]. We can express the responsivity R as:

$$R = \eta \frac{e}{h\nu} g, \quad (3.36)$$

where η is the quantum efficiency, e is the electron charge, $h\nu$ is the average photon energy and g is the photoconductive gain.

Taking into account all the geometrical and optical factors, the test detector responsivity can be estimated using [23]:

$$R = \frac{I_{\text{det}}}{P_{\text{det}}} = \frac{\sqrt{2} \cdot I_{\text{det}} \cdot R_{\text{ref}} \cdot d \cdot S_w}{V_{\text{ref}} \cdot A_{\text{det}} \cdot T_{\text{ZnSe}} \cdot T_{\text{GaAs}}}, \quad (3.37)$$

where I_{det} refers to the photocurrent, P_{det} is the optical power incident on the test detector power, R_{ref} is the responsivity of the reference detector, $d \cdot S_w$ refers to the reference detector surface area, V_{ref} is the generated by the reference detector voltage, A_{det} is our own detector surface area, T_{ZnSe} and T_{GaAs} are the transmittances of Zinc Selenide and Gallium Arsenide, respectively, of the cold head where the detector was situated.

During the experiment the temperature was kept fixed at 40K, so the photocurrents for the test detector under different applied electric fields were measured, and the responsivities calculated using Equation (3.37).

The experimental responsivity as a function of wavelength, for the step quantum well detector, for a set of biases is illustrated in Figure 3.17. The shifting of the peak position in Figure 3.17 is mainly due to the linear Stark effect in step quantum well as explained in Chapter II.

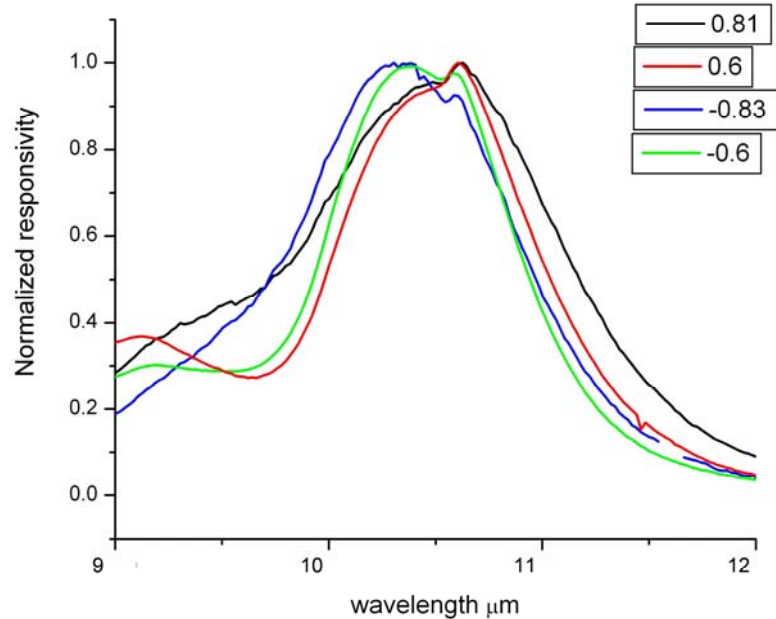


Figure 3.17: Experimental responsivity vs. wavelength at $T = 40$ K (From [27].)

2. Absorption

The normalized absorption coefficients calculated using the approach described in Subsection F-3 of the present Chapter, as a function of wavelength for the bias voltages used in the experiment are shown in Figure 3.18. The shifting of the peak position can be clearly seen from Figure 3.18.

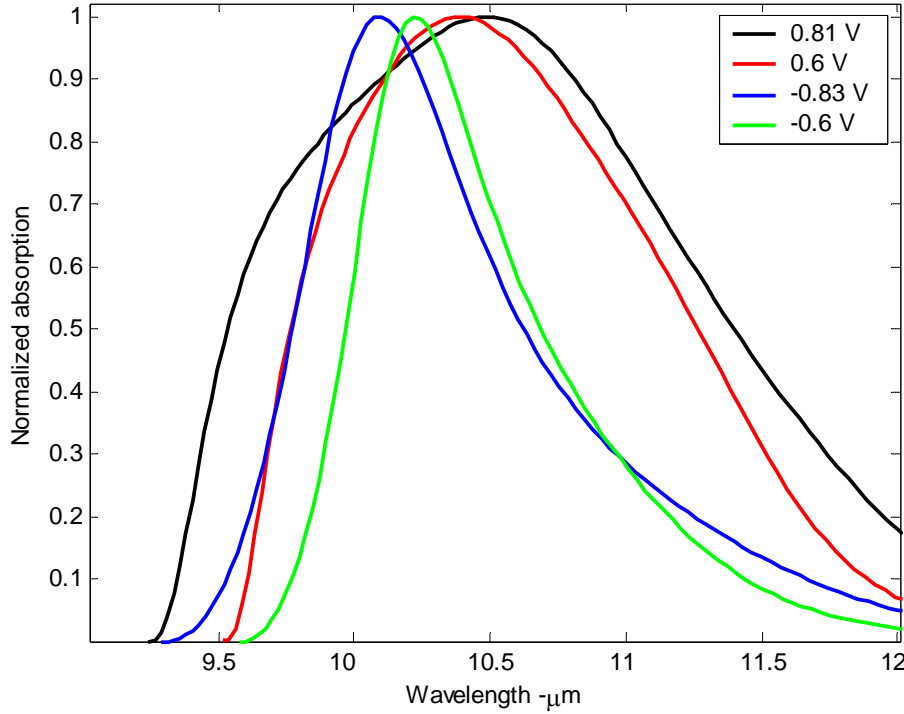


Figure 3.18: Computer simulation of absorption vs. wavelength for the step quantum well structure.

3. Photocurrent

The photocurrent density can be estimated by taking the product of quantum efficiency with the outgoing current density of the excited electron. The current density associated with a quantum state can be calculated using the wavefunction [24], as:

$$J = \frac{\hbar|e|}{2mi} \left(\Psi^* \frac{d\Psi}{dx} - \Psi \frac{d\Psi^*}{dx} \right), \quad (3.38)$$

where \hbar is the reduced Plank's constant, m is the electron mass, x is the direction where the current is evaluated and Ψ is the wavefunction.

Assuming the wavefunction has the following form:

$$CAi + DBi, \quad (3.39)$$

and after some algebraic effort, the quantity in the bracket of Equation (3.38) can be obtained as:

$$\Psi^* \frac{d\Psi}{dx} - \Psi \frac{d\Psi^*}{dx} = (C^* D - D^* C)(AiBi' - Ai'Bi), \quad (3.40)$$

Using the Wronskian (W) of the two Airy functions [40] the second bracket in Equation (3.40) can be further simplified as:

$$W = \begin{vmatrix} Ai & Bi \\ Ai' & Bi' \end{vmatrix} = AiBi' - Ai'Bi = \frac{1}{\pi}. \quad (3.41)$$

The current density given by Equation (3.38) can be expressed using the result in Equation (3.41) as:

$$J = \frac{\hbar|e|}{2\pi im|\beta|} (C^* D - D^* C), \quad (3.43)$$

where β is given by Equation (2.20), and appears in the denominator of Equation (3.43) due to the argument of the Airy functions of Equation (3.39), which according to Equation (2.39) is:

$$-\frac{\left(x + \frac{E}{\alpha}\right)}{|\beta|}. \quad (3.44)$$

Equation (3.43) represents the total current density which should be zero, since the probability density is time independent [20]. This requires that the coefficients C and D must be related as:

$$C^* \times D = D^* \times C. \quad (3.45)$$

In our simulations, it was found that this condition holds for all the regions of the quantum well structure. This indicates that the current density given in Equation (3.43) consists of two identical components, (a) outgoing current and (b) incoming current, which cancel to give zero net current.

In order to estimate the photocurrent after excitation of the electron from the ground state, it is necessary to extract the outgoing component from the current density that is given in Equation (3.43). The incoming and outgoing components of the current are not obvious in the case of the linear combinations of Airy functions, while they are usually obvious for exponential wavefunctions obtained for the zero bias case.

However, it can be shown that the linear combinations shown in Equations (3.46) and (3.47) produce pure outgoing and incoming currents by substituting in Equation (3.38):

$$\Psi_{out} = Ai - iBi, \quad (3.46)$$

$$\Psi_{in} = Ai + iBi. \quad (3.47)$$

The magnitudes of current density corresponding to the outgoing and incoming wavefunctions are given by:

$$J_{out} = \frac{\hbar}{2mi} \left(\Psi^* \frac{d\Psi}{dx} \right), \quad (3.48)$$

$$J_{in} = \frac{\hbar}{2mi} \left(-\Psi \frac{d\Psi^*}{dx} \right). \quad (3.49)$$

Under a positive bias, the photoexcited electrons moves to the right of the quantum well and the wavefunction in outermost right region, given in Equation (3.50) can be used to determine the outgoing current.

$$\Psi_4 = C_4 Ai + D_4 Bi, \quad (3.50)$$

where C_4 and D_4 are the coefficients defined in Subsection D-2 of Chapter II .

Equation (3.50) can be rewritten using the outgoing and incoming wavefunctions given in Equations (3.46) and (3.47) as:

$$\Psi_4 = C \Psi_{out} + D \Psi_{in}, \quad (3.51)$$

where the constants C and D are related to the coefficients C_4 and D_4 ,since:

$$C = \frac{C_4 - iD_4}{2}, \quad (3.52)$$

$$D = \frac{C_4 + iD_4}{2}. \quad (3.53)$$

The corresponding currents are given by:

$$J_{out} = \frac{\hbar}{\pi m |\beta|} \left| \frac{C_4 + i D_4}{2} \right|^2, \quad (3.54)$$

$$J_{in} = \frac{\hbar}{\pi m |\beta|} \left| \frac{C_4 - i D_4}{2} \right|^2. \quad (3.55)$$

The photocurrent density was calculated using the outgoing current given in Equation (3.54) and the quantum efficiency $\eta = \alpha L$ as:

$$J = \eta \frac{\hbar}{\pi m |\beta|} \left| \frac{C_4 - i D_4}{2} \right|^2, \quad (3.56)$$

where α is the absorption coefficient and L is the total length of the quantum well structure.

Figure 3.19 shows the calculated photocurrent for the biases used in the experimental measurement of the step quantum well detector.

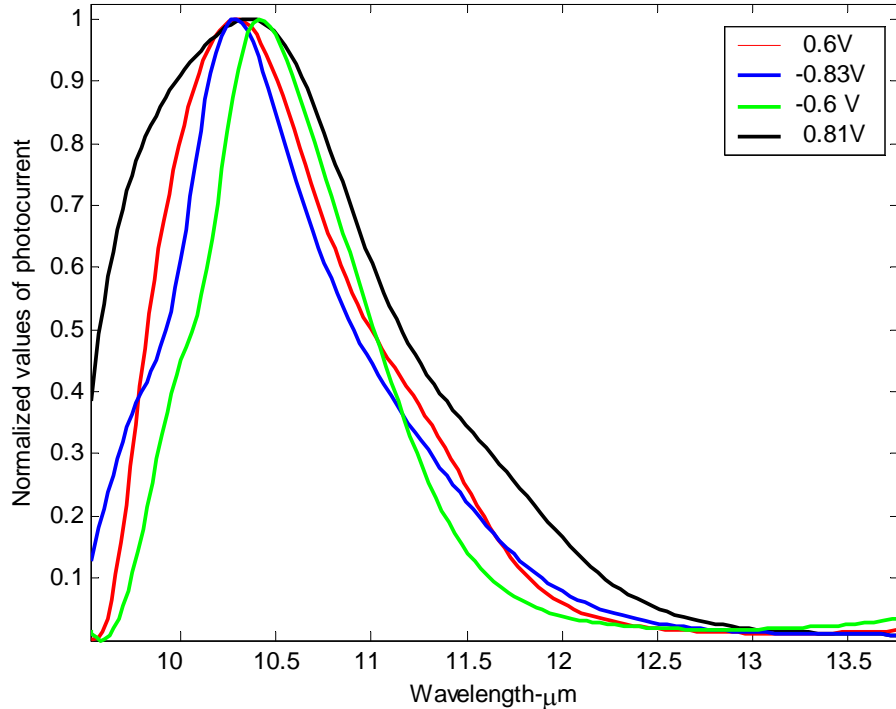


Figure 3.19: Calculated photocurrent vs. wavelength.

Figure 3.20 compares the absorption and normalized photocurrent density with the measured normalized responsivity at 0.81 V forward bias. It can be observed from this figure that the simulated photocurrent density provides a good description of the experimental observations. The absorption is found to be higher than the photocurrent density in the longer wavelength regime. This is mainly due to the difficulty of extraction of electrons after excitation due to the triangular barrier on the right side of the biased quantum well.

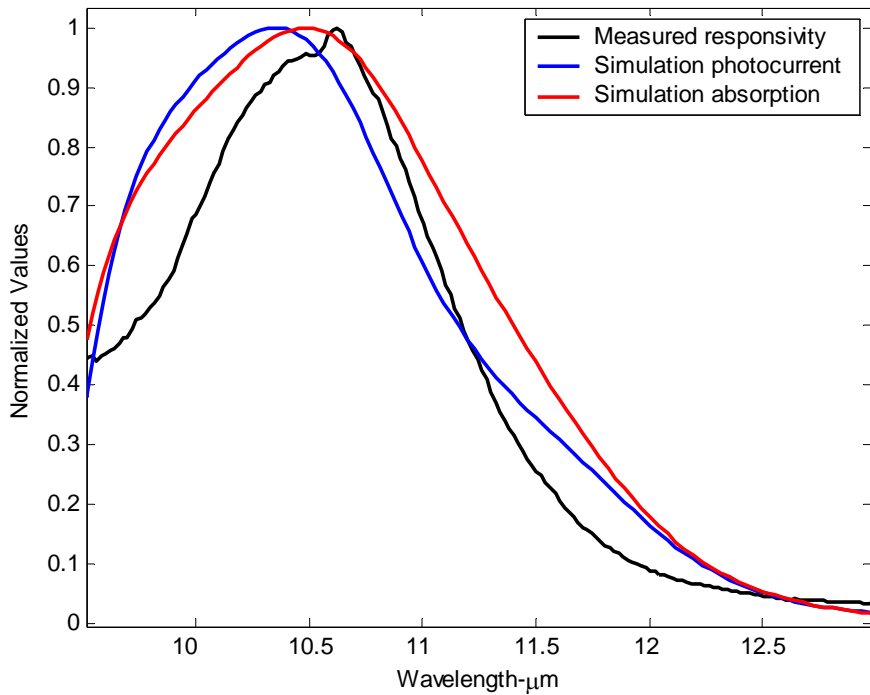


Figure 3.20: Measured responsivity, simulation photocurrent density and absorption vs. photon wavelength for 0.81 V forward bias.

H. SUMMARY

In this chapter, we presented the calculation of absorption and photocurrent density for the step quantum well detector under an external bias. The calculated results were compared with the experimental data and found to provide a good agreement which validated the accuracy of the model employed. In the following chapter, we will present a simulation code based in EKF for angle only tracking using an IR sensor. Ideas such as initialization using two synchronous bearing and EKF angle tracking will be developed and finally, selected results will be presented.

THIS PAGE INTENTIONALLY LEFT BLANK

IV. PERFORMANCE OF QUANTUM WELL INFRARED PHOTODETECTORS IN TARGET TRACKING

A. INTRODUCTION

Quantum well infrared photodetectors constitute a tool for target tracking since they offer the advantage of passivity. As we have discussed in the previous chapters, taking advantage of our ability to design multi-wavelength tunable infrared detectors, we can combine them with batch processing or recursive type algorithms in order to track targets passively.

In this chapter we simulate in Matlab the scenario of bearing-only tracking of a target using a recursive algorithm based on the Kalman filter. We investigate the bearing-only tracking problem in two main cases, namely tracking a non-maneuvering target and tracking a maneuvering target using either one or two sensors. Since we study only the tracking problem, we suppose that the detectors are tuned in such way that they provide the highest contrast and avoid the extensive clutter so they generate relatively reliable bearings. More analytic information about the coding used can be found in Appendix B. Finally the BOT problem is considered trivial since limited information is available

B. DESCRIPTION OF THE MODEL

The simulation model and the encounter geometry are illustrated in Figure 4.1.

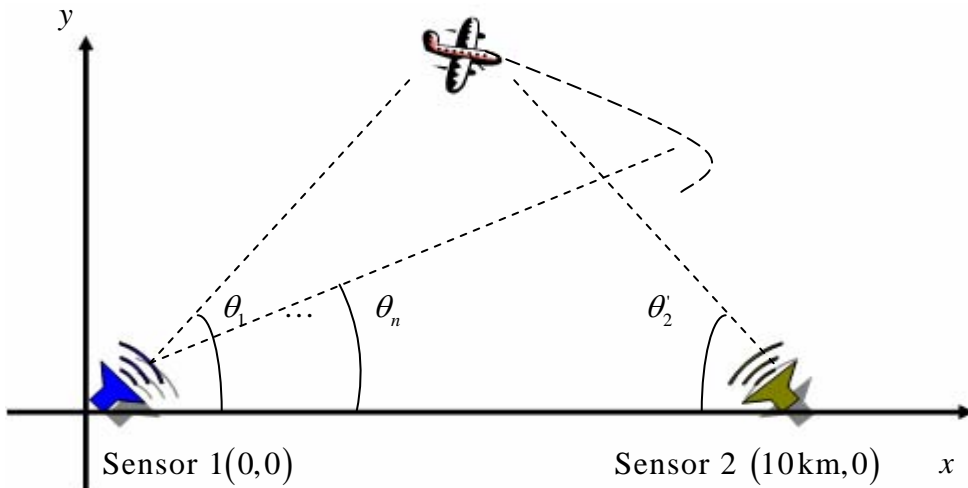


Figure 4.1: Encounter geometry of the Sensors and the target.

Sensor 1 is located at position $(0,0)$ of the local coordinate system, while sensor 2 was placed at $(10\text{ km}, 0)$. These sensors, since they are IR, can make measurements of the bearing of the target only. The first step of the bearing-only tracking using an extended Kalman filter is the initialization of the filter. Initialization in the case of EKF is sufficient if we estimate two positions of the target. This is possible either by taking advantage of the observer and target relative trajectory in the case that we use one sensor, or by assuming synchronous multiplatform bearings. BOT using asynchronous bearings will not be examined. So without the loss of generality in our case, we assume two stationary IR observers and synchronous initialization and tracking bearings.

C. INITIAL ESTIMATE OF THE TARGET POSITION

The initial estimate of the target position is determined using two sets of time synchronous bearings. We have used the fact that, in order to initialize our filter, we do not need to have the exact position of the target, only a reliable estimate of its position. The simplified geometrical problem is illustrated in Figure 4.2.

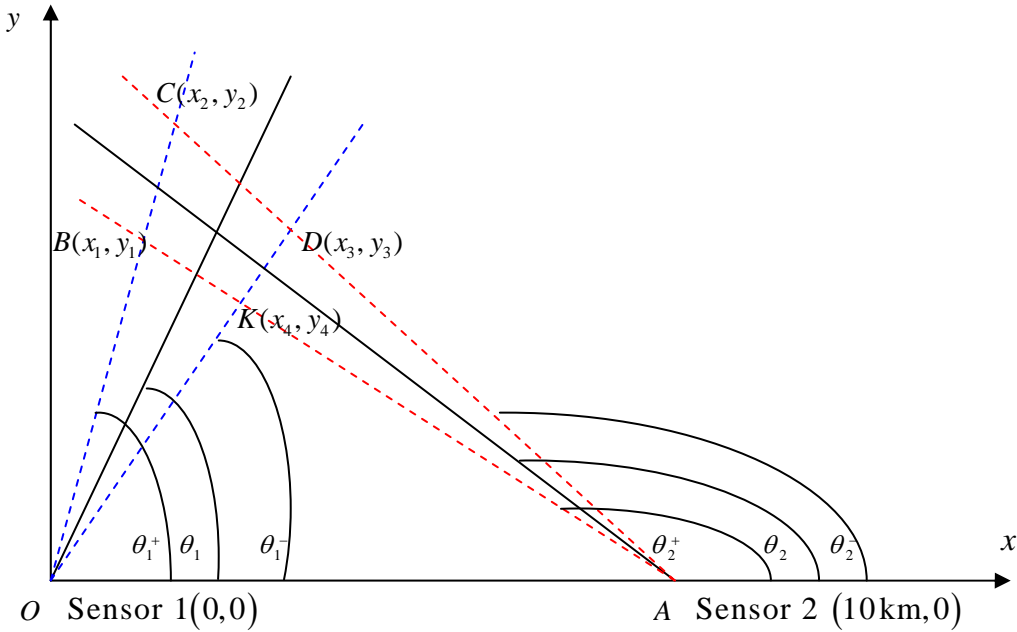


Figure 4.2: Encounter geometry of the initialization problem.

We suppose that the first set of the synchronous bearings from our IR sensors are θ_1 and θ_2 as shown in Figure 4.2. The reliability of the bearings depends on the quality of

the sensors, the sensors-target geometry and the distance between the sensors and the target. Since we examine the general case of the problem of initialization, we suppose that the sensors we use give a random error in bearing of maximum magnitude of approximately 2° . This error is considered very high for sensors designed to provide only the bearing, and it can be positive or negative.

So, examining sensor 1, the angular real position of the target must be between:

$$\theta_1^- \leq (x_{true}, y_{true}) \leq \theta_1^+, \quad (4.1)$$

where

$$\theta_1^- = \theta_1 - |\text{rand}(0,1) \cdot 2^\circ|, \quad (4.2)$$

$$\theta_1^+ = \theta_1 + |\text{rand}(0,1) \cdot 2^\circ|, \quad (4.3)$$

while bearings θ_1^- and θ_1^+ are shown in Figure 4.2 with the blue dashed line.

Treating the sensor 2 case, using the methodology used for sensor 1, we observe that the target must be inside the quadrilateral $BCDK$. In order to find the coordinates of $BCDK$ we apply Euclidian geometry to each triangle of Figure 4.2. So, examining triangle OBA and applying the sine law, we get:

$$\frac{\sin(\theta_1^+)}{AB} = \frac{\sin(\pi - \theta_2^+)}{OB} = \frac{\sin(\theta_3^l)}{OA}, \quad (4.4)$$

where AB , OB , OA are the lengths of the sides of the triangle as shown in Figure 4.2 while θ_3^l refers to the third angle of the triangle, namely angle $\angle OBA$. From Equation (4.4) we can find the length OB as:

$$OB = OA \frac{\sin(\pi - \theta_2^+)}{\sin(\theta_3^l)}, \quad (4.5)$$

where OA is the distance of the two sensors while angle θ_3^l is obtained since:

$$\theta_3^l = \pi - \theta_1^+ - (\pi - \theta_2^+) = \theta_2^+ - \theta_1^+. \quad (4.6)$$

Obtaining the length of OB we can find the coordinates using:

$$x_1 = OB \cos(\theta_1^+) = OA \frac{\sin(\theta_2^+) \cos(\theta_1^+)}{\sin(\theta_2^+ - \theta_1^+)}, \quad (4.7)$$

$$y_1 = OB \sin(\theta_1^+) = OA \frac{\sin(\theta_2^+) \sin(\theta_1^+)}{\sin(\theta_2^+ - \theta_1^+)} \quad (4.8)$$

We observe that finding the coordinates of point B involves only the sensor distance and the uncertainty bearings obtained by the two sensors. Following the same procedure the coordinates of point C are given by:

$$x_2 = OC \cos(\theta_1^+) = OA \frac{\sin(\theta_2^-) \cos(\theta_1^+)}{\sin(\theta_2^- - \theta_1^+)}, \quad (4.9)$$

$$y_2 = OB \sin(\theta_1^+) = OA \frac{\sin(\theta_2^-) \sin(\theta_1^+)}{\sin(\theta_2^- - \theta_1^+)} \quad (4.10)$$

For the coordinates of point D our calculations give:

$$x_3 = OD \cos(\theta_1^-) = OA \frac{\sin(\theta_2^-) \cos(\theta_1^-)}{\sin(\theta_2^- - \theta_1^-)}, \quad (4.11)$$

$$y_3 = OD \sin(\theta_1^-) = OA \frac{\sin(\theta_2^-) \sin(\theta_1^-)}{\sin(\theta_2^- - \theta_1^-)}, \quad (4.12)$$

while for point K

$$x_4 = OK \cos(\theta_1^-) = OA \frac{\sin(\theta_2^+) \cos(\theta_1^-)}{\sin(\theta_2^+ - \theta_1^-)}, \quad (4.13)$$

$$y_4 = OK \sin(\theta_1^-) = OA \frac{\sin(\theta_2^+) \sin(\theta_1^-)}{\sin(\theta_2^+ - \theta_1^-)}. \quad (4.14)$$

The next step involves determination of the maximum between the two diagonal lengths BD and CK . This determination is used for initialization of the covariance matrix P of the extended Kalman filter. The determination is illustrated in Figure 4.3.

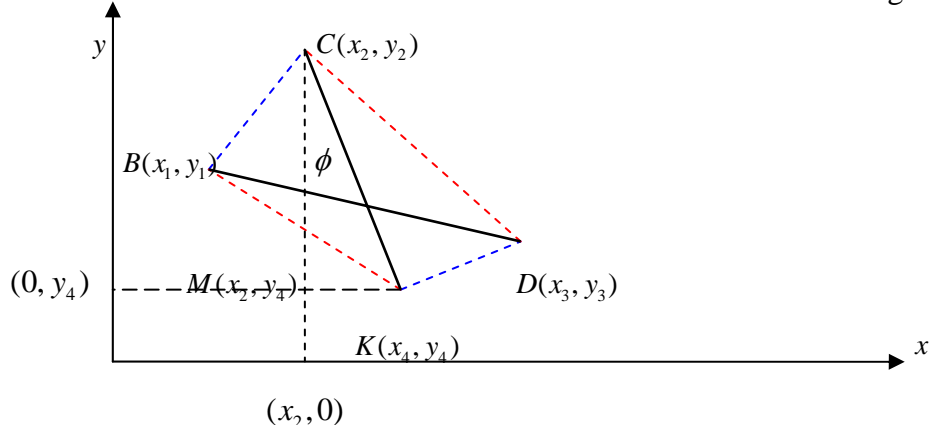


Figure 4.3: Encounter geometry for the determination of the diagonal lengths.

The diagonal length can be extracted either using the angle ϕ of the orthogonal triangle MCK whose inverse tangent is:

$$\phi = \tan^{-1} \left(\frac{x_4 - x_2}{y_2 - y_4} \right), \quad (4.15)$$

while the length CK according to this approach:

$$CK = \frac{|(x_4 - x_2)|}{\sin \left(\tan^{-1} \left(\frac{x_4 - x_2}{y_2 - y_4} \right) \right)}, \quad (4.16)$$

or using the well known approach for finding length:

$$BD = \sqrt{(x_1 - x_3)^2 + (y_1 - y_3)^2}. \quad (4.17)$$

Since the target can be anywhere inside the quadrilateral we assume without the loss of generality that it is located at:

$$x_t = \frac{x_1 + x_2 + x_3 + x_4}{4}, \quad (4.18)$$

$$y_t = \frac{y_1 + y_2 + y_3 + y_4}{4}. \quad (4.19)$$

We have implemented the above considerations in Matlab and we have produced Figure 4.4, for the target initialization:

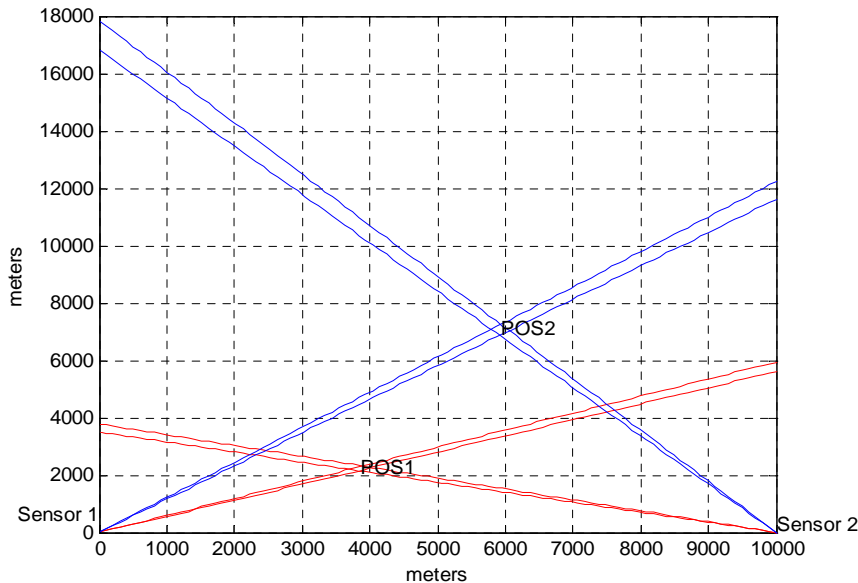


Figure 4.4: Matlab initialization using two sets of synchronous bearings.

The position of the target during the first and the second time that the bearings took place is illustrated in Figure 4.5:

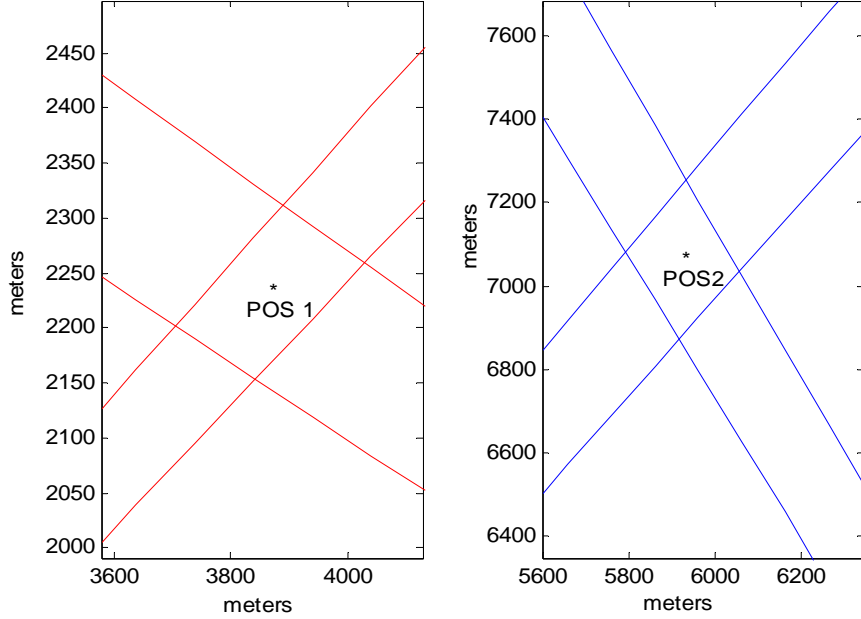


Figure 4.5: The position of the target is located inside the uncertainty bearing box.

D. EXTENDED KALMAN FILTERING CONSIDERATIONS

1. General

The problem considered in the bearing-only tracking is that the target motion is modeled in linear Cartesian coordinates, while the measurements are in polar coordinates. We begin by assuming the following non-linear discrete-time system:

$$\begin{aligned} x(k+1) &= f(k, x(k)) + g(k, x(k))v_k, \\ z(k) &= h(k, x(k)) + \omega_k, \end{aligned} \quad (4.20)$$

where x provides the target position data, z is the measurement, f and h are non-linear vector-valued functions, g is a non-linear matrix valued function and v_k , ω_k are uncorrelated Gaussian processes.

According to [28-30], it can be proved that the prediction using an extended Kalman filter is given by:

$$\hat{x}_{k+1|k} = f(k, \hat{x}_{k|k}), \quad (4.21)$$

$$P_{k+1|k} = F_k P_{k|k} F_k' + G_k Q_k G_k', \quad (4.22)$$

where $\hat{x}_{k+1|k}$ is the state vector at time $k+1$ given its value at time k , $P_{k+1|k}$ is the covariance prediction matrix at time $k+1$ given its value at time k , F_k and F'_k are the gradient and the transpose gradient of $f(k, \hat{x}_{k|k})$, G_k and G'_k are the zero order term for $g(k, \hat{x}_{k|k})$ evaluated at $\hat{x}_{k|k}$ and its transpose, respectively and, finally, Q_k is a matrix related to the noise inserted in the system.

We define Q_k according to [27] as:

$$Q_k = q^2 Q_i \quad (4.23)$$

where Q_i is the sampling interval matrix and q arbitrary chosen parameter of the design [30].

The update of the measurement according to [28, 29], can be expressed as:

$$\hat{x}_{k+1|k+1} = \hat{x}_{k+1|k} + K_{k+1} (z_{k+1} - h(k+1, \hat{x}_{k+1|k})), \quad (4.24)$$

$$P_{k+1|k+1} = (I - K_{k+1} H_{k+1}) P_{k+1|k} (I - K_{k+1} H_{k+1})' + K_{k+1} H_{k+1} K'_{k+1}, \quad (4.25)$$

where z_{k+1} is the measurement at time $k+1$, I stands for the associated to the problem identity matrix, H_{k+1} is the gradient of $h(k+1, \hat{x}_{k+1|k})$ and K_{k+1} is defined as:

$$K_{k+1} = P_{k+1|k} H'_{k+1} (H_{k+1} P_{k+1|k} H'_{k+1} + R_{k+1})^{-1}, \quad (4.26)$$

where R_{k+1} is associated to the uncertainty of the measurement at time $k+1$.

2. Bearing Tracking Expansion of EKF

The initialization in the EKF BOT case provides the vector of the two positions of the target after the second set of the synchronous bearings. This vector is:

$$x = (x_2 \ y_2 \ x_1 \ y_1)^T, \quad (4.27)$$

where x_2, y_2, x_1, y_1 are the estimated possible positions of the target obtained during the initialization process by the two sets of the tautochronous bearings. Since our state vector is in the form:

$$\hat{x} = (x \ v_x \ y \ v_y)^T, \quad (4.28)$$

where x, y is the position of the target and v_x, v_y the associated velocity, we use matrix D to obtain:

$$\hat{x} = Dx, \quad (4.29)$$

where the matrix D is defined as:

$$D = \begin{pmatrix} 1 & 0 & 0 & 0 \\ 1/dt & 0 & -1/dt & 0 \\ 0 & 1 & 0 & 0 \\ 0 & 1/dt & 0 & -1/dt \end{pmatrix}, \quad (4.30)$$

where dt is the time between the measurements.

The initialization of the covariance matrix P involves the maximum diagonals of the quadrilaterals and it is given according to [29, 30] by:

$$P_{initial} = \begin{pmatrix} d_2^2 & 0 & 0 & 0 \\ 0 & d_2^2 & 0 & 0 \\ 0 & 0 & d_1^2 & 0 \\ 0 & 0 & 0 & d_1^2 \end{pmatrix}, \quad (4.31)$$

where d_1 is the maximum distance of the diagonals of the quadrilateral formed by the first set of bearings, while d_2 refers to the second. During the EKF update and for the rest of the calculation the covariance matrix P is obtained by Equation (4.25).

The bearing-only measurements are θ angle measurements, so they can be expressed by:

$$z(k) = \theta(x(k)) + \omega_k. \quad (4.32)$$

where

$$\theta(x(k)) = \arctan\left(\frac{x_k}{y_k}\right). \quad (4.33)$$

The gradient of $h(x) = \theta(x)$ for the bearing-only measurements can be expressed by the following matrix:

$$H_k = \frac{\partial \theta(x)}{\partial x} = \begin{pmatrix} -\frac{y}{x^2 + y^2} & 0 & \frac{x}{x^2 + y^2} & 0 \end{pmatrix}, \quad (4.34)$$

where x and y are obtained by Equation (4.27).

3. Maneuvering Target Considerations

According to [29] and [30], in the maneuvering case target, the equations of measurement and update do not change. However, the transition matrices should be calculated as:

$$F^{(j)} = \begin{pmatrix} 1 & \frac{\sin(\omega\Delta)}{\omega} & 0 & \frac{1-\cos(\omega\Delta)}{\omega} \\ 0 & \cos(\omega\Delta) & 0 & -\sin(\omega\Delta) \\ 0 & \frac{1-\cos(\omega\Delta)}{\omega} & 1 & \frac{\sin(\omega\Delta)}{\omega} \\ 0 & \sin(\omega\Delta) & 0 & \cos(\omega\Delta) \end{pmatrix}, \quad (4.35)$$

where ω is the turn rate and Δ is the sampling interval. The determination of $F^{(j)}$ is possible by application of simple target motion analysis for a rotating mass around a complete circle. The turn can be either clockwise or anticlockwise.

4. Trajectory Error and Measurement-Angle Chi-square Formulation

The error is determined by the difference between the trajectory that the EKF predicts and the real trajectory of the target:

$$\begin{pmatrix} x_{error} \\ y_{error} \end{pmatrix} = \begin{pmatrix} \hat{x} \\ \hat{y} \end{pmatrix} - \begin{pmatrix} x_{real} \\ y_{real} \end{pmatrix}, \quad (4.36)$$

where x_{error}, y_{error} are the difference between the predicted by the EKF \hat{x}, \hat{y} and the real coordinates x_{real}, y_{real} of the position of the target. As a consequence the total distance error is obtained by:

$$\text{Total Error} = \sqrt{\begin{pmatrix} x_{error} \\ y_{error} \end{pmatrix} \begin{pmatrix} x_{error} & y_{error} \end{pmatrix}}. \quad (4.37)$$

The Chi-Square values of the angle allow us to observe the angle variations during the measurements. These values according to [27] are obtained by:

$$\chi^2 = (z - \hat{z})' \cdot (H \cdot \hat{P} \cdot H' + R)^{-1} \cdot (z - \hat{z}), \quad (4.38)$$

where z is defined by Equations (4.32) and (4.33), \hat{z} is the non-linear angular measurement, H is the gradient defined by Equation (4.34), P is the covariance matrix and R involves the error of the measurement. In every sampling interval the χ^2 value changes since the measured angle of the target is different.

E. PROBLEM FORMULATION AND RESULTS

The mathematical considerations above are the basis of tracking a moving target both in a straight line and during a turn using either one or two sensors, with or without the presence of measurement noise. For the purpose of this thesis we simulated each case separately in Matlab, although only selected cases will be presented. Analytic information for the all the cases can be found in Appendix C. In our simulation we assumed that the position of the sensors and the bearing measurements were according to Figure 4.2. The initialization always takes place using two sensors since these are assumed stationary, but it is possible to use only one if a sensor motion is assumed. In this case the mathematical equations should be corrected in such way that the relative trajectory of the target-observer is taken under consideration [29].

1. Non-Maneuvering Target BOT using One or Two IR Sensors in Noise Presence

In the case of a non-maneuvering target the initialization of the filter takes place using both sensors, while during the tracking we can use either one or two without any difference in the results. The geometry is illustrated in Figure 4.6.

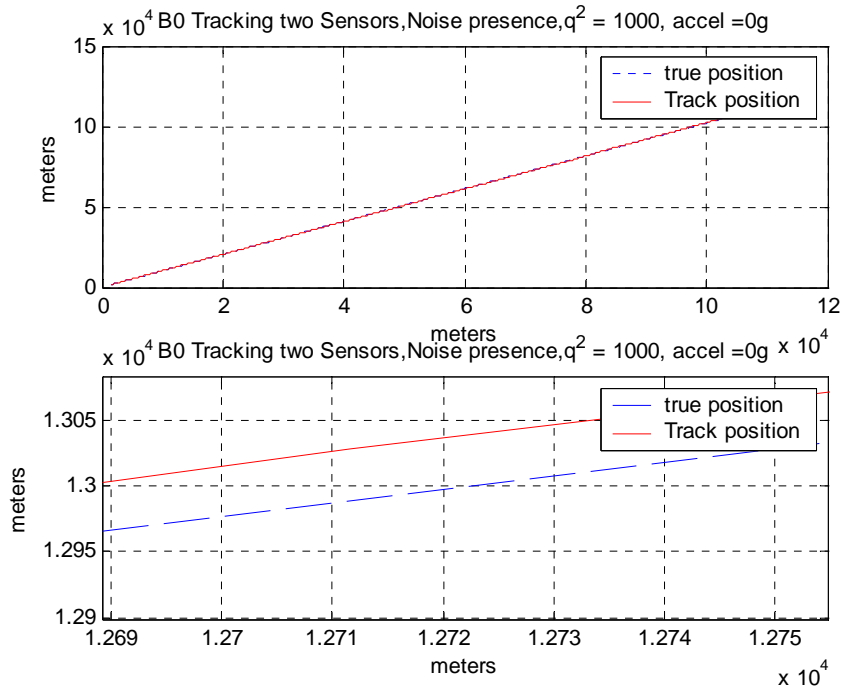


Figure 4.6: True position and track position of straight line moving target using two IR sensors in the presence of measurement noise.

The error during the tracking and the values of the measurement angle are presented in Figure 4.7.

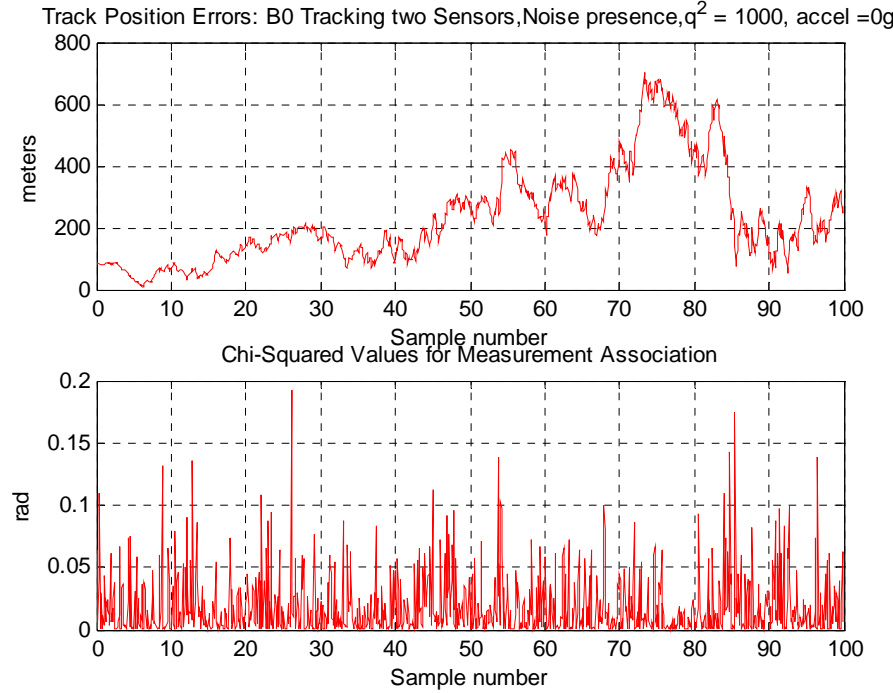


Figure 4.7: Track position error and chi-squared values vs. sample number for non-maneuvering target - two IR sensors in the presence of measurement noise.

In Figure 4.6 we observe that, when we use both sensors for initialization and tracking, the filter tracks the flying target almost from the starting point of our simulation run until the final point. We have selected a geometry for the simulation which does not offer advantage to the EKF since the target flies away from the sensors and the bearing angles are not perpendicular. Despite these facts, the filter error generally remains under 200 m for most of the simulation time, although there is an interval of 40 samples where the error increases.

In Figure 4.7 we also observe that the values of the chi-squared variable remain under 0.20 which means that the effort of the filter to correct the bearing angle and, hence, to obtain a more accurate position of the target is minimal. This means that the filter is unaware that there is a difference between the tracking position and the real position of the target. This result was expected since we are simulating a filter that tracks only

with angle measurements, so in a case when the EKF is used with radar sensor that provides range information, these effects are eliminated.

2. BOT of Low Maneuvering Target using IR Sensors in Noise Presence

In this case the target turn was simulated according to Equation (4.35). We will examine two cases in this category. The first case involves a smooth target turn of not more than $3 g$, while in the other case the target will execute a sharp high g turn. The geometry for the filter and the target for the first case are shown in Figure 4.8.

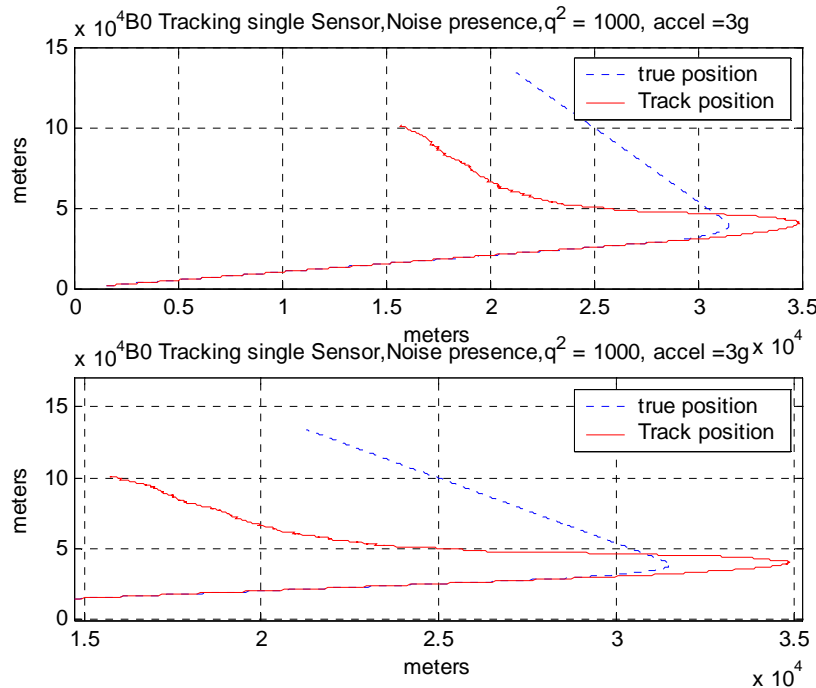


Figure 4.8: True position and track position of a low g turning target using one IR sensor in the presence of measurement noise.

From Figures 4.7 and 4.8 above we conclude that as long as the target flies on a straight course the single sensor filter responds positively. When the target starts its turn we observe a slow response time from the EKF which results in the loss of the target for almost 4 km . When the filter realizes that a turn has occurred, it turns sharply seeking for the true target track. The track subsequently generated by the EKF parallels the true target path, matching the true bearing closely but missing in range. So the filter tracks the target path only in bearing. This behavior appears because we applied the EKF algorithm to track a turning target using only one sensor so, once the sensor loses the real position

of a target can only recover the target's bearing, but not the distance. The error and the chi-squared graphs presented in Figure 4.9 supports the previous arguments.

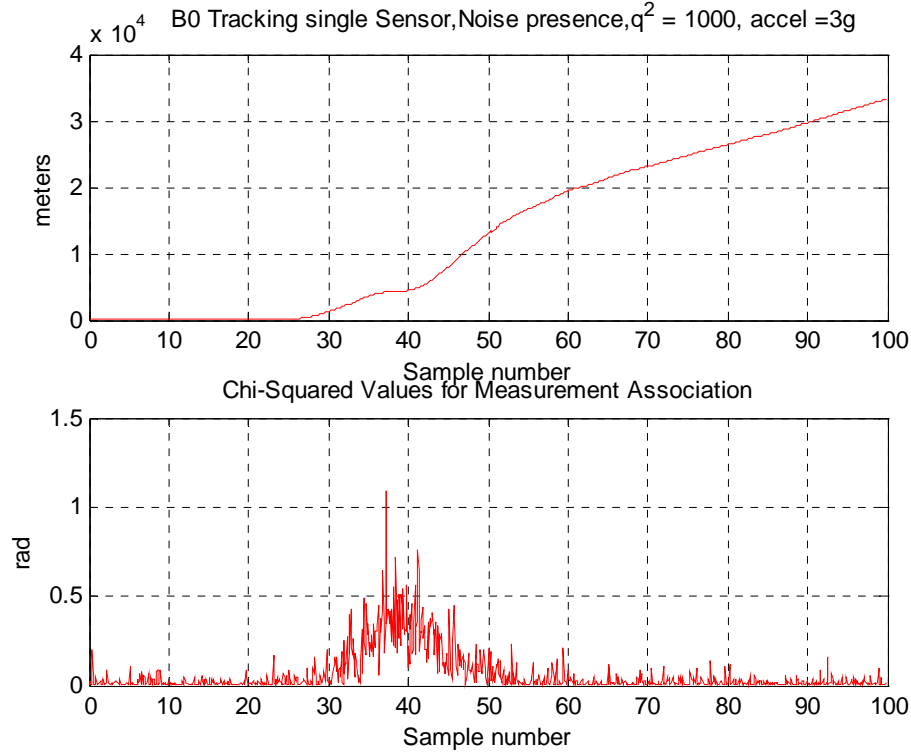


Figure 4.9: Track position error and chi-squared values vs. sample number for low g maneuvering target - single IR sensor in the presence of measurement noise.

In Figure 4.9 we observe that using both sensors for initialization and a single sensor for tracking results in an increasing error to almost 700 meters before the target starts its turn. The filter tracks the target almost from the starting point of our simulation run until the final point. The tracking in this case is characterized as low quality since the true position of the target after the turn is never obtained. At sample 28, as we clearly observe, the error starts growing and, at the end of the simulation, it becomes almost 30 km. We also observe that the values of the chi-squared remain under 0.10 when the target is out of the turn loop and close to 0.50 radians when the target is inside the turn. The fact that the values are kept low means that the filter assumes that it is tracking the target accurately after the turn. This is true in bearing but not in range. Again since we combine the EKF with a single angle tracking sensor, the algorithm is unable to regain

the real position. The tracking results become worse when the simulation involves higher random errors and sharper turns, as we will present.

To improve the performance in the case of a 3g turn, we employed both sensors in the tracking effort. The results are shown in Figures 4.10 and 4.11.

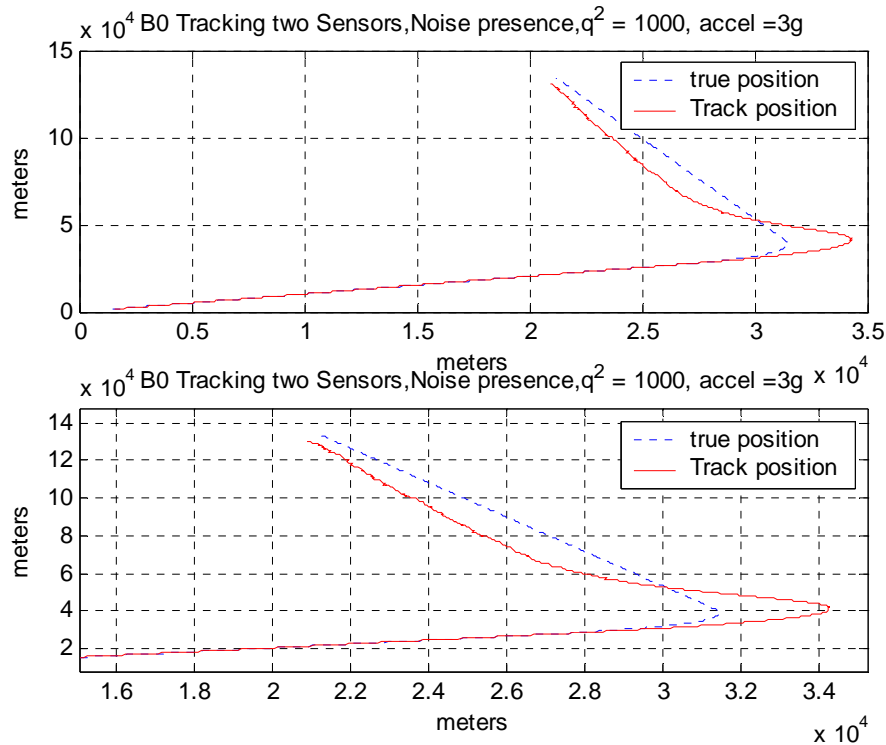


Figure 4.10: True position and track position of a low g turning target using two IR sensors in the presence of measurement noise.

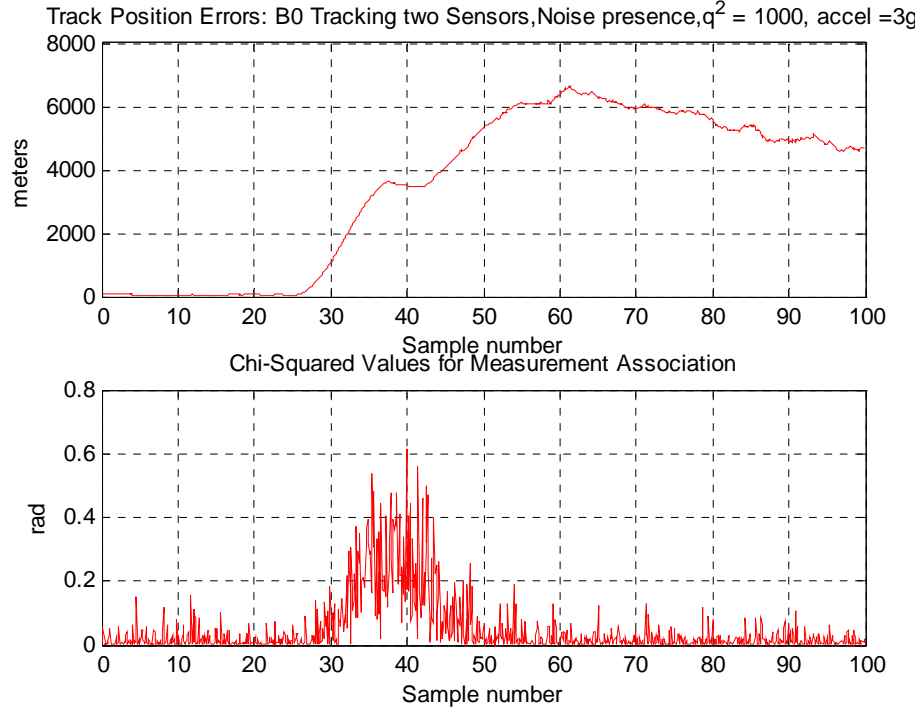


Figure 4.11: Track position error and chi-squared values vs. sample number for low g maneuvering target – two IR sensors in the presence of measurement noise.

We observe that using the second sensor has improved the tracking conditions; namely, it has reduced the resulting error from 30 km to almost 4 km. If the simulation was free to run for a longer sampling time, the real position and the tracking position would eventually converge. At the same time the chi squared values were found almost the same.

3. BOT of High Maneuvering Target using IR Sensors in Noise Presence.

We present two sub-cases in BOT of a high maneuvering target. Firstly, the concept of EKF angle tracking using one sensor. In this case, a turn of no more than 9 g is presented since, with the particular geometry and with the particular initialization bearings and sampling time, higher turns result in a breakdown of the EKF algorithm. So employing a 9 g turn of a target, which is moving with velocity 339 m/s, results to the geometry of Figure 4.12.

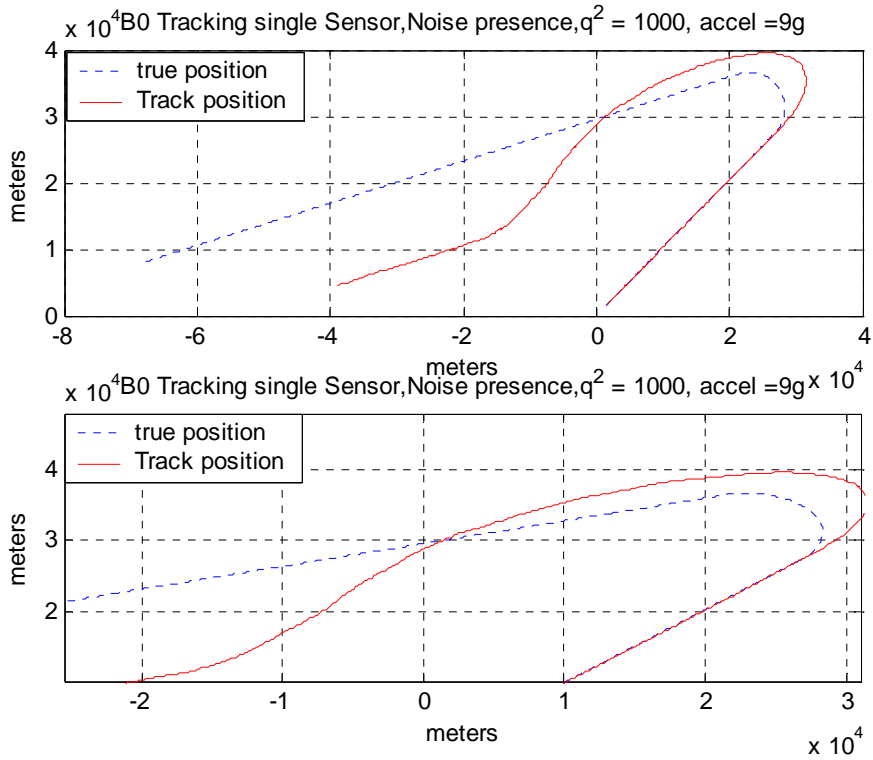


Figure 4.12: True position and track position of a high g turning target using one IR sensor in the presence of measurement noise.

We observe that the single sensor combined with the EKF tracks the target reliably when we have a straight-line motion, but when the turn takes place it follows with a time delay and finally manages to recover the correct bearing tracking. The associated error and the values of chi-squared are illustrated in Figure 4.13.

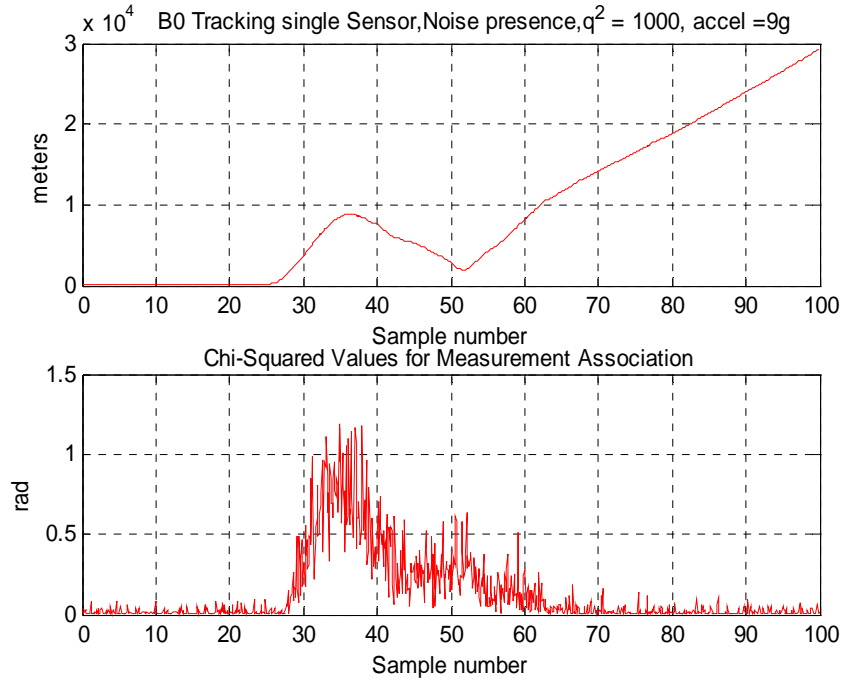


Figure 4.13: Track position error and chi-squared values vs. sample number for high g maneuvering target – single IR sensor in the presence of measurement noise.

Figure 4.13 shows that the error is kept small before the target starts the turn, it grows to almost 8km during the turn, then it reduces due to the convergence of the real and the estimate position but finally it grows due to the divergence of the two tracks. The chi-squared values are also higher compared to the other cases due to the high g turn, so we observe that the values are over 1 during the turn, while for the half of the simulation time, they are close to 0.1.

Second, in order to obtain more reliable results we employ the second sensor in the tracking effort. We expect the performance of our system to be improved similar to the results of the low g turning target. In fact, the tracking results turned out to be better than expected, meaning that the IR sensors combined with the EKF algorithm track the target with small error. The explanation of the reliable tracking is that in this case the target follows a reverse course towards our system. This means that the distance to our sensor system is reduced, so the suggested rule that the tracking distance should not be much higher than the sensor distance is satisfied [30]. The results and the encounter geometry are shown in Figures 4.14 and 4.15.

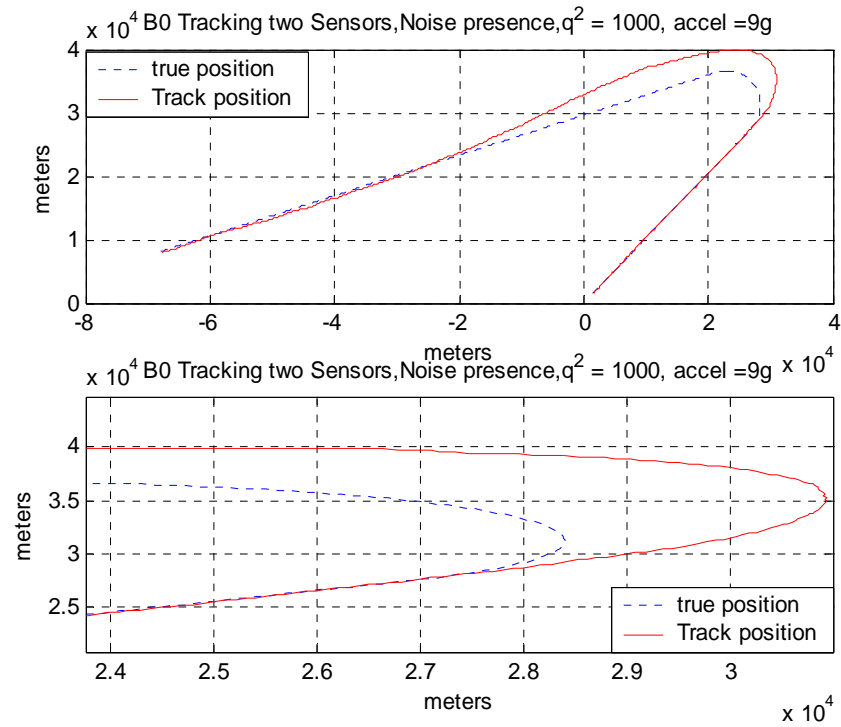


Figure 4.14: True position and track position of a high g turning target using two IR sensors in the presence of measurement noise.

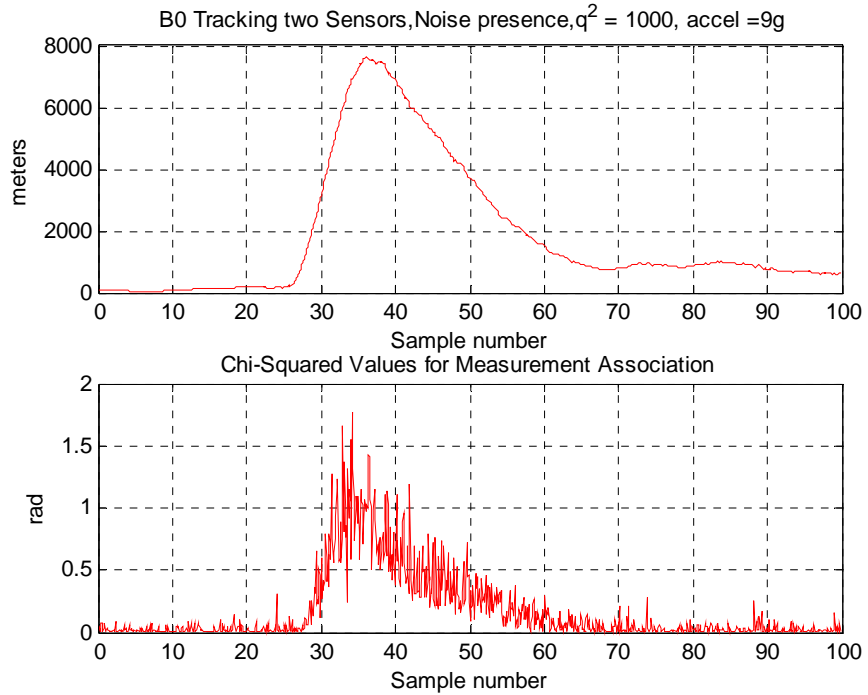


Figure 4.15: Track position error and chi-squared values vs. sample number for high g maneuvering target – single IR sensor in the presence of measurement noise.

Figure 4.15 illustrates that the error remains high during the turn, but it is also significantly reduced compared to all the previous cases. In addition, the filter with the two sensors recovers quickly after the turn and seeks the real path of the target. The chi-squared values are much higher than all the previous cases but they last for shorter sample periods, which means that the tracking effort is large during the turn and minimal at all the other times.

F. SUMMARY

We have investigated a classical algorithm applied to two modern sensors. It is obvious that the results are significantly improved in the case where two sensors are used for tracking. In real applications more than two sensors may be used at the same time. In addition, three dimensional cases are examined in the literature [31]. Other techniques not explored in the present thesis may also be used. Some alternative methods involve particle filters [29], and combined IR and radar sensors with EKF application [32].

THIS PAGE INTENTIONALLY LEFT BLANK

V. CONCLUSIONS AND FUTURE WORK.

We have modeled the behavior of QWIPs in various conditions of operation through a computer algorithm and we have simulated the behavior of an infrared sensor in the bearing-only tracking application. Our goal, optimization of the performance of QWIPs and their application to target tracking, was achieved by implementing in a computer fundamental quantum mechanical equations and nonlinear control theory, respectively. Our conclusions are summarized per chapter along with suggestions for future work.

A. CONCLUSIONS

In Chapter II we began with the fundamental quantum mechanical concept, the Schrödinger equation. By application of this equation in the quantum structures of interest we studied their behavior. Then, using a well known mathematical technique, the method of the transfer matrix (TMM), we were able, not only to have our equations in a consistent form, but also to implement them inside the simulation program and study them. During the program simulations we were able to observe theoretically predicted and experimentally observed concepts, such as tunneling through the quantum well barrier and leakage current. Finally we developed a set of programming functions using asymptotic expressions of Airy's functions to study the behavior of our structure in the case of very low biases.

Chapter III provided a discussion of the fabricated QWIP. A single quantum well of the multi-quantum structure was examined in various cases. Namely, we studied the behavior of bound, quasibound and continuous states in the case of forward and reverse bias, both above and below the arbitrarily placed threshold and in the case of absence of electric field. We examined the concept of bound and continuous coefficients of the wavefunctions used in the TMM and we developed their value in every region of the well and for the bias used. In addition, we examined the performance of the detector by studying its oscillator strength using characteristic biases and we found the theoretically predicted rapid oscillations when we apply very low biases. Moreover, we compared the experimental and the simulation results and we concluded that they match. Finally, we developed and simulated the concept of photocurrent in the quantum well.

Finally, Chapter IV presented the basic concepts of nonlinear extended Kalman filtering. We developed the mathematical model of initialization of the filter using two sets of synchronous bearings. The algorithm was initialized by the user and, based in that geometry, various cases were studied, either using one, or two sensors with and without the presence of ambient noise. Results and conclusions were made for the optimal design of a bearing only tracking system based on IR sensors.

B. FUTURE WORK

There are many concepts based on this work that further research is recommended. For instance, using the simulation program developed, we can design the desired QWIP, predicting its behavior in the laboratory. In addition, we can predict the necessary bias to observe the theoretically predicted constructive interference oscillations. Furthermore, we can design the optimal quantum well to minimize the quantum tunneling and to maximize the photocurrent before testing it in the laboratory.

Finally, it is recommended to expand the EKF simulation program, using the same initialization process, so that the number of the sensors exceeds two. In that way we can simulate sensors arrays and the expected tracking results will be better. Furthermore we can expand the simulation into three dimensional cases. Concluding, it is strongly recommended to study similar cases using particle filters and compare the results with the EKF, especially in three dimensional and in terrain mapping cases using synchronous or asynchronous bearings.

APPENDIX A: QWIP SIMULATION PROGRAMS

In the present Appendix we present selected programs of the simulation of the *InGaAs / AlGaAs* quantum well. The core of the simulation is [E_InGaAs.m](#). Once this program is executed, every other sub-matlab file is called automatically.

```
% *****NPS*****
% **Simulation Of Performance Of Infrared Photodetectors*****
% E_InGaAs
%LT Psarakis Eftychios Hellenic Navy
clc
clear all
global E E_c
%defining the constants
hbar = 1.05557e-34; %[J*s]
m0 = 9.10939e-31; %[kg]
q = 1.60218e-19; %[C]
F = input('Electric Field in [V/m]:      ');
% Percentage in region
x=[0,0.3,0.1,0];
% Width of the region
width=[inf,40,40,inf];
ii=4;
for tt=1:ii
    %X(i)=input('Percentage of Al (0-1) in region ');
    %width(i) = input('Give width: ');
end
y = 0;    %Initial value of y & z to correct the logic of the later condition
z = 0;
for tt=2:3
    L(1) = width(1)*1e-10;
    L(2) = width(2)*1e-10;
    L(tt+1) = (width(tt)+width(tt+1))*1e-10;
end
if F>-2*10^5 & F<10^5
    %EwellNoBiasAiry
    EwellsmallBiasAiry
    %EwellNoBias
    break
end
if F>=10^5
    for tt=1:4
        if width(tt)==inf
            Z_dir(tt)=0;
        else
```



```

E_c =min(V(1),V(4))-03;
Vb=input('give Vb in eV :');
disp('The continuus states energy are:')
% dE_c = 1.2490e-004;
dE_c=(Vb-E_c)/1001;
while E_c < Vb
E_c = E_c + dE_c;
for jj=1:4
eta(jj) = (E_c - V(jj));
end
for jj=1:4
Alpha(jj) = -C(jj)*(F*Z_dir(jj) + eta(jj));
Alphaout(ll,jj)=[Alpha(:,jj)];
end
for jj=1:3
alpha(1)=0;
alpha(jj+1)= -C(jj+1)*(F*Z_dir(jj) + eta(jj+1));
alphaout(ll,jj+1)=[alpha(:,jj+1)];
end
for jj=1:3
m11_c=(pi)*(airy(0,alpha(jj+1))*airy(3,Alpha(jj))-sigma(jj)*(airy(2,Alpha(jj))*airy(1,alpha(jj+1))));
m12_c= (pi)*(airy(2,alpha(jj+1))*airy(3,Alpha(jj))-sigma(jj)*(airy(2,Alpha(jj))*airy(3,alpha(jj+1))));
m21_c= (pi)*(sigma(jj)*(airy(0,Alpha(jj))*airy(1,alpha(jj+1)))-airy(1,Alpha(jj))*airy(0,alpha(jj+1)));
m22_c= (pi)*(sigma(jj)*(airy(0,Alpha(jj))*airy(3,alpha(jj+1)))-airy(1,Alpha(jj))*airy(2,alpha(jj+1)));
%checking the output data
m11out_c(ll,jj)=[m11_c];
m12out_c(ll,jj)=[m12_c];
m21out_c(ll,jj)=[m21_c];
m22out_c(ll,jj)=[m22_c];
M_c(:,jj)=[m11_c;m12_c;m21_c;m22_c];
end
%finding Mn
M12_c=[M_c(1,1),M_c(2,1);M_c(3,1),M_c(4,1)],[M_c(1,2),M_c(2,2);M_c(3,2),M_c(4,2)];
M23_c=[M_c(1,2),M_c(2,2);M_c(3,2),M_c(4,2)],[M_c(1,3),M_c(2,3);M_c(3,3),M_c(4,3)];
M123_c=[M_c(1,1),M_c(2,1);M_c(3,1),M_c(4,1)],[M_c(1,2),M_c(2,2);M_c(3,2),M_c(4,2)],[M_c(1,3),M_c(2,3);M_c(3,3),M_c(4,3)];
disp(E_c)
Eout_cont(ac) = E_c;
Epsi_cont;
hold on

```



```

% %*****BOUND STATES*****%
% %*****%
% %*****%
clear a n ll dE E eta alpha Alpha E;
a =1;
n = 0;
ll=1;
dE = 5*10^-4;
E = DD;
%Evaluate the energy from the bottom to the top of the well;
while E < V2_-dE
if E > V2_-10^-3
    dE = 10^-6;
end
E = E + dE;
for tt=1:4
eta(tt) = (E - V(tt));
end
for jj=1:4
Alpha(jj) = -C(jj)*(F*Z_dir(jj) + eta(jj));
end
for jj=1:3
alpha(jj+1)= -C(jj+1)*(F*Z_dir(jj) + eta(jj+1));
end
for jj=1:3
    m11=          (pi)*(airy(0,alpha(jj+1))*airy(3,Alpha(jj))-
sigma(jj)*(airy(2,Alpha(jj))*airy(1,alpha(jj+1)))); -
    m12=          (pi)*(airy(2,alpha(jj+1))*airy(3,Alpha(jj))-
sigma(jj)*(airy(2,Alpha(jj))*airy(3,alpha(jj+1)))); -
    m21=          (pi)*(sigma(jj)*(airy(0,Alpha(jj))*airy(1,alpha(jj+1))-
airy(1,Alpha(jj))*airy(0,alpha(jj+1)))); -
    m22=          (pi)*(sigma(jj)*(airy(0,Alpha(jj))*airy(3,alpha(jj+1))-
airy(1,Alpha(jj))*airy(2,alpha(jj+1)))); -
%checking the output data
m11out(ll,jj)=[m11];
m12out(ll,jj)=[m12];
m21out(ll,jj)=[m21];
m22out(ll,jj)=[m22];
M(:,jj)=[m11;m12;m21;m22];
end
%finding Mn
M12=[M(1,1),M(2,1);M(3,1),M(4,1)]*[M(1,2),M(2,2);M(3,2),M(4,2)];
M23=[M(1,2),M(2,2);M(3,2),M(4,2)]*[M(1,3),M(2,3);M(3,3),M(4,3)];
M123=[M(1,1),M(2,1);M(3,1),M(4,1)]*[M(1,2),M(2,2);M(3,2),M(4,2)]*[M(1,3),
M(2,3);M(3,3),M(4,3)];

```

```

M22 = real(M123(2,2)); %in case we have three matrices
%checking the output data
M22out(ll)=[M22];
EM22(ll)=[E];
%%%%%%%%%end of check%%%%%%%%%%%%%
z = y;
y = M22;
ll=ll+1;
if z*y < 0      %Determine the approximate eigen energy first
    n = n +1;
    if n < 2      %Increase the acuaracy of eigen energy
        E = E-dE;
        dE = 1e-6;
        y = z;
    end
end
if n > 1
    disp('The ground state energy is:')
    disp(E)
    Eout(a) = E;  %Stores energy levels into an array
    Epsi_bound;
    dE = 5e-4;
    n = 0;
    hold on
    r = 0:.1:width(2)+(a-1)*width(3);
    if a < 3
        plot(r,Eout(a),'r')
        text(0,Eout(a)+.01,['E_',num2str(a),' = ',sprintf('%4.3f',Eout(a)), ' eV'])
        plot((X*1e10),(real(Psi1_bound(a,:)/5e5)+Eout(a)),'k')
        plot((Y*1e10),(real(Psi2_bound(a,:)/5e5)+Eout(a)),'k')
        plot((Z*1e10),(real(Psi3_bound(a,:)/5e5)+Eout(a)),'k')
        plot((T*1e10),(real(Psi4_bound(a,:)/5e5)+Eout(a)),'k')
    end
    a = a+1;
end
end
end
ZETA;
% ****
% *****oscillator strength*****
% ****
for ai=1:ac-1;
    DE(ai)=(Eout_cont(ai)-Eout);
    f_oscil(ai)=2*(m_eff(1))/(hbar^2).*DE(ai)*q.*Zeta_final(ai)';
end
figure
plot(DE,real(f_oscil))

```

```

xlabel('DeltaE')
ylabel('oscillator strength f')
title('oscillator strength Vs |DeltaE')
for ai=1:ac-1;
Prod_f_oscil_DOS(ai)=f_oscil(ai).*DOS(ai)*q;
OSCSTR(ai)=f_oscil(ai).*DOS(ai)*q*dE_c;
OSCSTR_INTEG=sum(OSCSTR);
end
figure
plot(DE,real(Prod_f_oscil_DOS))
xlabel('DeltaE')
ylabel('(oscillator strength)*(density of states)')
title('oscillator strength multiplied by density of states Vs |DeltaE')
disp('The (oscillator strength)*(density of states) integral is')
round(OSCSTR_INTEG)
% % ****absorption*****
% % ****absorption*****
% % ****absorption*****
q = 1.60218e-19; %[C]
h=6.626*10^-34;
m_eff(1)=1.0e-031*0.6103;
N_d=1e24;
e0=8.85e-12;
n_r=3.5;
c=3*10^8;
Cb_c=pi*(N_d*q*hbar^2)./(2*m_eff(1).^2*e0*n_r*c);
total_length=380*10^-10;
for kk=1:ac-1
beta4=((hbar^2)/(2*m_eff(4)*F))^(1/3);
%region IV
quantum_eff=total_length*Cb_c.*Prod_f_oscil_DOS;
J4R(kk)=hbar/(4*m_eff(4)*pi*abs(beta4))*(b3_cont(kk).*A4(kk)+b3_cont(kk).*(i*B4(kk))).*conj((b3_cont(kk).*A4(kk)+b3_cont(kk).*(i*B4(kk)))*q;
% I=J_total*Area;
end
J_total=quantum_eff.*J4R.*q;
figure
plot((h*c)./(q*DE),real(J_total)/max(real(J_total)), 'b')
hold on
plot((h*c)./(q*DE),real(Cb_c*Prod_f_oscil_DOS)./max(real(Cb_c*Prod_f_oscil_DOS)), 'r')
xlabel('Wavelength-\mu m')
ylabel('Normalized photocurrent, Normalized absorption')
legend('photocurrent','absorption')

```

```

% *****NPS*****
% **Simulation Of Performance Of Infrared Photodetectors*****
% EwellNoBias
% LT Psarakis Eftychios Hellenic Navy
hbar = 1.05557e-34; %[J*s]
m0 = 9.10939e-31; %[kg]
q = 1.60218e-19; %[C]
F =F;
% Percentage in region
x=[0,0.3,0.1,0];
% Width of the region
width=[inf,40,40,inf];
ii=4;
y = 0;
z = 0;
for tt=2:ii-1
L(1) = width(1)*1e-10;
L(2) = width(2)*1e-10;
L(tt+1) = (width(tt)+width(tt+1))*1e-10;
end
eg(1) = 1.519 + 1.247.*x(1);
eg(2) = 1.519 - 1.102.*x(2);
eg(3) = 1.519 - 1.102.*x(3);
eg(4) = 1.519 + 1.247.*x(4);
eg=[eg(1) eg(2) eg(3) eg(4)];
V(1)=0.62*(eg(1)-eg(2));
V(2)=0;
V(3)=0.62*(eg(3)-eg(2));
V(4)=0.62*(eg(4)-eg(2));
V=[V(1),V(2),V(3),V(4)];
for jj=1:4
m_eff(jj) = 1/((x(jj)/(0.028*m0)) + ((1-x(jj))/(0.067*m0)));
end
for t=1:ii
if width(t)==inf
Z_dir(t)=0;
else
Z_dir(t) = L(t);
end
end
ac =1;
n = 0;
ll=1;
%by varing dE we can ajust the number of states found
E =max(V(1),V(4));

```

```

jj=0;
Vb=input('give Vb in eV :')
dE_c=10^-4;
disp('The continuus states energy are:')
while E<Vb
E=E+dE_c;
for nn=1:4
k(nn)=sqrt((2*m_eff(nn)*(E-V(nn))*q)/hbar^2);
end
for nn=1:3
XI(nn)=(k(nn)*m_eff(nn+1))/(k(nn+1)*m_eff(nn));
end
for jj=1:3
m11_c= 1/2*((1+XI(jj))*exp(i*(k(jj)-k(jj+1))*Z_dir(jj)));
m12_c= 1/2*((1-XI(jj))*exp(-i*(k(jj)+k(jj+1))*Z_dir(jj)));
m21_c= 1/2*((1-XI(jj))*exp(i*(k(jj)+k(jj+1))*Z_dir(jj)));
m22_c= 1/2*((1+XI(jj))*exp(-i*(k(jj)-k(jj+1))*Z_dir(jj)));
M_c(:,jj)=[m11_c;m12_c;m21_c;m22_c];
m11out_c(l1,jj)=[m11_c];
m12out_c(l1,jj)=[m12_c];
m21out_c(l1,jj)=[m21_c];
m22out_c(l1,jj)=[m22_c];
end
%finding Mn
M21_c=[M_c(1,2),M_c(2,2);M_c(3,2),M_c(4,2)],[M_c(1,1),M_c(2,1);M_c(3,1),M_c(4,1)];
M32_c=[M_c(1,3),M_c(2,3);M_c(3,3),M_c(4,3)],[M_c(1,2),M_c(2,2);M_c(3,2),M_c(4,2)];
M321_c=[M_c(1,3),M_c(2,3);M_c(3,3),M_c(4,3)],[M_c(1,2),M_c(2,2);M_c(3,2),M_c(4,2)][M_c(1,1),M_c(2,1);M_c(3,1),M_c(4,1)];
M22_c =real(M321_c(2,2));
%checking the output data
disp(E)
Eout_cont(ac) = E;
integration_cont;
hold on
r = 0:.1:width(2)+width(3);
plot(r,Eout_cont(ac),'r')
text(0,Eout_contt(ac)+.01,['E_',num2str(ac),'',
',sprintf('%4.3f',Eout_cont(ac)), ' eV'])
plot(reg1*10^10,(real(psi1_cont(ac)/5e5)+Eout_cont(ac)), 'k')
plot(reg2*10^10,(real(psi2_cont(ac)/5e5)+Eout_cont(ac)), 'k')
plot(reg3*10^10,(real(psi3_cont(ac)/5e5)+Eout_cont(ac)), 'k')
%',plot(reg4*10^10,(real(psi4_cont(ac)/5e5)+Eout_cont(ac)), 'k')
ac=ac+1;

```

```

end
xlabel('X (Angstroms)')
ylabel('Potential Height (eV)')
title('Quantum Well')
% *****Well*****
% ****
hold on
x1 = -100:.1:0;
h1 = 0:.001:V(1);
plot(x1,(V(1)-F*(x1*1e-10))) %,'LineWidth',5)
x2 = 0:.1:width(2);
x3 = width(2):.1:(width(2)+width(3));
h2 = (-F*L(2)):0.001:(V(3)-(F*L(2)));
h3 = (V(3)-(F*L(3))):.001:(V(1)-(F*L(3)));
plot(x3,((V(3)-F*(x3*1e-10)))) %,'LineWidth',5)
x4 = (width(2)+width(3)):1:(width(2)+width(3)+100);
plot(x4,((V(1)-F*(x4*1e-10)))) %,'LineWidth',5)
x5 = 0:.1:(width(2)+width(3));
plot(x2,(-F*(x2*1e-10))) %,'LineWidth',5)
plot(0,h1) %,'LineWidth',8)
plot(width(2),h2) %,'LineWidth',3)
plot((width(2)+width(3)),h3) %,'LineWidth',5)
% ****
% ****bound states*****
a =1;
n = 0;
ll=1;
dE = 5*10^-4;
E = 0;
jj=0;
while E<max(V)
if E > max(V)-10^-3
    dE = 10^-6;
end
E=E+dE;
for nn=1:4
    k(nn)=sqrt((2*m_eff(nn)*(E-V(nn))*q)/hbar^2);
end
for nn=1:3
    XI(nn)=(k(nn)*m_eff(nn+1))/(k(nn+1)*m_eff(nn));
end
for jj=1:3
m11= 1/2*((1+XI(jj))*exp(i*(k(jj)-k(jj+1))*Z_dir(jj)));
m12= 1/2*((1-XI(jj))*exp(-i*(k(jj)+k(jj+1))*Z_dir(jj)));
m21= 1/2*((1-XI(jj))*exp(i*(k(jj)+k(jj+1))*Z_dir(jj)));

```

```

m22= 1/2*((1+XI(jj))*exp(-i*(k(jj)-k(jj+1))*Z_dir(jj)));
M(:,jj)=[m11;m12;m21;m22];
m11out(l1,jj)=[m11];
m12out(l1,jj)=[m12];
m21out(l1,jj)=[m21];
m22out(l1,jj)=[m22];
end
%finding Mn
M21=[M(1,2),M(2,2);M(3,2),M(4,2)]*[M(1,1),M(2,1);M(3,1),M(4,1)];
M32=[M(1,3),M(2,3);M(3,3),M(4,3)]*[M(1,2),M(2,2);M(3,2),M(4,2)];
M321=[M(1,3),M(2,3);M(3,3),M(4,3)]*[M(1,2),M(2,2);M(3,2),M(4,2)]*[M(1,1),
M(2,1);M(3,1),M(4,1)];
M22 =real(M321(2,2));
%checking the output data
M22out(l1)=[M22];
EM22(l1)=[E];
%%%%%%%%%%%%%end of check%%%%%%%%%%%%%
z=y;
y=M22 ;
l1=l1+1;
if z.*y < 0
    n = n +1;
    if n < 2      %Increase the acuaracy of eigen energy
        E = E-dE;
        dE = 1e-6;
        y = z;
    end
end
if n > 1
    disp('The ground state energy is:')
    disp(E)
    Eout(a) = E;
    xx=E;
    integration;
    dE = 5e-4;
    n = 0;
    hold on
    r = 0:.1:width(2)+(a-1)*width(3);
    Eout(a) = E;
    hold on
    if a<3
        plot(r,Eout(a),'r')
        text(0,Eout(a)+.01,['E_',num2str(a),' = ',sprintf('%4.3f',Eout(a)), ' eV'])
        plot(reg1*1e10,(real(Psi1_bound/5e5)+E),'k')
        plot(reg2*1e10,(real(Psi2_bound/5e5)+E),'k')
        plot(reg3*1e10,(real(Psi3_bound/5e5)+E),'k')
    end
end

```

```

    plot(reg4*1e10,(real(Psi4_bound/5e5)+E),'k')
end
a=a+1;
end
end
ZETA1;
% *****
% *****oscillator strength*****
% *****

for ai=1:ac-1;
    DE(ai)=(Eout_cont(ai)-Eout(1));
    f_oscil(ai)=2*(m_eff(1))/(hbar^2).*DE(ai)*q.*Zeta_final(ai)';
end
figure(2)
plot(DE,real(f_oscil))

xlabel('|\Delta E|')
ylabel('oscillator strength f')
title('oscillator strength Vs |\Delta E|')
for ai=1:ac-1;
    Prod_f_oscil_DOS(ai)=f_oscil(ai).*DOS(ai)*q;
    OSCSTR(ai)=f_oscil(ai).*DOS(ai)*q*dE_c;
    OSCSTR_INTEG=sum(OSCSTR);
end
figure(3)
plot(DE,real(Prod_f_oscil_DOS))
xlabel('|\Delta E|')
ylabel('oscillator strength)*(density of states)')
title('oscillator strength multiplied by density of states Vs |\Delta E|')
disp('The (oscillator strength)*(density of states) integral is')
round(OSCSTR_INTEG)

% *****
% **Simulation Of Performance Of Infrared Photodetectors*****
% integration
% LT Psarakis Eftychios Hellenic Navy
dx = 10^-11;
reg1= -300e-10:dx:0;
reg2 = 0:dx:L(1,2);
reg3 = L(1,2):dx:L(1,3);
reg4 = L(1,3):dx:(L(1,3)+300e-10);

A1=0;
B1=1;
A2=M(2,1);

```

```

B2=M(4,1);
A3=M21(1,2);
B3=M21(2,2);
A4=M321(1,2);
B4=0;
psi1_bound=A1*exp(i*k(1)*reg1)+B1*exp(-i*k(1)*reg1);
psi2_bound=A2*exp(i*k(2)*reg2)+B2*exp(-i*k(2)*reg2);
psi3_bound=A3*exp(i*k(3)*reg3)+B3*exp(-i*k(3)*reg3);
psi4_bound=A4*exp(i*k(4)*reg4)+B4*exp(-i*k(4)*reg4);
integral1=sum((psi1_bound.*conj(psi1_bound))*dx);
integral2=sum((psi2_bound.*conj(psi2_bound))*dx);
integral3=sum((psi3_bound.*conj(psi3_bound))*dx);
integral4=sum((psi4_bound.*conj(psi4_bound))*dx);
total_integral=integral1+integral2+integral3+integral4;
b1=(sqrt(total_integral));
Psi1_bound=1/b1*psi1_bound;
Psi2_bound=1/b1*psi2_bound;
Psi3_bound=1/b1*psi3_bound;
Psi4_bound=1/b1*psi4_bound;
Integral1=sum((Psi1_bound.*conj(Psi1_bound))*dx);
Integral2=sum((Psi2_bound.*conj(Psi2_bound))*dx);
Integral3=sum((Psi3_bound.*conj(Psi3_bound))*dx);
Integral4=sum((Psi4_bound.*conj(Psi4_bound))*dx);
Total_integral=Integral1+Integral2+Integral3+Integral4;

% *****NPS*****
% **Simulation Of Performance Of Infrared Photodetectors*****
% integration_cont
% LT Psarakis Eftychios Hellenic Navy
dx = 10^-11;
reg1= -300e-10:dx:0;
reg2 = 0:dx:L(1,2);
reg3 = L(1,2):dx:L(1,3);
reg4 = L(1,3):dx:(L(1,3)+300e-10);
A1_c(ac)=1/sqrt(2*pi);
B1_c(ac)=-A1_c(ac)*M321_c(2,1)/M321_c(2,2);
A2_c(ac)=M_c(1,1)*A1_c(ac)+M_c(2,1)*B1_c(ac);
B2_c(ac)=M_c(3,1)*A1_c(ac)+M_c(4,1)*B1_c(ac);
A3_c(ac)=M21_c(1,1)*A1_c(ac)+M21_c(1,2)*B1_c(ac);
B3_c(ac)=M21_c(2,1)*A1_c(ac)+M21_c(2,2)*B1_c(ac);
A4_c(ac)=M321_c(1,1)*A1_c(ac)+M321_c(1,2)*B1_c(ac);
B4_c(ac)=0;
psi1_cont(ac,:)=A1_c(ac)*exp(i*k(1)*reg1)+B1_c(ac)*exp(-i*k(1)*reg1);
psi2_cont(ac,:)=A2_c(ac)*exp(i*k(2)*reg2)+B2_c(ac)*exp(-i*k(2)*reg2);
psi3_cont(ac,:)=A3_c(ac)*exp(i*k(3)*reg3)+B3_c(ac)*exp(-i*k(3)*reg3);
psi4_cont(ac,:)=A4_c(ac)*exp(i*k(4)*reg4)+B4_c(ac)*exp(-i*k(4)*reg4);

```

```

% *****NPS*****
% **Simulation Of Performance Of Infrared Photodetectors*****
% ZETA1
%LT Psarakis Eftychios Hellenic Navy
dx = 10^-11;
reg1= -300e-10:dx:0;
reg2 = 0:dx:L(1,2);
reg3 = L(1,2):dx:L(1,3);
reg4 = L(1,3):dx:(L(1,3)+300e-10);
dim=max(reg4)-min(reg1);
for kk=1:ac-1
Zita1(kk,:)=conj(Psi1_bound(1,:)).*reg1.*psi1_cont(kk,:).*dx;
Zita2(kk,:)=conj(Psi2_bound(1,:)).*reg2.*psi2_cont(kk,:).*dx;
Zita3(kk,:)=conj(Psi3_bound(1,:)).*reg3.*psi3_cont(kk,:).*dx;
Zita4(kk,:)=conj(Psi4_bound(1,:)).*reg4.*psi4_cont(kk,:).*dx;
OSC_integral1(kk,:)= sum(Zita1(kk,:));
OSC_integral2(kk,:)= sum(Zita2(kk,:));
OSC_integral3(kk,:)= sum(Zita3(kk,:));
OSC_integral4(kk,:)= sum(Zita4(kk,:));
OSC_finali(kk,:)=(OSC_integral1(kk,:)+OSC_integral2(kk,:)+OSC_integral3(kk,:)+OSC_integral4(kk,:));
Zeta_final(kk,:)=(OSC_finali(kk,:)).*conj(OSC_finali(kk,:));
%DOS(kk)=dim./(hbar*pi)*sqrt(m_eff(1)/(2*q*(Eout_cont(kk)-Eout_cont(1)+0.001)));
DOS(kk)=1/(hbar*pi)*sqrt(m_eff(1)/(2*q*(Eout_cont(kk)-V(1)+0.0001)));
end

```

```

% *****NPS*****
% **Simulation Of Performance Of Infrared Photodetectors*****
% EwellsmallBiasAiry
%LT Psarakis Eftychios Hellenic Navy
if F>0
for tt=1:4
if width(tt)==inf
Z_dir(tt)=0;
else
Z_dir(tt) = L(tt);
end
end
Z_dir
else
for tt=1:4
if width(tt)==inf
Z_dir(tt)=0;
else

```

```

Z_dir(1) = L(3);
Z_dir(2) = L(2);
end
end
x=[x(4),x(3),x(2),x(1)];
end

eg(1) = 1.519 + 1.247.*x(1);
eg(2) = 1.519 - 1.102.*x(2);
eg(3) = 1.519 - 1.102.*x(3);
eg(4) = 1.519 + 1.247.*x(4);
eg=[eg(1) eg(2) eg(3) eg(4)];
for tt=1:ii
if F>0
V(tt) = 0.62*(eg(tt) - eg(2));
else
V(tt) = 0.62*(eg(tt) - eg(3));
end
m_eff(tt) = 1/((x(tt)/(0.028*m0)) + ((1-x(tt))/(0.067*m0)));
C(tt) = (((2*m_eff(tt)*q)/((F*hbar)^2))^(1/3));
end
for tt=1:ii-1
sigma(tt) = ((m_eff(tt)*C(tt+1))/(m_eff(tt+1)*C(tt)));
end
if F < 0;
DD = 0;
V2_ = V(1);
else
DD = -F*L(2);
V2_ = V(1)- F*L(3);
end
ac =1;
n = 0;
ll=1;
%by varing dE we can ajust the number of states found
E_c =min(V(1),V(4))-03;
Vb=input('give Vb in eV :');
disp('The continuus states energy are:')
dE_c = (Vb-E_c)/1001;
while E_c < Vb
E_c = E_c + dE_c;
for tt=1:4
eta(tt) = (E_c - V(tt));
end
for jj=1:4
Alpha(jj) = -C(jj)*(F*Z_dir(jj) + eta(jj));

```

```

Alphaout(ll,jj)=[Alpha(:,jj)];
end
for jj=1:3
alpha(jj+1)= -C(jj+1)*(F*Z_dir(jj) + eta(jj+1));
alphaout(ll,jj)=[alpha(:,jj)];
end
for jj=1:3
m11_c= (pi)*(airy(0,alpha(jj+1))*airy(3,Alpha(jj)) -
sigma(jj)*(airy(2,Alpha(jj))*airy(1,alpha(jj+1)))); -
m12_c= (pi)*(airy(2,alpha(jj+1))*airy(3,Alpha(jj)) -
sigma(jj)*(airy(2,Alpha(jj))*airy(3,alpha(jj+1)))); -
m21_c= (pi)*(sigma(jj)*(airy(0,Alpha(jj))*airy(1,alpha(jj+1))) -
airy(1,Alpha(jj))*airy(0,alpha(jj+1))); -
m22_c= (pi)*(sigma(jj)*(airy(0,Alpha(jj))*airy(3,alpha(jj+1))) -
airy(1,Alpha(jj))*airy(2,alpha(jj+1))); -
%checking the output data
m11out_c(ll,jj)=[m11_c];
m12out_c(ll,jj)=[m12_c];
m21out_c(ll,jj)=[m21_c];
m22out_c(ll,jj)=[m22_c];
M_c(:,jj)=[m11_c;m12_c;m21_c;m22_c];
end
%finding Mn
M12_c=[M_c(1,1),M_c(2,1);M_c(3,1),M_c(4,1)],[M_c(1,2),M_c(2,2);M_c(3,2),
M_c(4,2)];
M23_c=[M_c(1,2),M_c(2,2);M_c(3,2),M_c(4,2)],[M_c(1,3),M_c(2,3);M_c(3,3),
M_c(4,3)];
M123_c=[M_c(1,1),M_c(2,1);M_c(3,1),M_c(4,1)],[M_c(1,2),M_c(2,2);M_c(3,2),
M_c(4,2)][M_c(1,3),M_c(2,3);M_c(3,3),M_c(4,3)];
disp(E_c)
Eout_cont(ac) = E_c;
Epsi_cont;
hold on
r = 0:1:width(2)+width(3);
plot(r,Eout_cont(ac),'r')
text(0,Eout_cont(ac)+.01,['E_',num2str(ac+2),' =
',sprintf('%4.3f',Eout_cont(ac)), ' eV'])
plot((X*1e10),(real(psi1_cont(ac,:)/5e5)+Eout_cont(ac)), 'k')
plot((Y*1e10),(real(psi2_cont(ac,:)/5e5)+Eout_cont(ac)), 'k')
plot((Z*1e10),(real(psi3_cont(ac,:)/5e5)+Eout_cont(ac)), 'k')
plot((T*1e10),(real(psi4_cont(ac,:)/5e5)+Eout_cont(ac)), 'k')
ac=ac+1;
ll=ll+1;
end
text(-40,1.15*V(1),['V(1) = ',sprintf('%4.3f',V(1)), ' eV'])

```

```

xlabel('X (Angstroms)')
ylabel('Potential Height (eV)')
title('Quantum Well')
% %*****Ewell2*****
% %*****BOUND STATES*****
hold on
x1 = -100:.1:0;
h1 = 0:.001:V(1);
plot(x1,(V(1)-F*(x1*1e-10)),'LineWidth',3)
x2 = 0:.1:width(2);
x3 = width(2):.1:(width(2)+width(3));
if F > 0
h2 = (-F*L(2)):001:(V(3)-(F*L(2)));
h3 = (V(3)-(F*L(3))):001:(V(1)-(F*L(3)));
plot(x3,((V(3)-F*(x3*1e-10))),'LineWidth',3)
end
if F < 0
h2 = (-F*L(2)):001:(V(2)-F*L(2));
h3 = (V(2)-F*L(3)):001:(V(1)-F*L(3));
plot(x3,((V(2)-F*(x3*1e-10))),'LineWidth',3)
end
x4 = (width(2)+width(3)):1:(width(2)+width(3)+100);
plot(x4,((V(1)-F*(x4*1e-10))),'LineWidth',3)
plot(x2,(-F*(x2*1e-10)),'LineWidth',3)
plot(0,h1,'LineWidth',1)
plot(width(2),h2,'LineWidth',1)
plot((width(2)+width(3)),h3,'LineWidth',1)
% *****
% *****BOUND STATES*****
% *****
% clear M22 M22out n ll dE E m11 m12 m21 m22 alpha alphaout
% clear m11out m12out m21out m22out M12 M23 M123 Alpha Alphaout
ab =1;
n = 0;
ll=1;
dE = 5*10^-4;
E = DD;
%Evaluate the energy from the bottom to the top of the well;
while E < V2_-dE

if E > V2_-10^-3
dE = 10^-6;
end
E = E + dE;
for tt=1:4
eta(tt) = (E - V(tt));

```

```

end
for jj=1:4
Alpha(jj) = -C(jj)*(F*Z_dir(jj) + eta(jj));
Alphaout(ll,jj)=[Alpha(:,jj)];
end
for jj=1:3
alpha(jj+1)= -C(jj+1)*(F*Z_dir(jj) + eta(jj+1));
alphaout(ll,jj)=[alpha(:,jj)];
end
for jj=1:3
m11=(pi)*(asymptoticAiry(0,alpha(jj+1))*asymptoticAiry(3,Alpha(jj))
sigma(jj)*(asymptoticAiry(2,Alpha(jj))*asymptoticAiry(1,alpha(jj+1))));
m12=(pi)*(asymptoticAiry(2,alpha(jj+1))*asymptoticAiry(3,Alpha(jj))
sigma(jj)*(asymptoticAiry(2,Alpha(jj))*asymptoticAiry(3,alpha(jj+1))));
m21=
(pi)*(sigma(jj)*(asymptoticAiry(0,Alpha(jj))*asymptoticAiry(1,alpha(jj+1))) - asymptoticAiry(1,Alpha(jj))*asymptoticAiry(0,alpha(jj+1)));
m22=
(pi)*(sigma(jj)*(asymptoticAiry(0,Alpha(jj))*asymptoticAiry(3,alpha(jj+1))) - asymptoticAiry(1,Alpha(jj))*asymptoticAiry(2,alpha(jj+1)));
%checking the output data
m11out(ll,jj)=[m11];
m12out(ll,jj)=[m12];
m21out(ll,jj)=[m21];
m22out(ll,jj)=[m22];
M(:,jj)=10^-40*[m11;m12;m21;m22];
end
%finding Mn
M12=[M(1,1),M(2,1);M(3,1),M(4,1)]*[M(1,2),M(2,2);M(3,2),M(4,2)]; %10^60
M23=[M(1,2),M(2,2);M(3,2),M(4,2)]*[M(1,3),M(2,3);M(3,3),M(4,3)]; %10^60
M123=[M(1,1),M(2,1);M(3,1),M(4,1)]*[M(1,2),M(2,2);M(3,2),M(4,2)]*[M(1,3),
M(2,3);M(3,3),M(4,3)]; %10^90
M22 = real(M123(2,2));
%checking the output data
M22out(ll)=[M22];
EM22(ll)=[E];
%%%%%end of check%%%%%
ll=ll+1;
z = y;
y = M22;
if z*y < 0      %Determine the approximate eigen energy first
    n = n +1;
    if n < 2      %Increase the acuaracy of eigen energy
        E = E-dE;
        dE = 1e-6;
        y = z;
    end
end

```

```

    end
end
if n > 1
    disp('The ground state energy is:')
    disp(E)
%    disp(M123)
%    disp(M23)
Eout(ab) = E; % Stores energy levels into an array
Epsi_bound1;
dE = 5e-4;
n = 0;
hold on
r = 0:1:width(2)+(ab-1)*width(3);
if ab < 3
    plot(r,Eout(ab),'r')
    text(0,Eout(ab)+.01,['E_',num2str(ab),' = ',sprintf('%4.3f',Eout(ab)), ' eV'])
    plot((X*1e10),(real(Psi1_bound(ab,:)/5e5)+E),'k')
    plot((Y*1e10),(real(Psi2_bound(ab,:)/5e5)+E),'k')
    plot((Z*1e10),(real(Psi3_bound(ab,:)/5e5)+E),'k')
    plot((T*1e10),(real(Psi4_bound(ab,:)/5e5)+E),'k')
end
ab = ab+1;
end
end
ZETA;
% ****
% *****oscillator strength*****
% ****
for ai=1:ac-1;
    DE(ai)=(Eout_cont(ai)-Eout);
    f_oscil(ai)=2*(m_eff(1))/(hbar^2).*DE(ai)*q.*Zeta_final(ai)';
end
figure(2)
plot(DE,real(f_oscil))

xlabel('DeltaE')
ylabel('oscillator strength f')
title('oscillator strength Vs \DeltaE')
for ai=1:ac-1;
Prod_f_oscil_DOS(ai)=f_oscil(ai).*DOS(ai)*q;
OSCSTR(ai)=f_oscil(ai).*DOS(ai)*q*dE_c;
OSCSTR_INTEG=sum(OSCSTR);
end
figure(3)
plot(DE,real(Prod_f_oscil_DOS))

```

```

xlabel('DeltaE')
ylabel('oscillator strength)*(density of states)')
title('oscillator strength multiplied by density of states Vs |DeltaE')

disp('The (oscillator strength)*(density of states) integral is')
round(OSCSTR_INTEG)

% *****NPS*****
% **Simulation Of Performance Of Infrared Photodetectors*****
% Epsi_bound1
% LT Psarakis Eftychios Hellenic Navy
warning off
deltax = 10^-11;
B4 = 1;
A4 = 0;
A3(ab) = 10^40*M(2,3)*B4;
B3(ab) = 10^40*M(4,3)*B4;
A2(ab) = 10^80*M23(1,2);
B2(ab) = 10^80*M23(2,2)*B4;
% if ab==1
%   A1(1)=0;
% else
%   A1(ab) =10^20*M123(1,2);
% end
B1 = 0;

if F > 0
    X = -300e-10:deltax:0;
    Y = 0:deltax:L(1,2);
    Z = L(1,2):deltax:L(1,3);
    T = L(1,3):deltax:(L(1,3)+300e-10);
else
    X = L(1,3):deltax:(L(1,3)+300e-10);
    Y = L(1,2):deltax:L(1,3);
    Z = 0:deltax:L(1,2);
    T = -300e-10:deltax:0;
end
P1_bound(ab,:) = -C(1).*(F.*X + eta(1));
P2_bound(ab,:) = -C(2).*(F.*Y + eta(2));
P3_bound(ab,:) = -C(3).*(F.*Z + eta(3));
P4_bound(ab,:) = -C(4).*(F.*T + eta(4));

psi1_bound(ab,:) = (A1(:,ab).*asymptoticAiry(0,P1_bound(ab,:))) +
B1.*asymptoticAiry(2,P1_bound(ab,:)));

```

```

psi2_bound(ab,:) = (A2(:,ab).*asymptoticAiry(0,P2_bound(ab,:))) +
B2(:,ab).*asymptoticAiry(2,P2_bound(ab,:)));
psi3_bound(ab,:) = (A3(:,ab).*asymptoticAiry(0,P3_bound(ab,:))) +
B3(:,ab).*asymptoticAiry(2,P3_bound(ab,:)));
psi4_bound(ab,:) = (A4.*asymptoticAiry(0,P4_bound(ab,:))) +
B4.*asymptoticAiry(2,P4_bound(ab,:)));
psi1_bound(ab,:) = 10^0*psi1_bound(ab,:);
psi2_bound(ab,:) = 10^-100*psi2_bound(ab,:);
psi3_bound(ab,:) = 10^-100*psi3_bound(ab,:);
psi4_bound(ab,:) = 10^-100*psi4_bound(ab,:);
integrand1_bound(ab,:) = (psi1_bound(ab,:).*conj(psi1_bound(ab,:)))*deltax;
integrand2_bound(ab,:) = (psi2_bound(ab,:).*conj(psi2_bound(ab,:)))*deltax;
integrand3_bound(ab,:) = (psi3_bound(ab,:).*conj(psi3_bound(ab,:)))*deltax;
integrand4_bound(ab,:) = (psi4_bound(ab,:).*conj(psi4_bound(ab,:)))*deltax;
integral1_bound(ab,:) = sum(integrand1_bound(ab,:));
integral2_bound(ab,:) = sum(integrand2_bound(ab,:));
integral3_bound(ab,:) = sum(integrand3_bound(ab,:));
integral4_bound(ab,:) = sum(integrand4_bound(ab,:));
finali_bound(ab,:) = integral1_bound(ab,:) + integral2_bound(ab,:) + integral3_bound(ab,:) + integral4_bound(ab,:);
b3_bound(ab,:)=1./sqrt(finali_bound(ab,:));
Psi1_bound(ab,:) = b3_bound(ab,:).*psi1_bound(ab,:);
Psi2_bound(ab,:) = b3_bound(ab,:).*psi2_bound(ab,:);
Psi3_bound(ab,:) = b3_bound(ab,:).*psi3_bound(ab,:);
Psi4_bound(ab,:) = b3_bound(ab,:).*psi4_bound(ab,:);
Integral1_bound(ab,:)=sum((Psi1_bound(ab,:).*conj(Psi1_bound(ab,:)))*deltax);
Integral2_bound(ab,:)=sum((Psi2_bound(ab,:).*conj(Psi2_bound(ab,:)))*deltax);
Integral3_bound(ab,:)=sum((Psi3_bound(ab,:).*conj(Psi3_bound(ab,:)))*deltax);
Integral4_bound(ab,:)=sum((Psi4_bound(ab,:).*conj(Psi4_bound(ab,:)))*deltax);
Ttal_integral_bound(ab,:)=Integral1_bound(ab,:)+Integral2_bound(ab,:)+Integral3_bound(ab,:)+Integral4_bound(ab,:)

```

```

% ****NPS*****
% **Simulation Of Performance Of Infrared Photodetectors*****
%Epsi\_cont1
%LT Psarakis Eftychios Hellenic Navy
deltax = 10^-11;
if F>0
    X = -300e-10:deltax:0;
    Y = 0:deltax:L(1,2);
    Z = L(1,2):deltax:L(1,3);
    T = L(1,3):deltax:(L(1,3)+300e-10);
    A4(ac) = 1/sqrt(2*pi);
    B4(ac) = -(M123_c(2,1)/M123_c(2,2))*A4(ac) ;
    A3(ac) = (M_c(1,3)*A4(ac) + B4(ac)*M_c(2,3));

```

```

B3(ac) = (M_c(3,3)*A4(ac) + B4(ac)*M_c(4,3));
A2(ac) = (M23_c(1,1)*A4(ac)+B4(ac)*M23_c(1,2));
B2(ac) = (M23_c(2,1)*A4(ac)+B4(ac)*M23_c(2,2));
A1(ac) = (M123_c(1,1)*A4(ac) + B4(ac)*M123_c(1,2));
B1(ac) = 0;
else
    X = L(1,3):deltax:(L(1,3)+300e-10);
    Y = L(1,2):deltax:L(1,3);
    Z = 0:deltax:L(1,2);
    T = -300e-10:deltax:0;
    A4(ac) = 1/sqrt(2*pi);
    B4(ac) = -(M123_c(2,1)/M123_c(2,2))*A4(ac) ;
    A3(ac) = (M_c(1,3)*A4(ac) + B4(ac)*M_c(2,3));
    B3(ac) = (M_c(3,3)*A4(ac) + B4(ac)*M_c(4,3));
    A2(ac) = (M23_c(1,1)*A4(ac)+B4(ac)*M23_c(1,2));
    B2(ac) = (M23_c(2,1)*A4(ac)+B4(ac)*M23_c(2,2));
    A1(ac) = (M123_c(1,1)*A4(ac) + B4(ac)*M123_c(1,2));
    B1(ac) = 0;
end
P1_cont(ac,:) = -C(1).*(F.*X + eta(1));
P2_cont(ac,:) = -C(2).*(F.*Y + eta(2));
P3_cont(ac,:) = -C(3).*(F.*Z + eta(3));
P4_cont(ac,:) = -C(4).*(F.*T + eta(4));
psi1_cont(ac,:) = A1(ac)*asymptoticAiry(0,P1_cont(ac,:)) +
B1(ac)*asymptoticAiry(2,P1_cont(ac,:));
psi2_cont(ac,:) = A2(ac)*asymptoticAiry(0,P2_cont(ac,:)) +
B2(ac)*asymptoticAiry(2,P2_cont(ac,:));
psi3_cont(ac,:) = A3(ac)*asymptoticAiry(0,P3_cont(ac,:)) +
B3(ac)*asymptoticAiry(2,P3_cont(ac,:));
psi4_cont(ac,:) = A4(ac)*asymptoticAiry(0,P4_cont(ac,:)) +
B4(ac)*asymptoticAiry(2,P4_cont(ac,:));
integrand1_cont(ac,:) = (psi1_cont(ac,:).*conj(psi1_cont(ac,:)))*deltax;
integrand2_cont(ac,:) = (psi2_cont(ac,:).*conj(psi2_cont(ac,:)))*deltax;
integrand3_cont(ac,:) = (psi3_cont(ac,:).*conj(psi3_cont(ac,:)))*deltax;
integrand4_cont(ac,:) = (psi4_cont(ac,:).*conj(psi4_cont(ac,:)))*deltax;
integral1_cont(ac,:) = sum(integrand1_cont(ac,:));
integral2_cont(ac,:) = sum(integrand2_cont(ac,:));
integral3_cont(ac,:) = sum(integrand3_cont(ac,:));
integral4_cont(ac,:) = sum(integrand4_cont(ac,:));
finali_cont(ac,:) = integral1_cont(ac,:) + integral2_cont(ac,:) + integral3_cont(ac,:) + integral4_cont(ac,:);
b3_cont(ac,:) = 1/(sqrt(finali_cont(ac,:)));
Psi1_cont(ac,:) = b3_cont(ac,:)*psi1_cont(ac,:);
Psi2_cont(ac,:) = b3_cont(ac,:)*psi2_cont(ac,:);
Psi3_cont(ac,:) = b3_cont(ac,:)*psi3_cont(ac,:);
Psi4_cont(ac,:) = b3_cont(ac,:)*psi4_cont(ac,:);

```

```

Integral1_cont(ac,:)=sum((Psi1_cont(ac,:).*conj(Psi1_cont(ac,:)))*deltax);
Integral2_cont(ac,:)=sum((Psi2_cont(ac,:).*conj(Psi2_cont(ac,:)))*deltax);
Integral3_cont(ac,:)=sum((Psi3_cont(ac,:).*conj(Psi3_cont(ac,:)))*deltax);
Integral4_cont(ac,:)=sum((Psi4_cont(ac,:).*conj(Psi4_cont(ac,:)))*deltax);
To-
tal_integral_cont(ac,:)=Integral1_cont(ac,:)+Integral2_cont(ac,:)+Integral3_cont(ac,:)+Int
egral4_cont(ac,:);

```

```

% ****NPS*****
% **Simulation Of Performance Of Infrared Photodetectors*****
%Epsi_bound
%LT Psarakis Eftychios Hellenic Navy
deltax = 10^-11;
A4_b = 0;
B4_b = 1;
A3_b(a) = M(1,3)*A4_b + M(2,3)*B4_b;
B3_b(a) = M(3,3)*A4_b + M(4,3)*B4_b;
A2_b(a) = M23(1,2)*B4_b;
B2_b(a) = M23(2,1)*A4_b + M23(2,2)*B4_b;
A1_b(a) = M123(1,2)*B4_b;
B1_b = 0;
if F > 0
    X = -300e-10:deltax:0;
    Y = 0:deltax:L(1,2);
    Z = L(1,2):deltax:L(1,3);
    T = L(1,3):deltax:(L(1,3)+300e-10);
else
    X = L(1,3):deltax:(L(1,3)+300e-10);
    Y = L(1,2):deltax:L(1,3);
    Z = 0:deltax:L(1,2);
    T = -300e-10:deltax:0;
end
P1_bound(a,:)= -C(1).*(F.*X + eta(1));
P2_bound(a,:)= -C(2).*(F.*Y + eta(2));
P3_bound(a,:)= -C(3).*(F.*Z + eta(3));
P4_bound(a,:)= -C(4).*(F.*T + eta(4));

```

$$\begin{aligned}
\text{psi1_bound}(a,:) &= A1_b(:,a) \cdot \text{airy}(0, P1_bound(a,:)) &+ \\
B1_b \cdot \text{airy}(2, P1_bound(a,:)); & \\
\text{psi2_bound}(a,:) &= A2_b(:,a) \cdot \text{airy}(0, P2_bound(a,:)) &+ \\
B2_b(:,a) \cdot \text{airy}(2, P2_bound(a,:)); & \\
\text{psi3_bound}(a,:) &= A3_b(:,a) \cdot \text{airy}(0, P3_bound(a,:)) &+ \\
B3_b(:,a) \cdot \text{airy}(2, P3_bound(a,:));
\end{aligned}$$

```

psi4_bound(a,:) = A4_b.*airy(0,P4_bound(a,:)) + B4_b.*airy(2,P4_bound(a,:));

psi_1_bound(a,:) = conj(psi1_bound(a,:));
psi_2_bound(a,:) = conj(psi2_bound(a,:));
psi_3_bound(a,:) = conj(psi3_bound(a,:));
psi_4_bound(a,:) = conj(psi4_bound(a,:));

integrand1_bound(a,:) = (psi1_bound(a,:).*psi1_bound(a,:))*deltax;
integrand2_bound(a,:) = (psi2_bound(a,:).*psi2_bound(a,:))*deltax;
integrand3_bound(a,:) = (psi3_bound(a,:).*psi3_bound(a,:))*deltax;
integrand4_bound(a,:) = (psi4_bound(a,:).*psi4_bound(a,:))*deltax;

integral1_bound(a,:) = sum(integrand1_bound(a,:));
integral2_bound(a,:) = sum(integrand2_bound(a,:));
integral3_bound(a,:) = sum(integrand3_bound(a,:));
integral4_bound(a,:) = sum(integrand4_bound(a,:));

finali_bound(a,:) = integral1_bound(a,:) + integral2_bound(a,:) + integral3_bound(a,:) + integral4_bound(a,:);

b3_bound(a,:) = 1/(sqrt(finali_bound(a,:)));

Psi1_bound(a,:) = b3_bound(a,:)*psi1_bound(a,:);
Psi2_bound(a,:) = b3_bound(a,:)*psi2_bound(a,:);
Psi3_bound(a,:) = b3_bound(a,:)*psi3_bound(a,:);
Psi4_bound(a,:) = b3_bound(a,:)*psi4_bound(a,:);

% *****NPS*****
% **Simulation Of Performance Of Infrared Photodetectors*****
% Epsi\_cont
% LT Psarakis Eftychios Hellenic Navy
deltax = 10^-11;

if F>0
    X = -300e-10:deltax:0;
    Y = 0:deltax:L(1,2);
    Z = L(1,2):deltax:L(1,3);
    T = L(1,3):deltax:(L(1,3)+300e-10);

    A4(ac) = 1/sqrt(2*pi);
    B4(ac) = -(M123_c(2,1)/M123_c(2,2))*A4(ac) ;
    A3(ac) = (M_c(1,3)*A4(ac) + B4(ac)*M_c(2,3));
    B3(ac) = (M_c(3,3)*A4(ac) + B4(ac)*M_c(4,3));
    A2(ac) = (M23_c(1,1)*A4(ac)+B4(ac)*M23_c(1,2));

```

```

B2(ac) = (M23_c(2,1)*A4(ac)+B4(ac)*M23_c(2,2));
A1(ac) = (M123_c(1,1)*A4(ac) + B4(ac)*M123_c(1,2));
B1(ac) = 0;
else
    X = L(1,3):deltax:(L(1,3)+300e-10);
    Y = L(1,2):deltax:L(1,3);
    Z = 0:deltax:L(1,2);
    T = -300e-10:deltax:0;

    A4(ac) = 1/sqrt(2*pi);
    B4(ac) = -(M123_c(2,1)/M123_c(2,2))*A4(ac) ;
    A3(ac) = (M_c(1,3)*A4(ac) + B4(ac)*M_c(2,3));
    B3(ac) = (M_c(3,3)*A4(ac) + B4(ac)*M_c(4,3));
    A2(ac) = (M23_c(1,1)*A4(ac)+B4(ac)*M23_c(1,2));
    B2(ac) = (M23_c(2,1)*A4(ac)+B4(ac)*M23_c(2,2));
    A1(ac) = (M123_c(1,1)*A4(ac) + B4(ac)*M123_c(1,2));
    B1(ac) = 0;
end

P1_cont(ac,:) = -C(1).*(F.*X + eta(1));
P2_cont(ac,:) = -C(2).*(F.*Y + eta(2));
P3_cont(ac,:) = -C(3).*(F.*Z + eta(3));
P4_cont(ac,:) = -C(4).*(F.*T + eta(4));

psi1_cont(ac,:) = A1(ac)*airy(0,P1_cont(ac,:)) + B1(ac)*airy(2,P1_cont(ac,:));
psi2_cont(ac,:) = A2(ac)*airy(0,P2_cont(ac,:)) + B2(ac)*airy(2,P2_cont(ac,:));
psi3_cont(ac,:) = A3(ac)*airy(0,P3_cont(ac,:)) + B3(ac)*airy(2,P3_cont(ac,:));
psi4_cont(ac,:) = A4(ac)*airy(0,P4_cont(ac,:)) + B4(ac)*airy(2,P4_cont(ac,:));

psi_1_cont(ac,:) = conj(psi1_cont(ac,:));
psi_2_cont(ac,:) = conj(psi2_cont(ac,:));
psi_3_cont(ac,:) = conj(psi3_cont(ac,:));
psi_4_cont(ac,:) = conj(psi4_cont(ac,:));

integrand1_cont(ac,:) = (psi1_cont(ac,:).*psi_1_cont(ac,:))*deltax;
integrand2_cont(ac,:) = (psi2_cont(ac,:).*psi_2_cont(ac,:))*deltax;
integrand3_cont(ac,:) = (psi3_cont(ac,:).*psi_3_cont(ac,:))*deltax;
integrand4_cont(ac,:) = (psi4_cont(ac,:).*psi_4_cont(ac,:))*deltax;

integral1_cont(ac,:) = sum(integrand1_cont(ac,:));
integral2_cont(ac,:) = sum(integrand2_cont(ac,:));
integral3_cont(ac,:) = sum(integrand3_cont(ac,:));
integral4_cont(ac,:) = sum(integrand4_cont(ac,:));

```

```

finali_cont(ac,:) = integral1_cont(ac,:)+integral2_cont(ac,:)+integral3_cont(ac,:)+integral4_cont(ac,:);

b3_cont(ac,:)=1/(sqrt(finali_cont(ac,:)));
Psi1_cont(ac,:)=b3_cont(ac,:)*psi1_cont(ac,:);
Psi2_cont(ac,:)=b3_cont(ac,:)*psi2_cont(ac,:);
Psi3_cont(ac,:)=b3_cont(ac,:)*psi3_cont(ac,:);
Psi4_cont(ac,:)=b3_cont(ac,:)*psi4_cont(ac,:);

psi1_cont_der(ac,:)=A1(ac)*airy(1,P1_cont(ac,:))
+B1(ac)*airy(3,P1_cont(ac,:));
psi2_cont_der(ac,:)=A2(ac)*airy(1,P2_cont(ac,:))+
B2(ac)*airy(3,P2_cont(ac,:));
psi3_cont_der(ac,:)=A3(ac)*airy(1,P3_cont(ac,:))+
B3(ac)*airy(3,P3_cont(ac,:));
psi4_cont_der(ac,:)=A4(ac)*airy(1,P4_cont(ac,:))+
B4(ac)*airy(3,P4_cont(ac,:));
Psi1_cont_der(ac,:)=b3_cont(ac,:)*psi1_cont_der(ac,:);
Psi2_cont_der(ac,:)=b3_cont(ac,:)*psi2_cont_der(ac,:);
Psi3_cont_der(ac,:)=b3_cont(ac,:)*psi3_cont_der(ac,:);
Psi4_cont_der(ac,:)=b3_cont(ac,:)*psi4_cont_der(ac,:);
Integral1_cont(ac,:)=sum((Psi1_cont(ac,:).*conj(Psi1_cont(ac,:)))*deltax);
Integral2_cont(ac,:)=sum((Psi2_cont(ac,:).*conj(Psi2_cont(ac,:)))*deltax);
Integral3_cont(ac,:)=sum((Psi3_cont(ac,:).*conj(Psi3_cont(ac,:)))*deltax);
Integral4_cont(ac,:)=sum((Psi4_cont(ac,:).*conj(Psi4_cont(ac,:)))*deltax);

```

To-
tal_integral_cont(ac,:)=Integral1_cont(ac,:)+Integral2_cont(ac,:)+Integral3_cont(ac,:)+Integral4_cont(ac,:);

```

% ****NPS*****
% **Simulation Of Performance Of Infrared Photodetectors*****
% LT Psarakis Eftychios Hellenic Navy
function y=aproxAiry(x)
% this function approximates the airy's functions and their
% dirivatives
% Author: © E.Psarakis, § 31-Aug-2004
% Ai(x)-->ans(1,1) --> ai
% Bi(x)-->ans(1,2) --> bi
% Ai'(x)-->ans(1,3)--> ad
% Bi'(x)-->ans(1,4)--> bd
% ai=[];bi=[];ad=[];bd=[];
% ai=(4*pi)^(-1/2)*(x.^(-1/4).*exp(-2/3*(x).^(3/2)));
% bi=(pi)^(-1/2)*(x).^(-1/4).*exp(2/3*(x).^(3/2));
% ad=-(4*pi)^(-1/2)*(x).^(1/4).*exp(-2/3*(x).^(3/2));

```

```

% bd=(pi)^(-1/2)*(x).^(1/4).*exp(2/3*(x).^(3/2));
% [ai; bi ;ad ;bd];
% y=eval(['ai;bi;ad;bd']);
index=0;
ai=[];bi=[];ad=[];bd=[];
for index=1:length(x);
    if x(index)>=0
        ai(index)=(4*pi)^(-1/2)*(x(index)).^(-1/4).*exp(-2/3*(x(index)).^1.5);
        bi(index)=(pi)^(-1/2)*(x(index)).^(-1/4).*exp(2/3*(abs(x(index))).^1.5);
        ad(index)=-(4*pi)^(-1/2)*(x(index)).^(1/4).*exp(-2/3*(x(index)).^1.5);
        bd(index)=(pi)^(-1/2)*(x(index)).^(1/4).*exp(2/3*(x(index)).^1.5);
    else
        ai(index)=(pi)^(-1/2)*(-(x(index))).^(-1/4).*sin(2/3*(-(x(index))).^1.5+pi/4);
        bi(index)=(pi)^(-1/2)*(-(x(index))).^(-1/4).*cos(2/3*(-(x(index))).^1.5+pi/4);
        ad(index)=-(pi)^(-1/2)*(-(x(index))).^(1/4).*(cos(2/3*(-(x(index))).^1.5+pi/4));
        % -1/(4*sqrt(pi)).*(abs(x(index))).^(-5/4).*sin(2/3*(abs(x(index))).^1.5+pi/4);
        bd(index)=(pi)^(-1/2)*(-(x(index))).^(1/4).*(sin(2/3*(-(x(index))).^1.5+pi/4));
        % -1/(4*sqrt(pi)).*(abs(x(index))).^(-5/4).*cos(2/3*(abs(x(index))).^1.5+pi/4);
    end
    end
    [ai; bi;ad ;bd];
    y=eval(['ai; bi;ad ;bd']);
    % ai=[];bi=[];ad=[];bd=[];

```

% *****NPS*****

% **Simulation Of Performance Of Infrared Photodetectors*****

% LT Psarakis Eftychios Hellenic Navy

function t=asymptoticAiry(n,x)

% this function approximates the airy's functions and their

% dirivatives. it is used like the matlab airy(x)

% Author: © E.Psarakis, § 31-Aug-2004

% Ai(x)-->ans(1,1)

% Bi(x)-->ans(1,2)

% Ai'(x)-->ans(1,3)

% Bi'(x)-->ans(1,4)

if n==0

approxAiry(x);

t=ans(1,:);

end

if n==1

approxAiry(x);

t=ans(3,:);

end

if n==2

approxAiry(x);

```

t=ans(2,:);
end
if n==3
    aproxAiry(x);
    t=ans(4,:);
end

% *****NPS*****
% **Simulation Of Performance Of Infrared Photodetectors*****
% ZETA
%LT Psarakis Eftychios Hellenic Navy
warning off
deltaz = 10^-11;

if F > 0
    X = -300e-10:deltaz:0;
    Y = 0:deltaz:L(1,2);
    Z = L(1,2):deltaz:L(1,3);
    T = L(1,3):deltaz:(L(1,3)+300e-10);
    dim=max(T)-min(X);
else
    X = L(1,3):deltaz:(L(1,3)+300e-10);
    Y = L(1,2):deltaz:L(1,3);
    Z = 0:deltaz:L(1,2);
    T = -300e-10:deltaz:0;
    dim=max(X)-min(T);
end
for kk=1:ac-1
    Zita1(kk,:)=conj(Psi1_bound(1,:)).*X.*Psi1_cont(kk,:).*deltaz;
    Zita2(kk,:)=conj(Psi2_bound(1,:)).*Y.*Psi2_cont(kk,:).*deltaz;
    Zita3(kk,:)=conj(Psi3_bound(1,:)).*Z.*Psi3_cont(kk,:).*deltaz;
    Zita4(kk,:)=conj(Psi4_bound(1,:)).*T.*Psi4_cont(kk,:).*deltaz;
    OSC_integral1(kk,:)= sum(Zita1(kk,:));
    OSC_integral2(kk,:)= sum(Zita2(kk,:));
    OSC_integral3(kk,:)= sum(Zita3(kk,:));
    OSC_integral4(kk,:)= sum(Zita4(kk,:));
    OSC_finali(kk,:)=(OSC_integral1(kk,:)+OSC_integral2(kk,:)+OSC_integral3(kk,:)+OSC_integral4(kk,:));
    Zeta_final(kk,:)=(OSC_finali(kk,:)).*conj(OSC_finali(kk,:));

    %
    DOS(kk)=dim./(hbar*pi)*sqrt(m_eff(1)./(2*q*(Eout_cont(kk)-min(V(1),V(2)))));
    DOS(kk)=dim./(hbar*pi)*sqrt(m_eff(1)./(2*q*(Eout_cont(kk)-Eout_cont(1)+.001)));
end

```

APPENDIX B: EKF INITIALIZATION AND TRACKING

In the present Appendix we present the BOT initialization and tracking algorithm. The core of the algorithm is **BOT.m**. Once this program is executed, the loop **INITIALIZATION.m** is called, and the user must define the initialization bearings.

```
% ****INITIALIZATION.m*****
% *****Written by LT Eftychios Psarakis Hellenic Navy*****
% ***Thesis Project: Simulation of Performance of Infrared Photodetectors*****
% ****
% clc
% clear
S1p=[0;0]; % Sensor 1 at origin
S1p=[10000;0]; % Sensor 2 at (10000,0)
% b1=input('give mesured bearing 1 from sensor 1 in degrees: ');%33
% b2=input('give mesured bearing 1 from sensor 2 in degrees: ');%173
b1_1=b1*2*pi/360; %convert to rad
b1_2=b2*2*pi/360; %convert to rad
sigma1b=1*pi/180; % 1 deg std dev in bearing
miss=abs(randn*sigma1b);

b1_S1_plus =b1_1+miss; % bearing 1 from sensor 1 (+)
b1_S1_minus=b1_1-miss; % bearing 1 from sensor 1 (-)

b1_S2_plus =b1_2+miss; % bearing 1 from sensor 2 (+)
b1_S2_minus=b1_2-miss; % bearing 1 from sensor 2 (-)

% b_1=input('give mesured bearing 2 from sensor 1 in degrees: ');%33.46
% b_2=input('give mesured bearing 2 from sensor 2 in degrees: ');%173.18
% dt=input('give time interval between the two measurements : ');
dt=.1;
b2_1=b_1*2*pi/360; %convert to rad
b2_2=b_2*2*pi/360; %convert to rad

b2_S1_plus=b2_1+miss; % bearing 2 from sensor 1 (+)
b2_S1_minus=b2_1-miss; % bearing 2 from sensor 1 (-)

b2_S2_plus=b2_2+miss; % bearing 2 from sensor 2 (+)
b2_S2_minus=b2_2-miss; % bearing 2 from sensor 2 (-)
% ****
% Triangle 1: Bearing 1 Sensor 1(+), Bearing 1 Sensor 2(+) using sine law
theta3_1=pi-b1_S1_plus-(pi-b1_S2_plus);
```

```

D1=((sin(theta3_1)/10000)^-1)*sin(pi-b1_S2_plus); %distance from (0,0)

x1=D1*cos(b1_S1_plus);
y1=D1*sin(b1_S1_plus);

% Triangle 1: Bearing 1 Sensor 1(+), Bearing 1 Sensor 2(-) using sine law
theta3_2=pi-b1_S1_plus-(pi-b1_S2_minus);
D2=((sin(theta3_2)/10000)^-1)*sin(pi-b1_S2_minus); %distance from (0,0)
x2=D2*cos(b1_S1_plus);
y2=D2*sin(b1_S1_plus);

% Triangle 1: Bearing 1 Sensor 1(-), Bearing 1 Sensor 2(+) using sine law
theta3_3=pi-b1_S1_minus-(pi-b1_S2_plus);
D3=((sin(theta3_3)/10000)^-1)*sin(pi-b1_S2_plus); %distance from (0,0)
x3=D3*cos(b1_S1_minus);
y3=D3*sin(b1_S1_minus);

% Triangle 1: Bearing 1 Sensor 1(-), Bearing 1 Sensor 2(-) using sine law
theta3_4=pi-b1_S1_minus-(pi-b1_S2_minus);
D4=((sin(theta3_4)/10000)^-1)*sin(pi-b1_S2_minus); %distance from (0,0)
x4=D4*cos(b1_S1_minus);
y4=D4*sin(b1_S1_minus);

% disp('*****first parallelogram*****');
pos1=[x1;y1];
pos2=[x2;y2];
pos3=[x3;y3];
pos4=[x4;y4];
% disp('*****');
POS1=[(x1+x2+x3+x4)/4;
      (y1+y2+y3+y4)/4]; % middle of the rectungular shape

d=max(abs((x2-x3)/(atan((y2-y3)/(x2-x3)))),abs((x4-x1)/(atan((y4-y1)/(x4-x1)))));

xx=linspace(1,10000,100);

yy1=tan(b1_S1_plus)*xx;
yy2=tan(b1_S1_minus)*xx;

a3=y3/(x3-10000);
b3=-10000*a3;
yy3=a3*xx+b3;

```

```

a4=y4/(x4-10000);
b4=-10000*a4;
yy4=a4*xx+b4;
% figure
% plot(xx,yy1,'r')
% hold on
% plot(xx,yy2,'b')
% hold on
% plot(xx,yy3,'r')
% hold on
% plot(xx,yy4,'b')

% Triangle 2: Bearing 1 Sensor 1(+), Bearing 1 Sensor 2(+) using sine law
theta3_1_2=pi-b2_S1_plus-(pi-b2_S2_plus);
D1_2=((sin(theta3_1_2)/10000)^-1)*sin(pi-b2_S2_plus); %distance from (0,0)
x1_2=D1_2*cos(b2_S1_plus);
y1_2=D1_2*sin(b2_S1_plus);

%Triangle 2: Bearing 1 Sensor 1(+), Bearing 1 Sensor 2(-) using sine law
theta3_2_2=pi-b2_S1_plus-(pi-b2_S2_minus);
D2_2=((sin(theta3_2_2)/10000)^-1)*sin(pi-b2_S2_minus); %distance from (0,0)
x2_2=D2_2*cos(b2_S1_plus);
y2_2=D2_2*sin(b2_S1_plus);

%Triangle 2: Bearing 1 Sensor 1(-), Bearing 1 Sensor 2(+) using sine law
theta3_3_2=pi-b2_S1_minus-(pi-b2_S2_plus);
D3_2=((sin(theta3_3_2)/10000)^-1)*sin(pi-b2_S2_plus); %distance from (0,0)
x3_2=D3_2*cos(b2_S1_minus);
y3_2=D3_2*sin(b2_S1_minus);

%Triangle 2: Bearing 1 Sensor 1(-), Bearing 1 Sensor 2(-) using sine law
theta3_4_2=pi-b2_S1_minus-(pi-b2_S2_minus);
D4_2=((sin(theta3_4_2)/10000)^-1)*sin(pi-b2_S2_minus); %distance from (0,0)
x4_2=D4_2*cos(b2_S1_minus);
y4_2=D4_2*sin(b2_S1_minus);

% disp('*****second parallelogram*****');
pos1_2=[x1_2;y1_2];
pos2_2=[x2_2;y2_2];
pos3_2=[x3_2;y3_2];
pos4_2=[x4_2;y4_2];
% disp('*****');

POS2=[(x1_2+x2_2+x3_2+x4_2)/4;

```

```

(y1_2+y2_2+y3_2+y4_2)/4]; % middle of the rectangular shape
d1=max(abs((x2_2-x3_2)/(atan((y2_2-y3_2)/(x2_2-x3_2)))),abs((x4_2-
x1_2)/(atan((y4_2-y1_2)/(x4_2-x1_2)))));

sigma1r=max(d,d1);

xx=linspace(1,10000,100);

yy1_2=tan(b2_S1_plus)*xx;
yy2_2=tan(b2_S1_minus)*xx;

a3_2=y3_2/(x3_2-10000);
b3_2=-10000*a3_2;
yy3_2=a3_2*xx+b3_2;

a4_2=y4_2/(x4_2-10000);
b4_2=-10000*a4_2;
yy4_2=a4_2*xx+b4_2;
% figure
% plot(xx,yy1_2,'r')
% hold on
% plot(xx,yy2_2,'b')
% hold on
% plot(xx,yy3_2,'r')
% hold on
% plot(xx,yy4_2,'b')

xi=[POS2(1,1);POS2(2,1);POS1(1,1);POS1(2,1)];
%
% figure
% plot(xx,yy1,'r')
% hold on
% plot(xx,yy2,'r')
% hold on
% plot(xx,yy3,'r')
% hold on
% plot(xx,yy4,'r')
% hold on
% plot(xx,yy1_2,'b')
% hold on
% plot(xx,yy2_2,'b')
% hold on
% plot(xx,yy3_2,'b')
% hold on

```

```

% plot(xx,yy4_2,'b')
%
% text(POS1(1,1),POS1(2,1),'POS1')
% text(POS2(1,1),POS2(2,1),'POS2')

% *****BOT.m*****
% *****Written by LT Eftychios Psarakis Hellenic Navy*****
% ***Thesis Project: Simulation of Performance of Infrared Photodetectors***
% *****

clear,clc
disp('for no mesurement noise select 0')
disp('for mesurement noise select 1')
mnoiseflag=input('SELECT NOISE OR NO NOISE CASE:');

disp('for single sensor tracking select 0')
disp('for two sensor tracking select 1')
twosensorflag=input('SELECT ONE OR TWO SENSORS CASE:');

s2p = [10000;0]; % Sensor 2 position (Sensor 1 is at (0/0)
%rand('seed',0);
de1ta = 0.1; %Time
nsamples = 1000;
initialization;
x = xi;
q = 1000;
Q= [de1ta^3/3, de1ta^2/2; de1ta^2/2, de1ta];
Qi = [Q, zeros(2); zeros(2),Q];
Q = q*Qi;
sb = 1*pi/180;
D=[1, 0, 0, 0;
  1/dt, 0, -1/dt, 0;
  0, 1, 0, 0;
  0, 1/dt, 0, -1/dt];
x_sp=D*xi;
speed=sqrt((x_sp(2,1))^2+(x_sp(4,1))^2)*2000/3600
w1=input('SELECT THE DESIRED ACCELERATION IN G')
w = w1*10/speed;

R = sb;
xout = [];
tout = [];
terr = [];
chi2err = [];
% xhat = x + [100*randn;5*randn;100*randn;5*randn];
xhat = x + 0.6*[100;5;100;5];

```

```

phat = [d1^2 ,0 ,0 ,0;
         0 ,d1^2 ,0 ,0;
         0 ,0 ,d^2 ,0;
         0 ,0 ,0 ,d^2]

```

```

F=[0,           1,           0,           0;
   0,           0,           0,           -w;
   0,           0,           0,           1;
   0,           w,           0,           0];

```

```

Fturn = expm(F*de1ta)

```

```

F   =[1,    de1ta,           0,           0;
      0,    1,           0,           0;
      0,    0,           1,           de1ta;
      0,    0,           0,           1];

```

```

Hp = [1 0 0 0; 0 0 1 0];
for ii =1:nsamples
% Take a measurement

```

```

b = atan2(x(3),x(1));
if mnoiseflag== 1
z = b + sb*randn;
else
z = b;
end
xout = [xout, [x(1) ;x(3) ]];

```

```

% EKF Update
r2 =xhat(1)^2 + xhat(3)^2;
b = atan2(xhat(3),xhat(1));
zhat = b;
H= [-xhat(3)/r2, 0, xhat(1)/r2,0];
Pzi=inv(H*phat*H' + R);
zt = z - zhat;
chi2 =zt'*Pzi*zt;
K = phat*H'*Pzi;
K2 = eye(4)-K*H;
xhat =xhat + K*zt;
phat = K2*phat*K2' + K*R*K';

```

```

if twosensorflag ==1 % process measuransnt frcm second sensor
% Take a Measuronent

```

```

rp = Hp*x - s2p;
b = atan2(rp(2),rp(1));
if mnoiseflag == 1
z = b + sb*randn;
else
z = b;
end
% Measurant update
rp = Hp*xhat - s2p;
r2 = rp'*rp;
b = atan2(rp(2),rp(1));
zhat = b;
H= [-rp(2)/r2, 0, rp(1)/r2, 0] ;
Pzi = inv(H*phat*H' + R) ;
zt = z- zhat;
chi2 = zt'*Pzi*zt;
K = phat*H'*Pzi;
K2 = eye(4) - K*H;
xhat = xhat + K*zt;
phat = K2*phat*K2' + K*R*K';

end
e = [xhat(1);xhat(3)];
tout =[tout,e] ;
e = e - [x(1);x(3)];
terr = [terr,sqrt(e'*e)];
chi2err = [chi2err,chi2];
% Target Motion
if ((ii > 250) & (ii <= 350))
x = Fturn*x;
else
x = F*x;
end
% Track Prediction
xhat=F*xhat;
phat=F*phat*F' + Q;
end % for ii
if mnoiseflag==0 && twosensorflag==0
tlabe1 = ['B0 Tracking single Sensor,no Noise,q^2 = 1000, accel
=',num2str(w1),'g'];
elseif mnoiseflag==1 && twosensorflag==0
tlabe1 = ['B0 Tracking single Sensor,Noise presence,q^2 = 1000, accel
=',num2str(w1),'g'];
elseif mnoiseflag==0 && twosensorflag==1
tlabe1 = ['B0 Tracking two Sensors, no Noise,q^2 = 1000, accel
=',num2str(w1),'g'];

```

```

elseif mnoiseflag==1 && twosensorflag==1
    tlabe1 = ['B0 Tracking two Sensors,Noise presence,q^2 = 1000, accel
=',num2str(w1),'g'];
    end
    figure
    subplot(2,1,1)
    plot(xout(1,:),xout(2,:), ':',tout(1, :),tout(2,:),'r');
    %tit1e('Target and Track');
    title ([tlabe1]);
    xlabel('meters')
    ylabel('meters')
    legend('true position','Track position')
    grid
    subplot(2,1,2)
    plot(xout(1,:),xout(2,:), ",",tout(1, :),tout(2,:),'r');
    %tit1e('Target and Track');
    title ([tlabe1]);
    xlabel('meters')
    ylabel('meters')
    legend('true position','Track position')
    axis([.6*10^4,3.3*10^4,3*10^4,13*10^4])
    grid
    figure
    tt = [0: (max (size(terr))-1)] *de1ta;
    subplot(2,1,1)
    plot (tt,terr, 'r');
    title ([ 'Track Position Errors: ',tlabe1]);
    xlabel('Sample number')
    ylabel('meters')
    grid
    subplot(2,1,2)
    tt = [0: (max(size (chi2err))-1)] *de1ta;
    plot (tt,chi2err, 'r');
    title ('Chi-Squared Values for Measurement Association');
    xlabel('Sample number')
    ylabel('rad')
    grid

```

APPENDIX C: ASYMPTOTIC EXPRESSIONS

Appendix C presents the Airy function considerations for the low bias simulation of the quantum well.

A. AIRY FUNCTION ANALYSIS

1. General

The differential equation $\frac{d^2w}{dz^2} - z\omega = 0$, where $\zeta = 2/3 z^{3/2}$ and $\omega = e^{2\pi i/3}$, can be reduced to the differential equation satisfied by Bessel functions of order 1/3 [33, sec. 6.4]. There are two linearly independent solutions which are called Airy functions of the first and the second kind.

$$Ai(z) = \frac{1}{3} z^{\frac{1}{2}} [I_{-1/3}(\zeta) - I_{1/3}(\zeta)] \quad (C.1)$$

$$Bi(z) = \left(\frac{\sqrt{z}}{3} \right)^{1/2} [I_{-1/3}(\zeta) + I_{1/3}(\zeta)] \quad (C.2)$$

$$Ai(-z) = \frac{1}{3} z^{\frac{1}{2}} [J_{-1/3}(\zeta) + J_{1/3}(\zeta)] \quad (C.3)$$

$$Bi(-z) = \left(\frac{z}{3} \right)^{1/2} [J_{-1/3}(\zeta) - J_{1/3}(\zeta)] \quad (C.4)$$

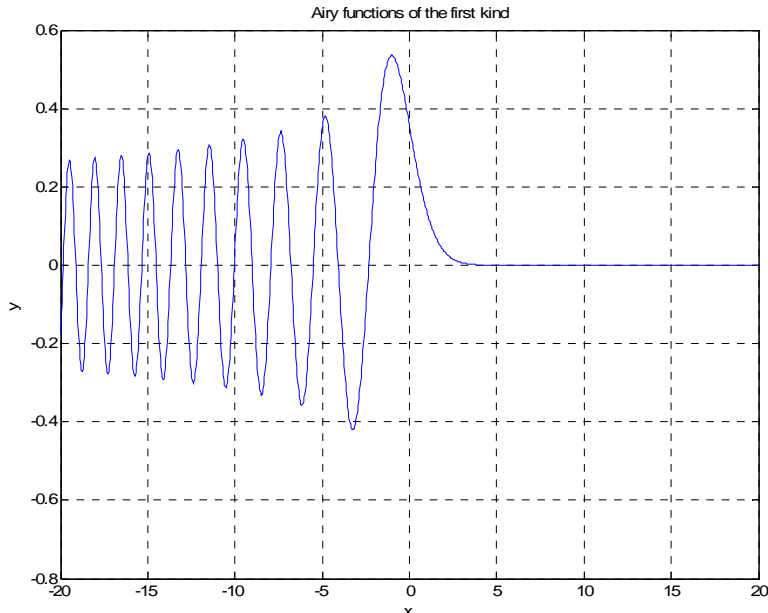


Figure C.1: Airy functions of the first kind, $Ai(-z)$ and $Ai(z)$

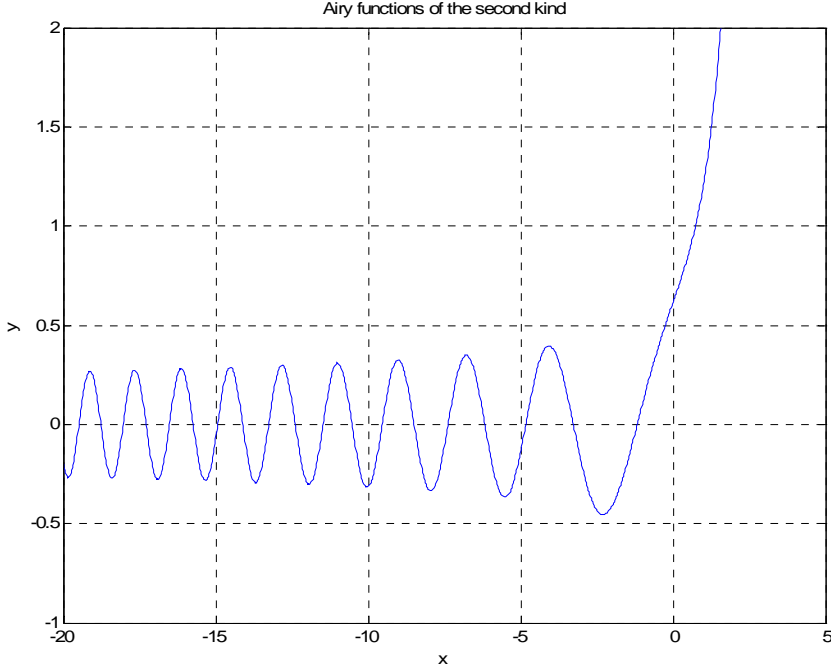


Figure C.2: Airy functions of the second kind, $Bi(-z)$ and $Bi(z)$

2. Asymptotic Expressions of Airy Functions

There are several problems associated with the direct approach to the solution of the Schrödinger equation using Airy's functions. The main drawback is the asymptotic behavior of Airy's functions and of their derivatives, when the used argument, is either very large or very small. In those cases personal computers give numerical overflows which significantly reduce the result quality and computational efficiency. These kinds of problems appear especially when low biases are applied in symmetric or asymmetric quantum wells structures.

The asymptotic forms of Airy's functions used for our simulations were taken from the handbook of mathematical functions [28, pp. 448-449].

$$Ai(z) \cong (4\pi)^{-\frac{1}{2}} z^{-\frac{1}{4}} e^{-\frac{2}{3}z^{\frac{3}{2}}}, z \gg 0 \quad (C.5)$$

$$Ai'(z) \cong -(4\pi)^{-\frac{1}{2}} z^{\frac{1}{4}} e^{-\frac{2}{3}z^{\frac{3}{2}}}, z \gg 0 \quad (C.6)$$

$$Ai(z) \cong (\pi)^{-\frac{1}{2}} (-z)^{-\frac{1}{4}} \sin\left(\frac{2}{3}(-z)^{\frac{3}{2}} + \frac{\pi}{4}\right), z \ll 0 \quad (C.7)$$

$$Ai(z) \cong -(\pi)^{-\frac{1}{2}}(-z)^{\frac{1}{4}} \cos\left(\frac{2}{3}(-z)^{\frac{3}{2}} + \frac{\pi}{4}\right), z \ll 0 \quad (C.8)$$

$$Bi(z) \cong (\pi)^{-\frac{1}{2}} z^{-\frac{1}{4}} e^{\frac{2}{3}z^{\frac{3}{2}}}, z \gg 0 \quad (C.9)$$

$$Bi(z) \cong (\pi)^{-\frac{1}{2}} z^{\frac{1}{4}} e^{\frac{2}{3}z^{\frac{3}{2}}}, z \gg 0 \quad (C.10)$$

$$Bi(z) \cong (\pi)^{-\frac{1}{2}}(-z)^{-\frac{1}{4}} \cos\left(\frac{2}{3}(-z)^{\frac{3}{2}} + \frac{\pi}{4}\right), z \ll 0 \quad (C.11)$$

$$Bi(z) = (\pi)^{-\frac{1}{2}}(-z)^{\frac{1}{4}} \sin\left(\frac{2}{3}(-z)^{\frac{3}{2}} + \frac{\pi}{4}\right), z \ll 0 \quad (C.12)$$

The expressions above give acceptable results not only when the argument is very large or extremely small but also when the argument is a finite number (not around zero) as shown in Figures C.3 and C.4. In the simulation code, written in Matlab, we have used a specific procedure so that when the built-in Matlab Airy functions give results, we take advantage and use them, but when the built-in functions are unable to give results we use Equations (C.5) through (C.12).

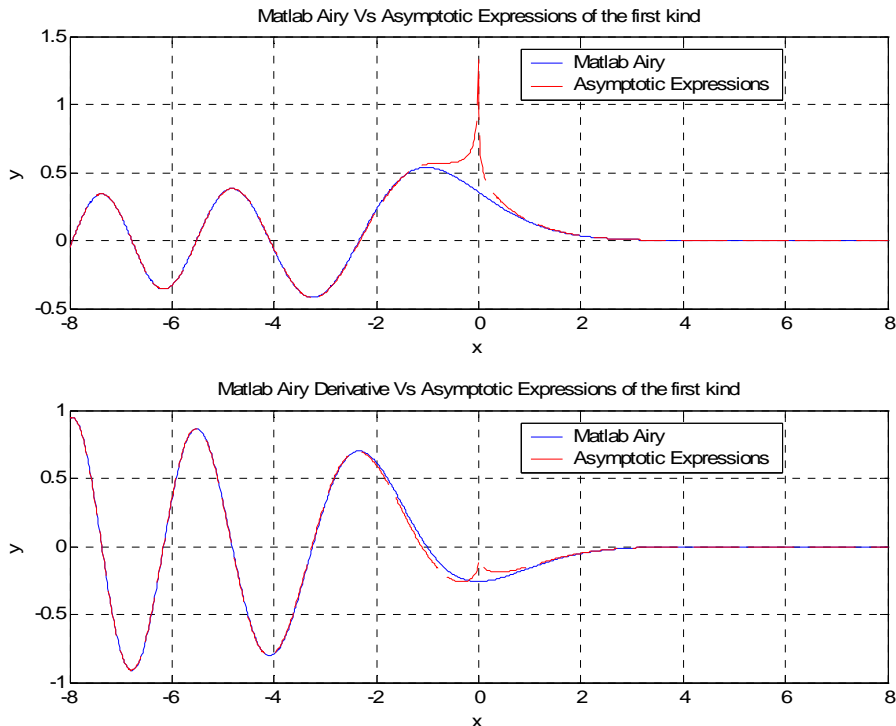


Figure C.3: Matlab Airy functions vs. asymptotic expressions of the first kind

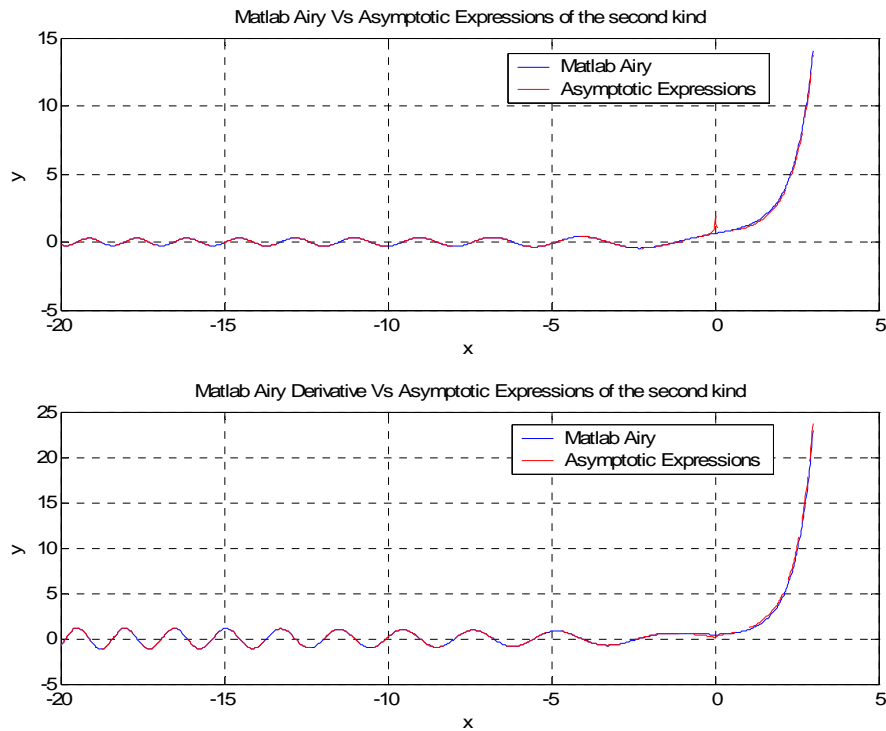
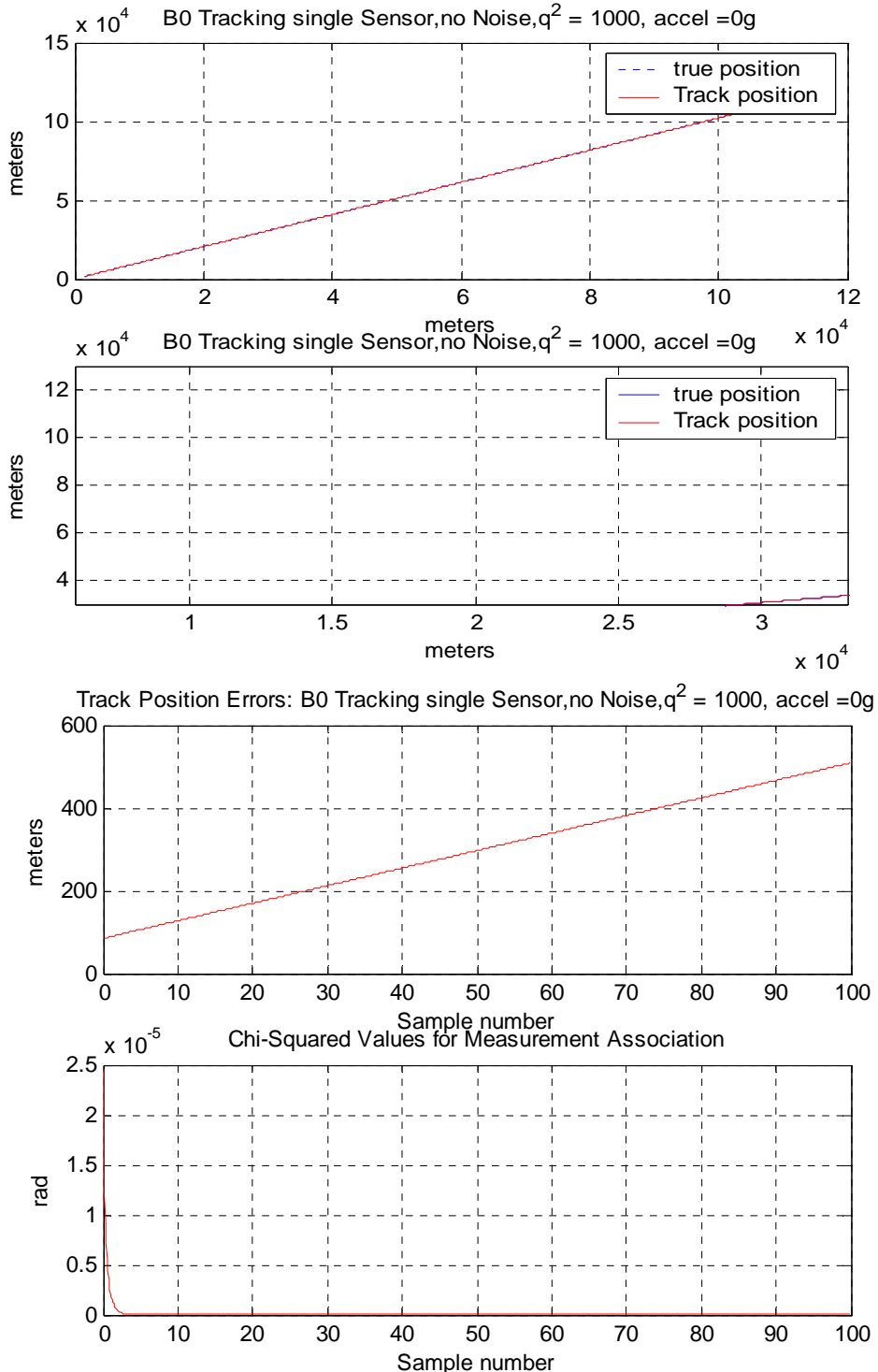
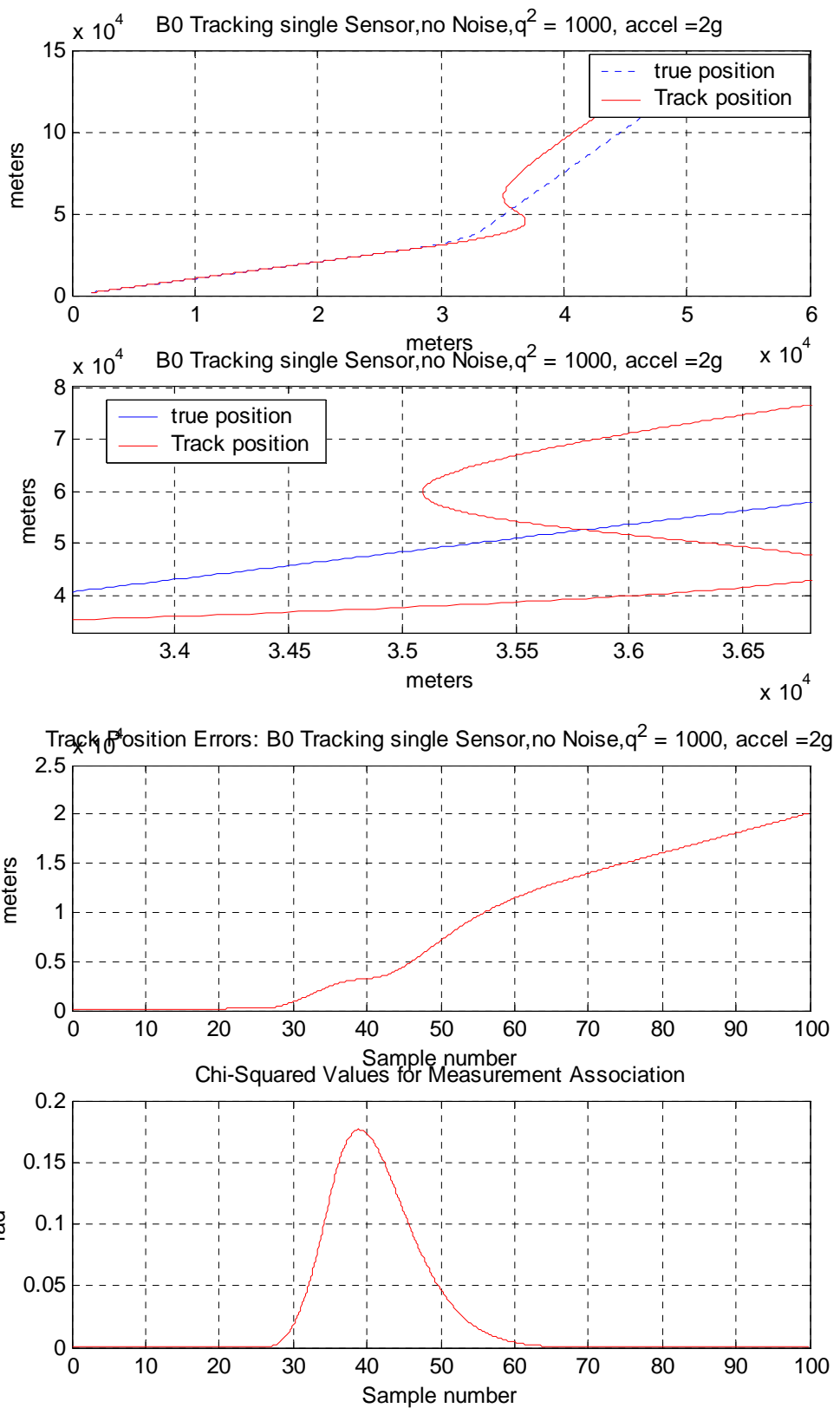


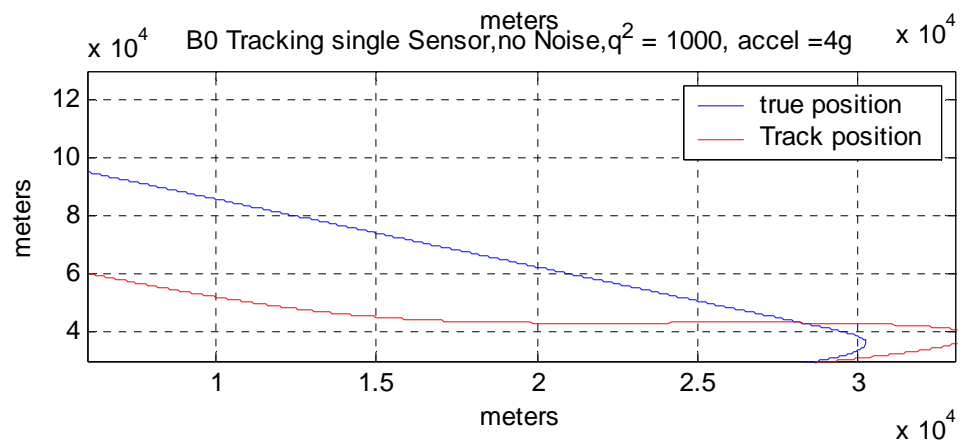
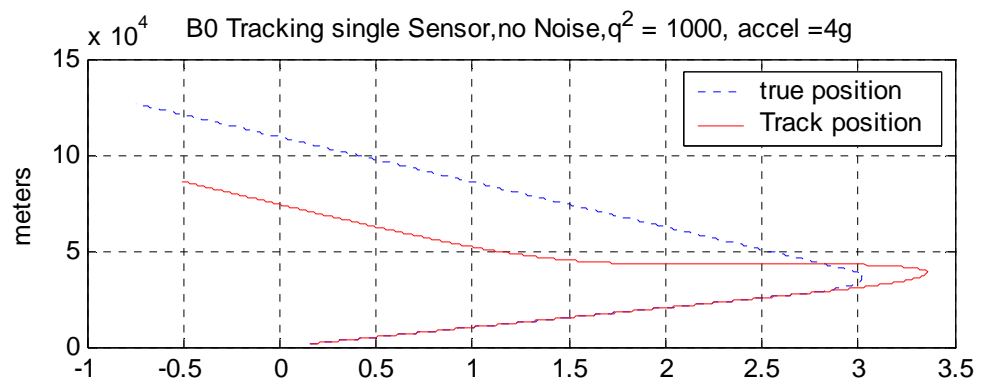
Figure C.4: Matlab Airy functions vs. asymptotic expressions of the second kind

APPENDIX D: BOT COMPLETE CASE SET

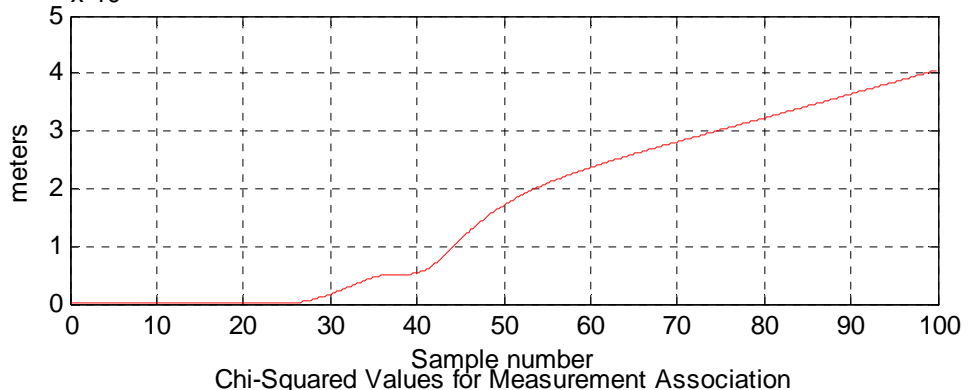
We present the complete results of the BOT simulation for 0 g, 2 g, 4 g, 6 g and 8 g turns, using one or two sensors, with and without the presence of measurement noise.



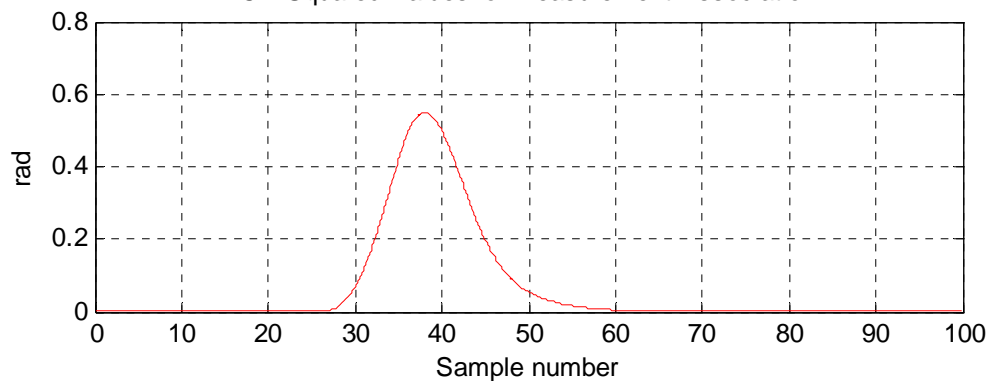


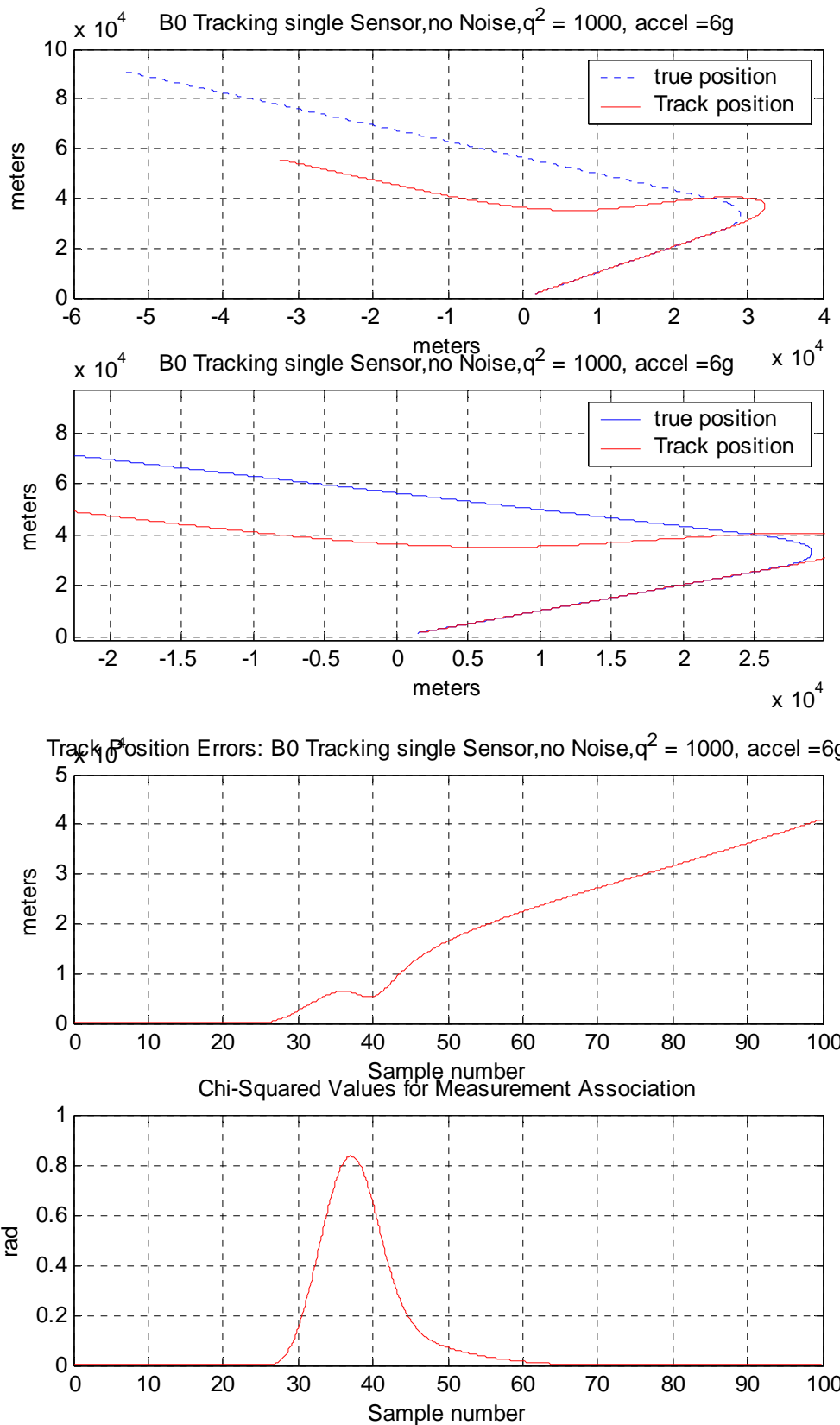


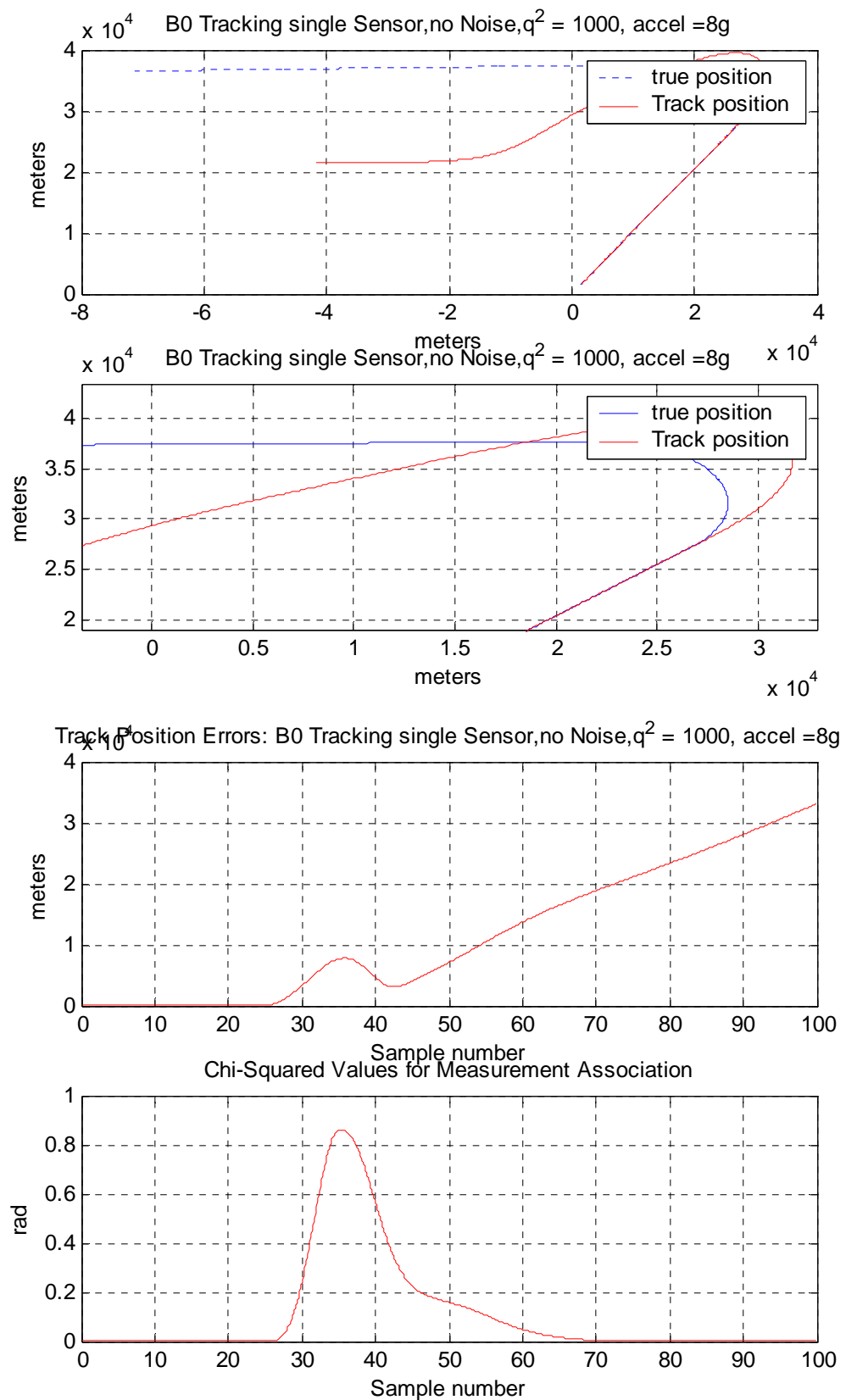
Track Position Errors: B0 Tracking single Sensor,no Noise, $q^2 = 1000$, accel =4g

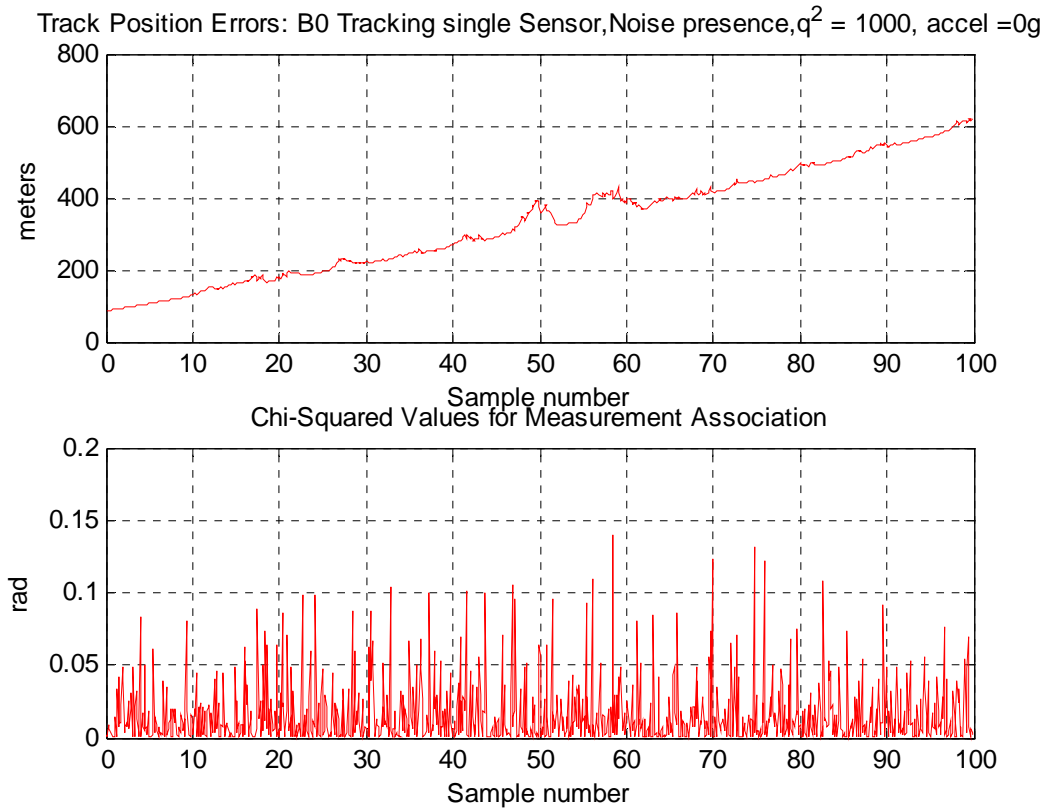
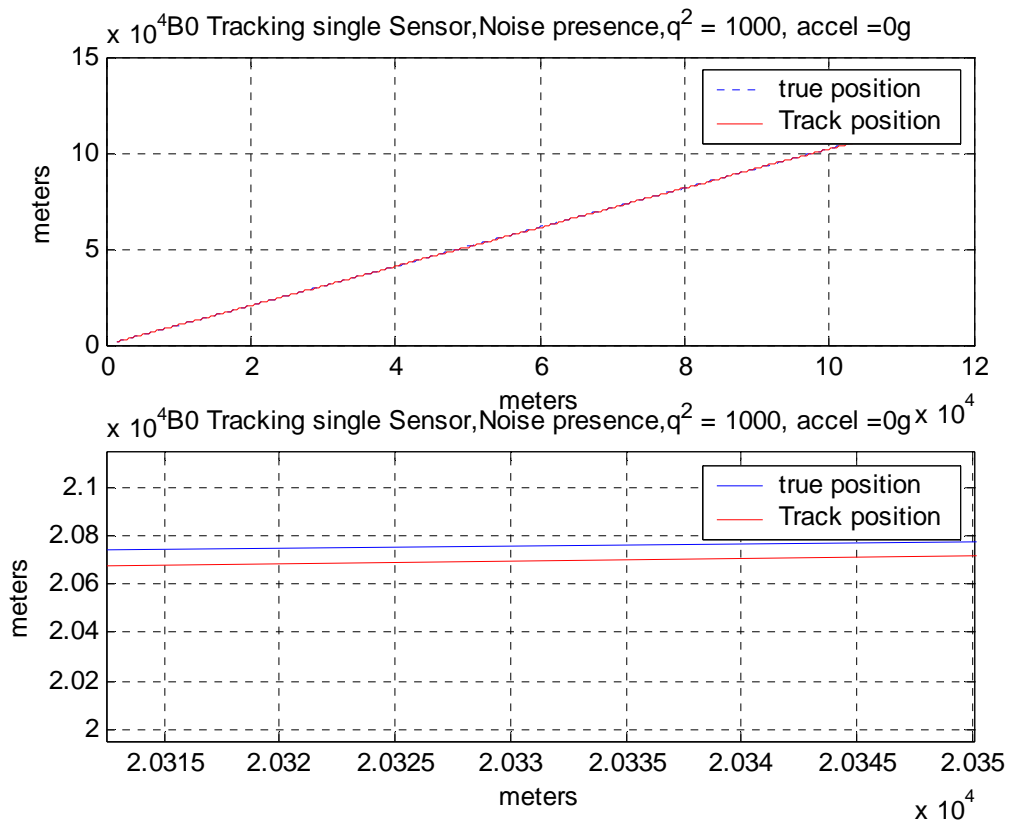


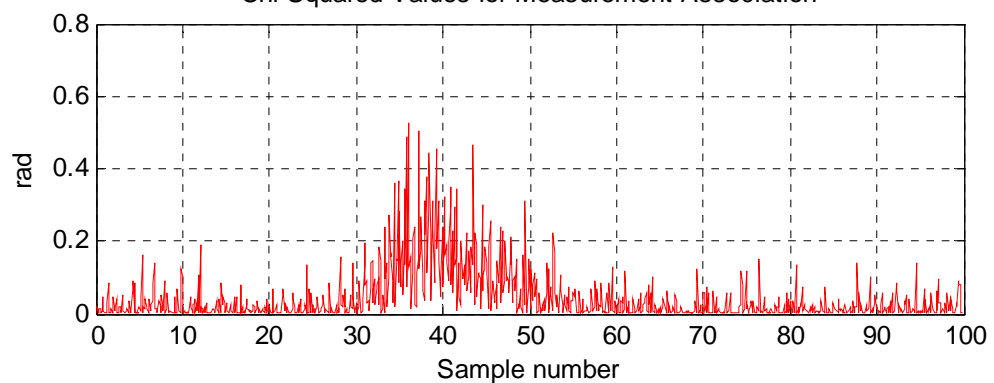
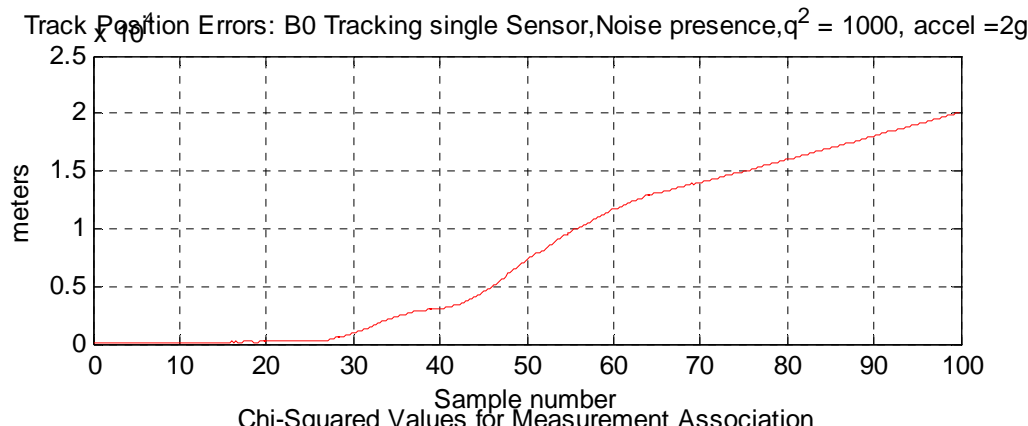
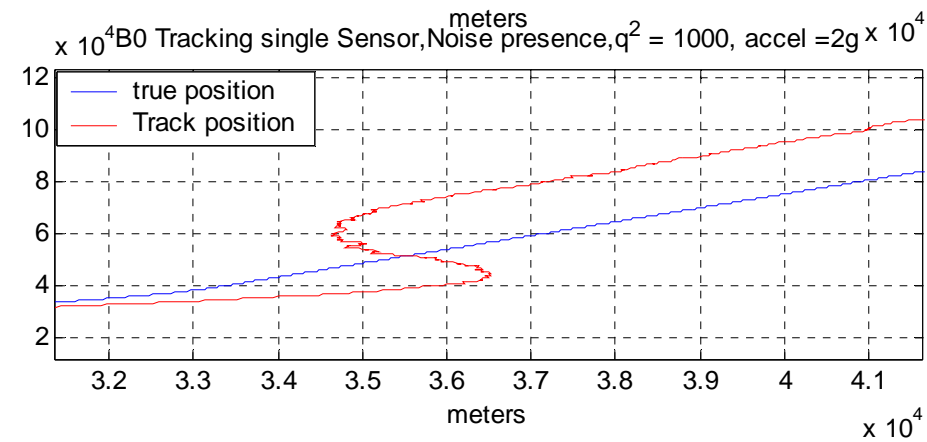
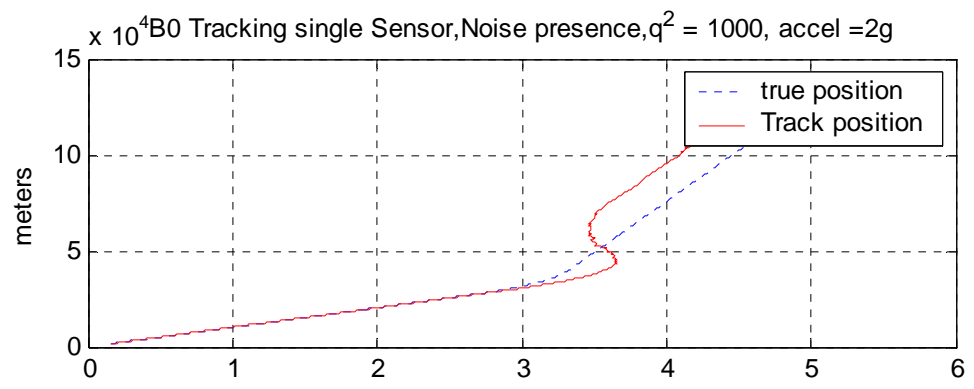
Chi-Squared Values for Measurement Association

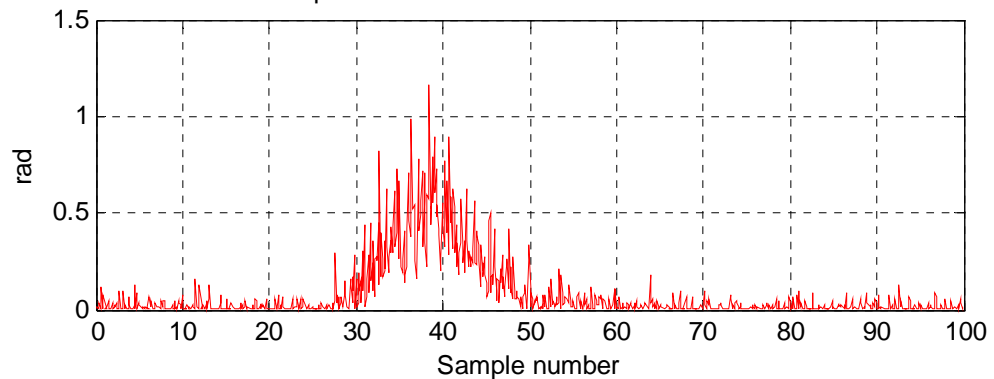
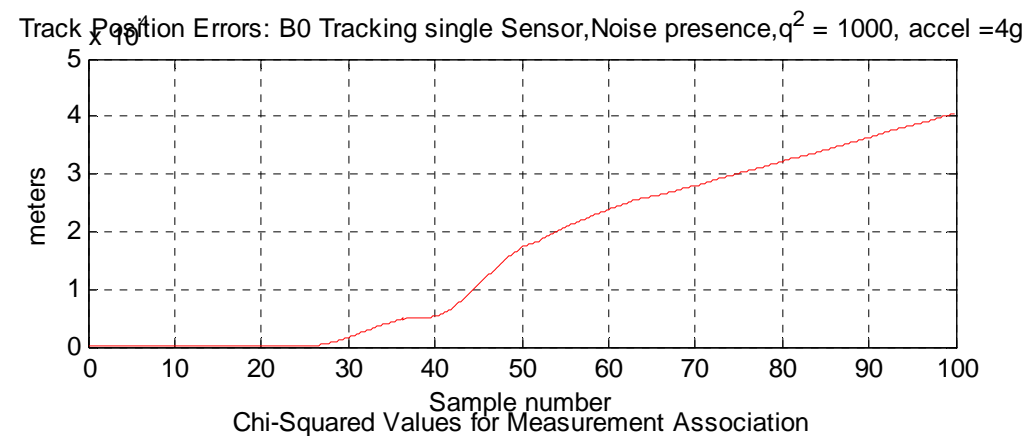
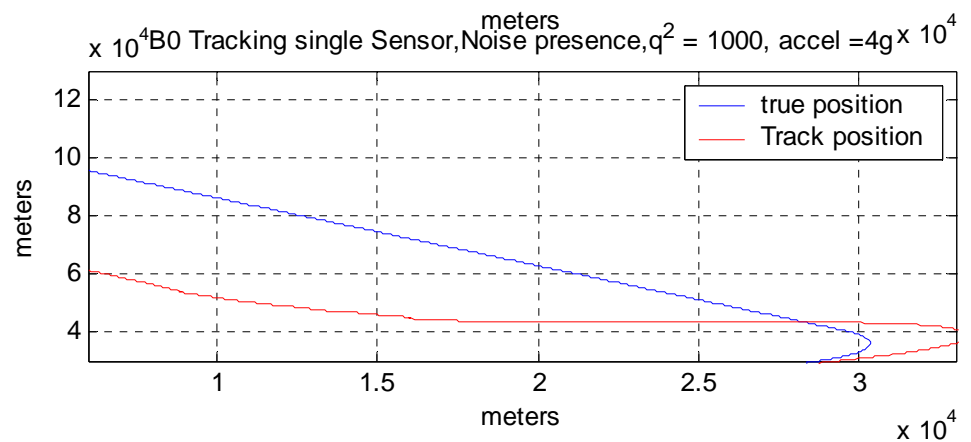
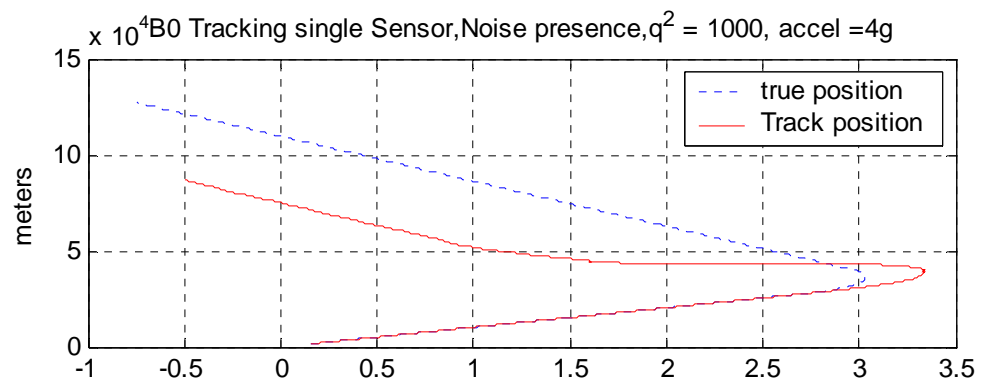


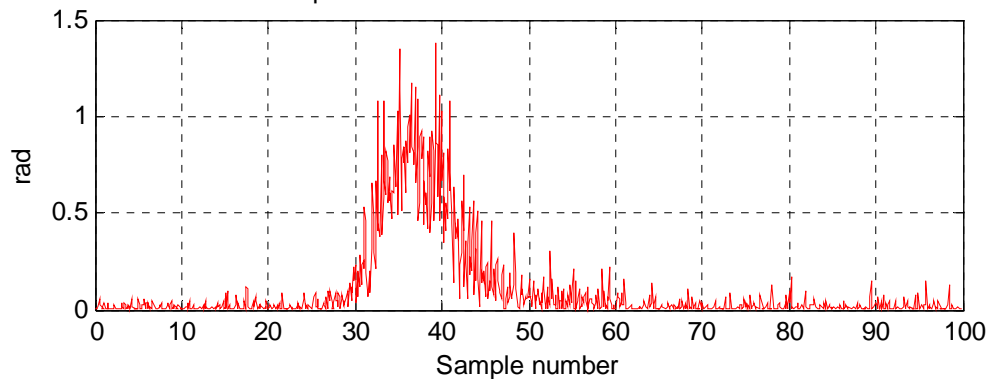
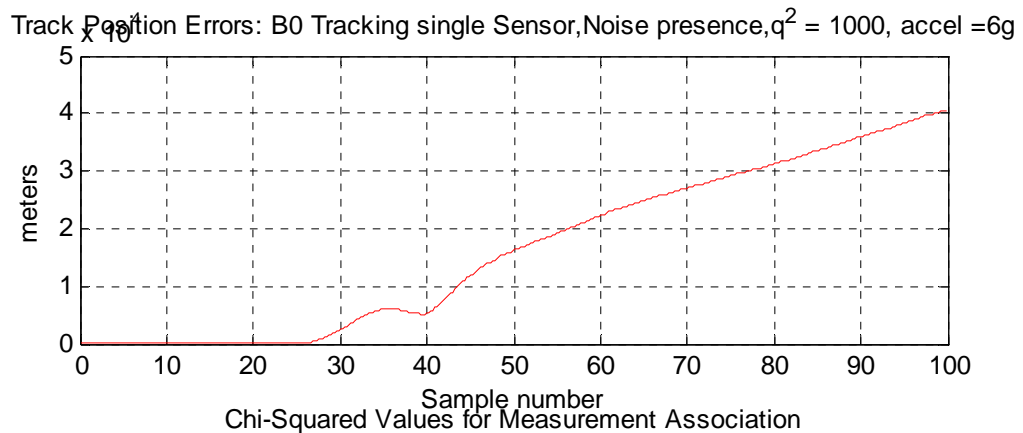
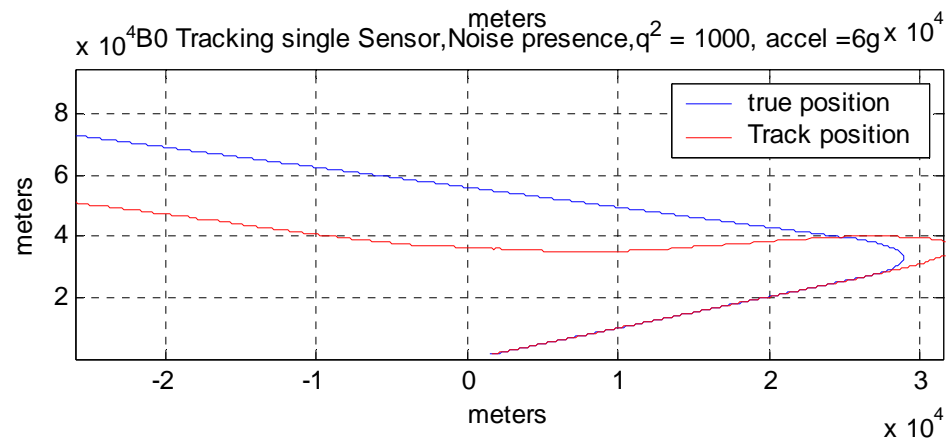
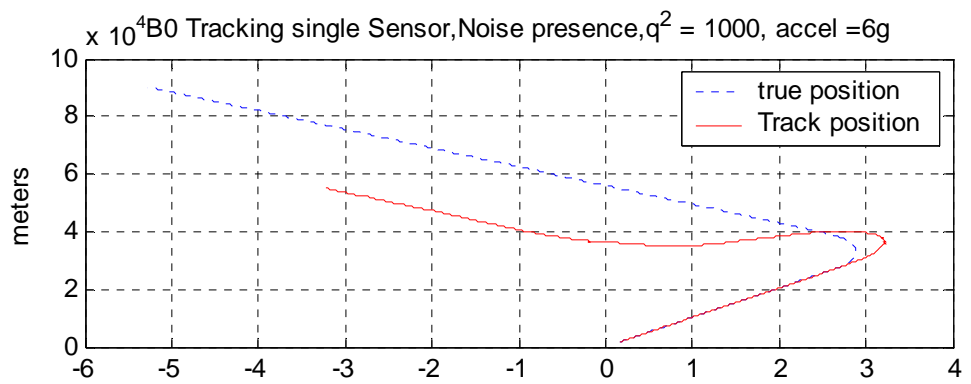


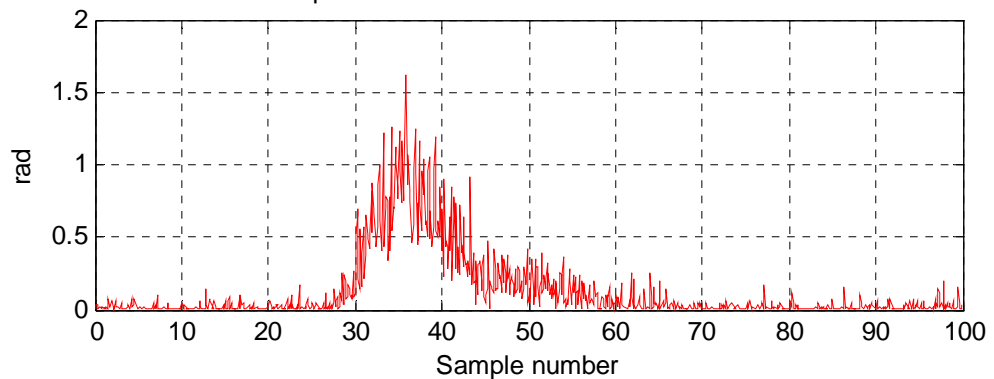
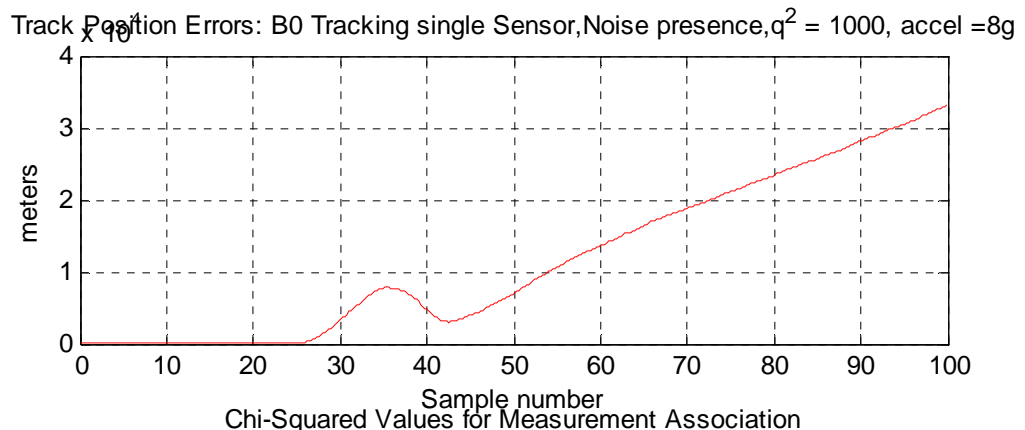
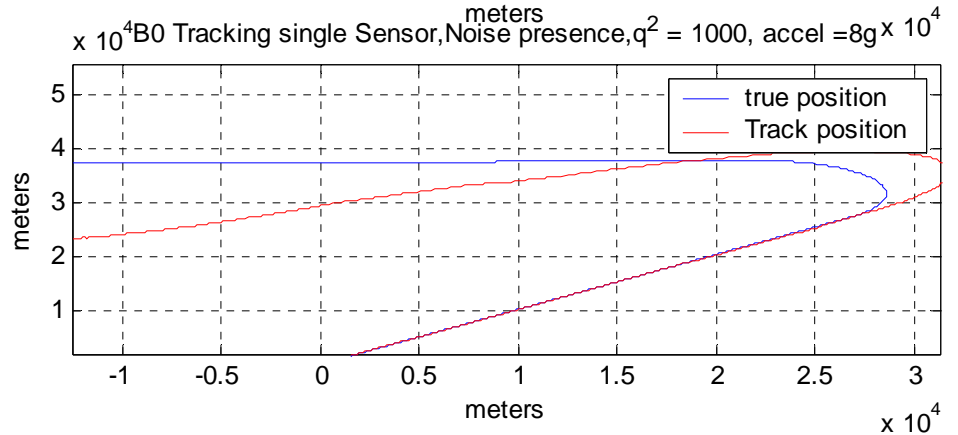
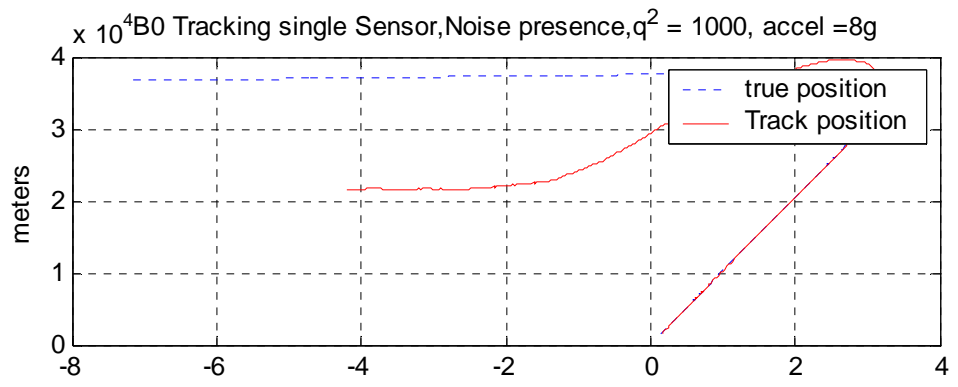


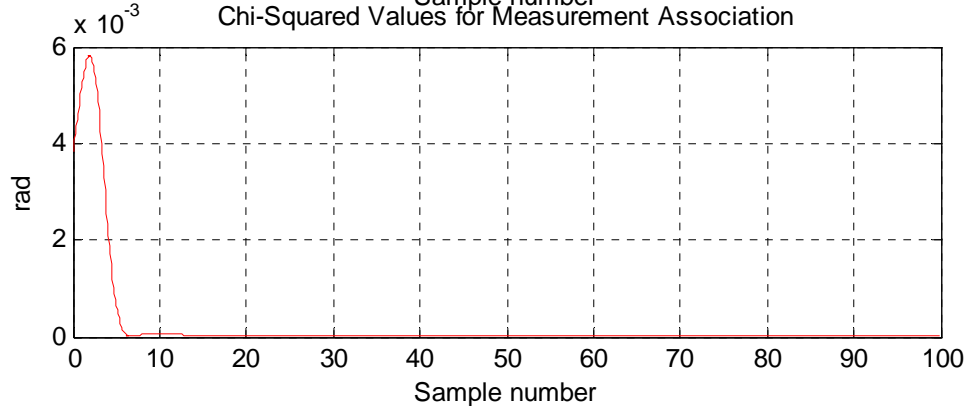
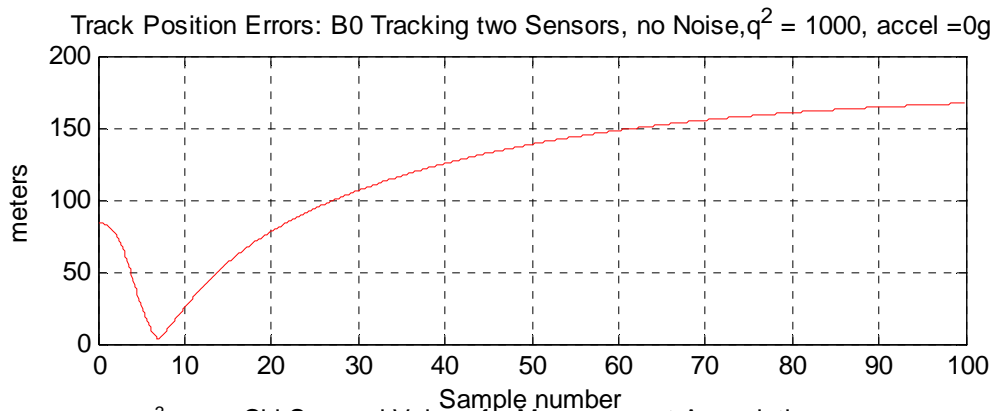
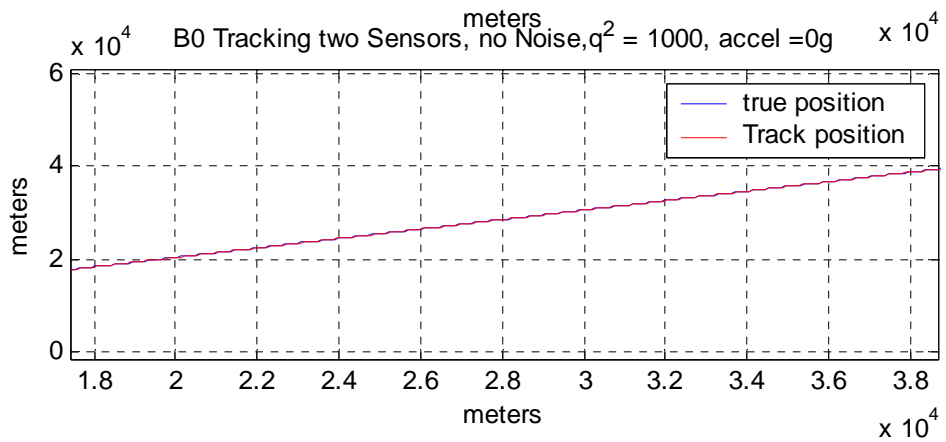
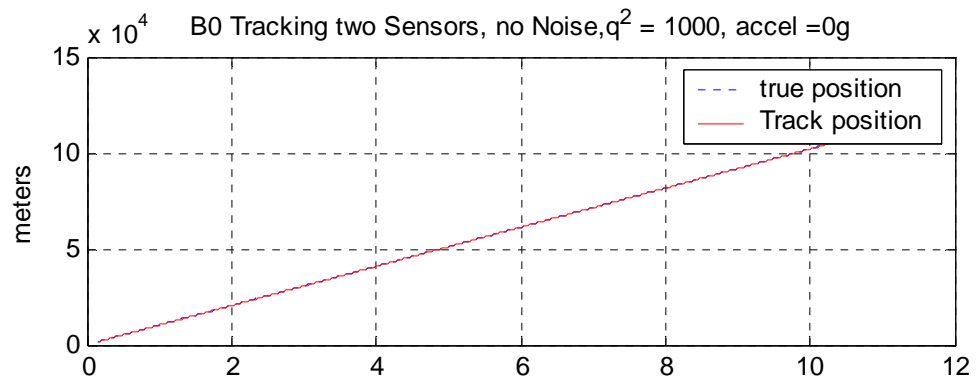


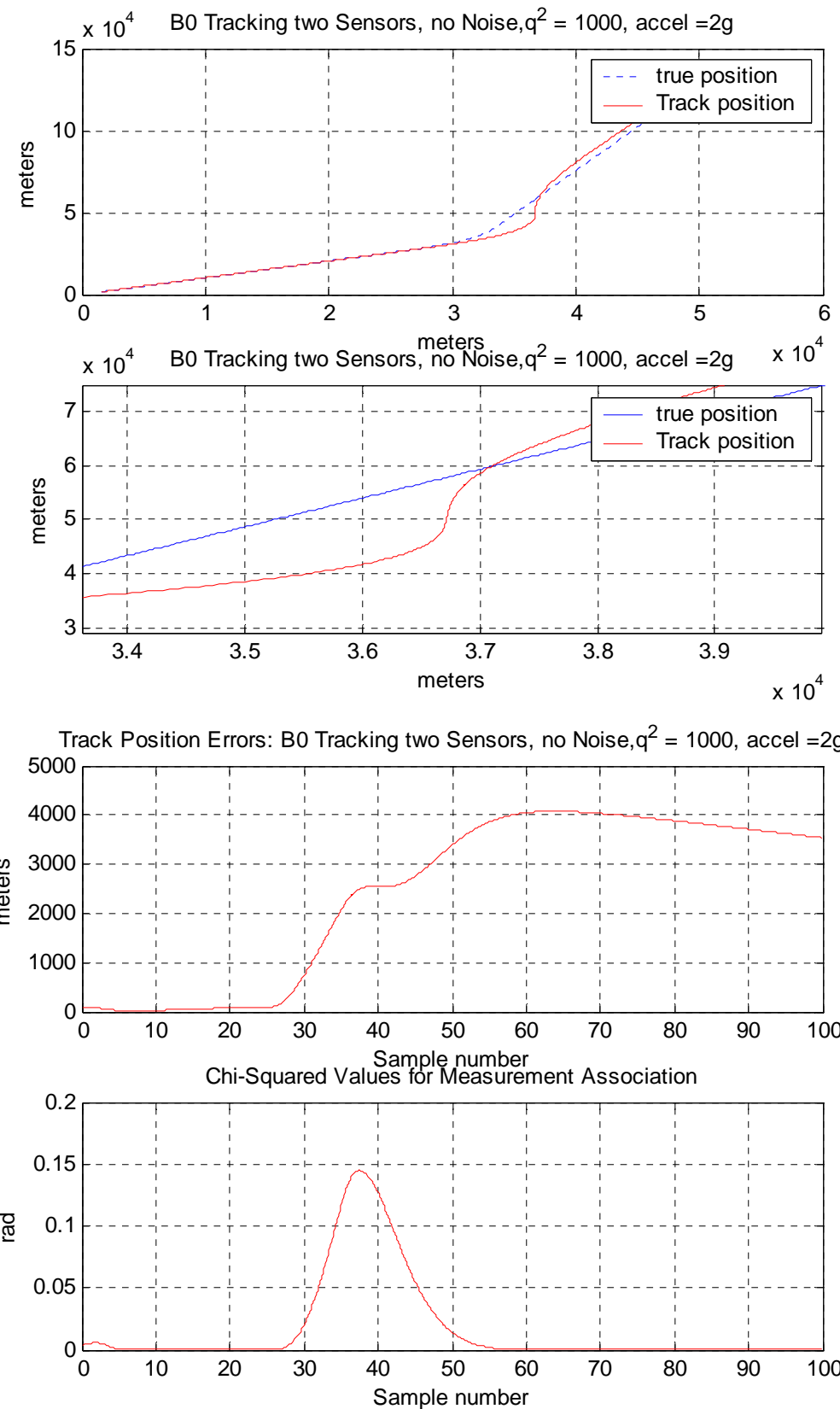


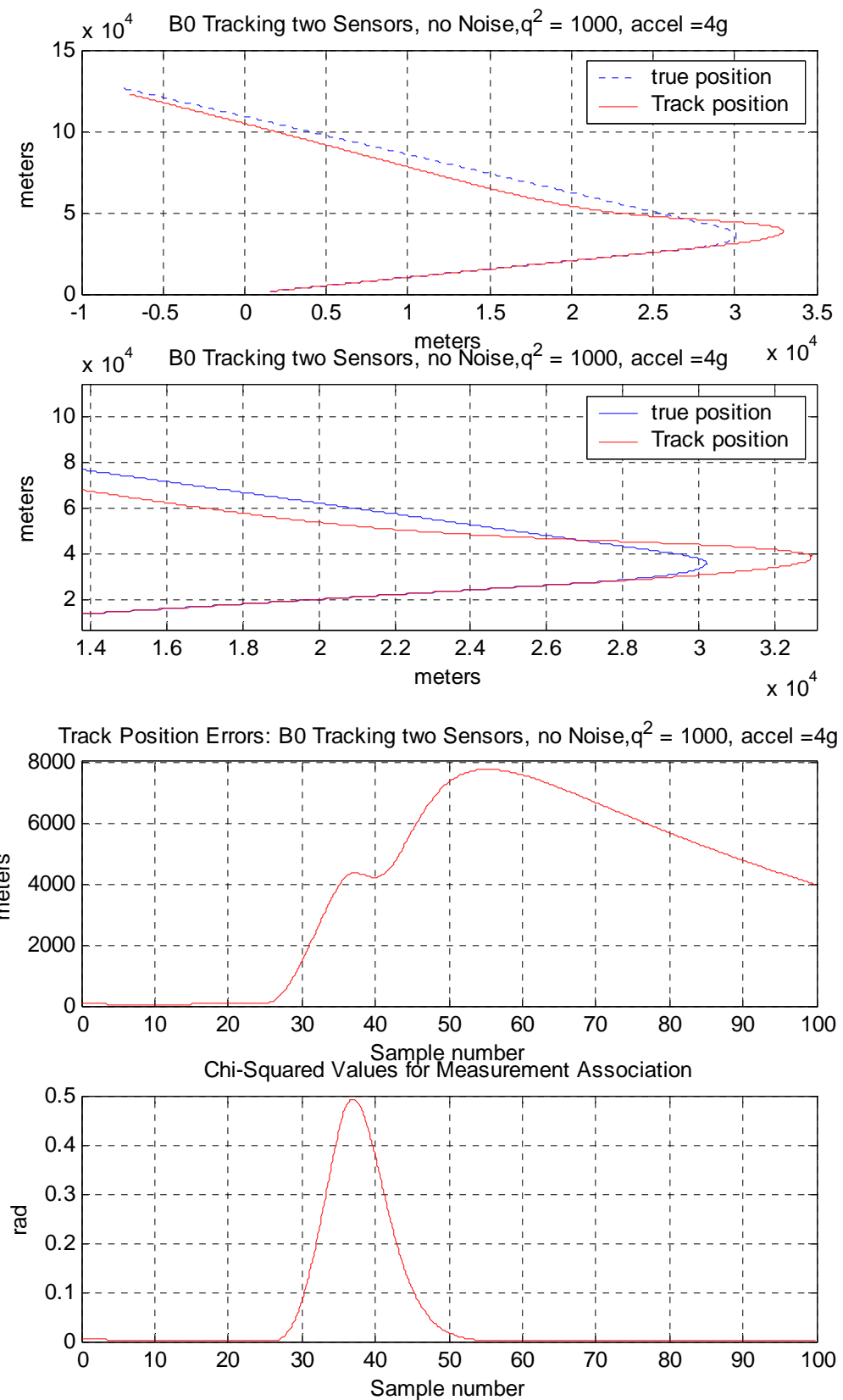


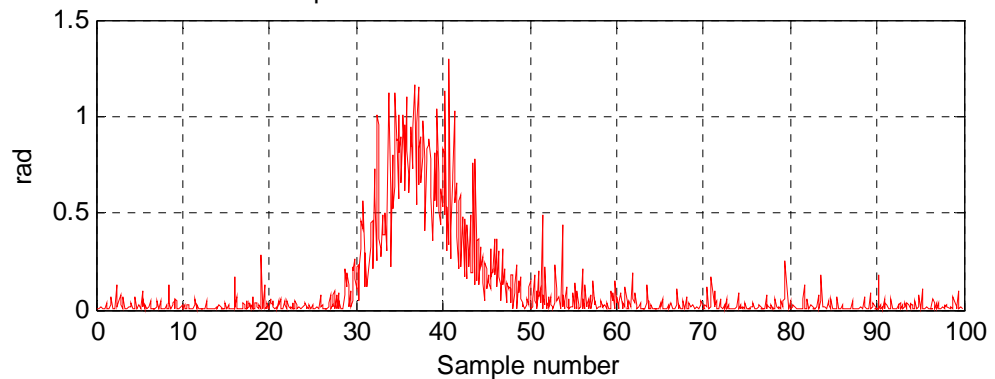
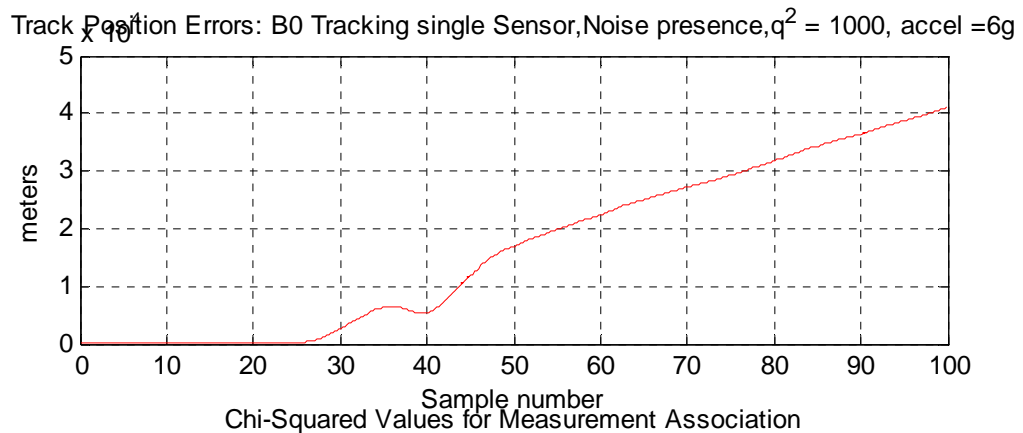
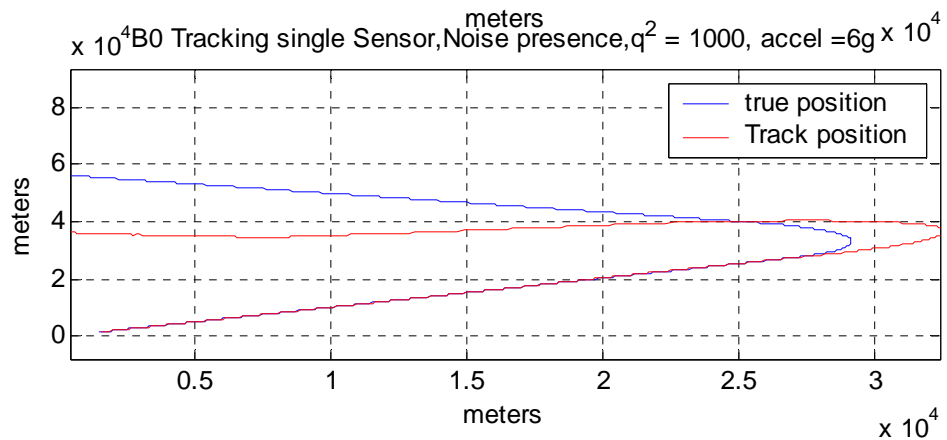
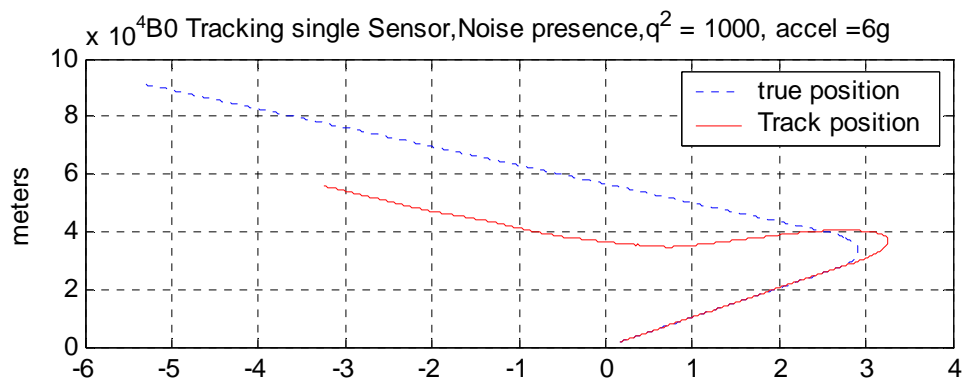


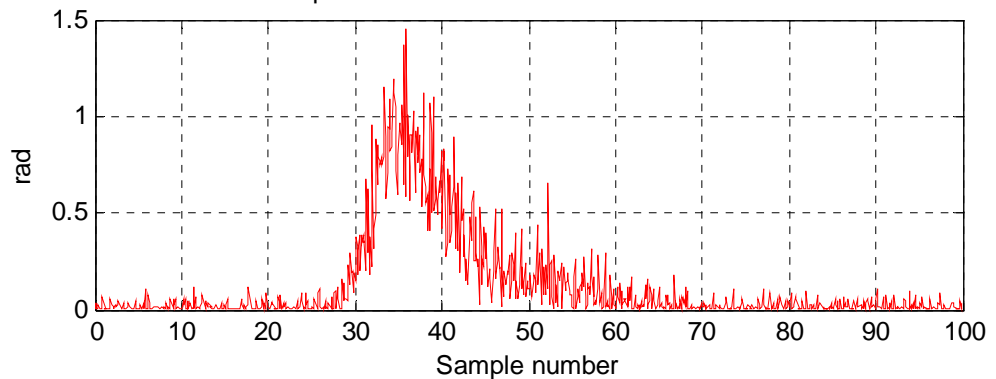
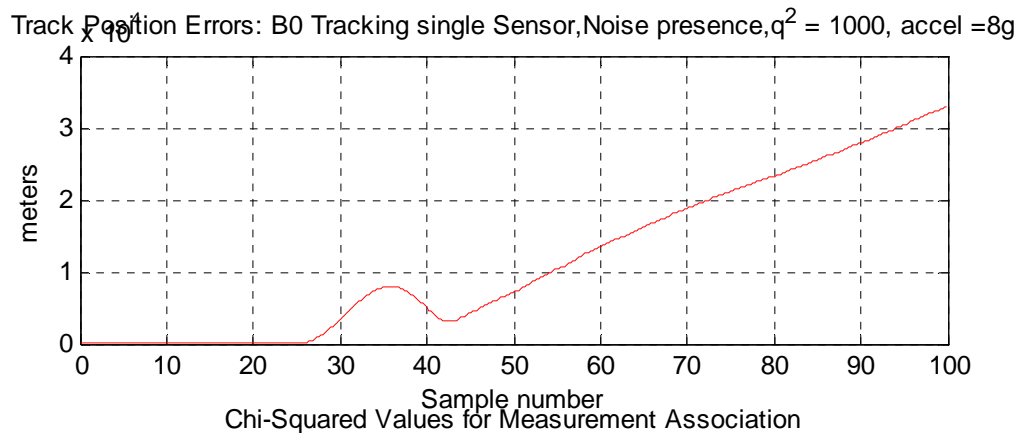
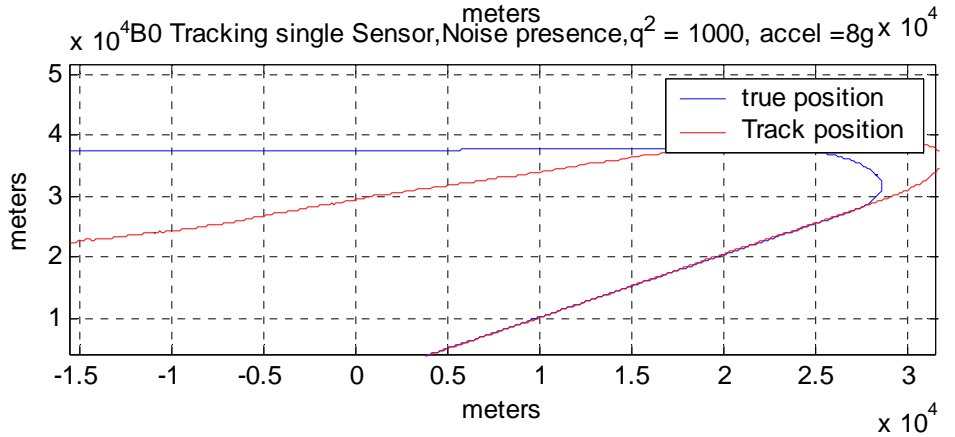
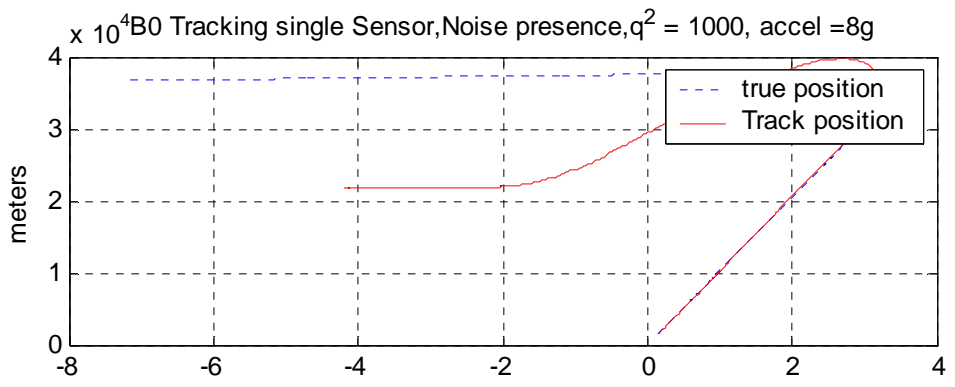


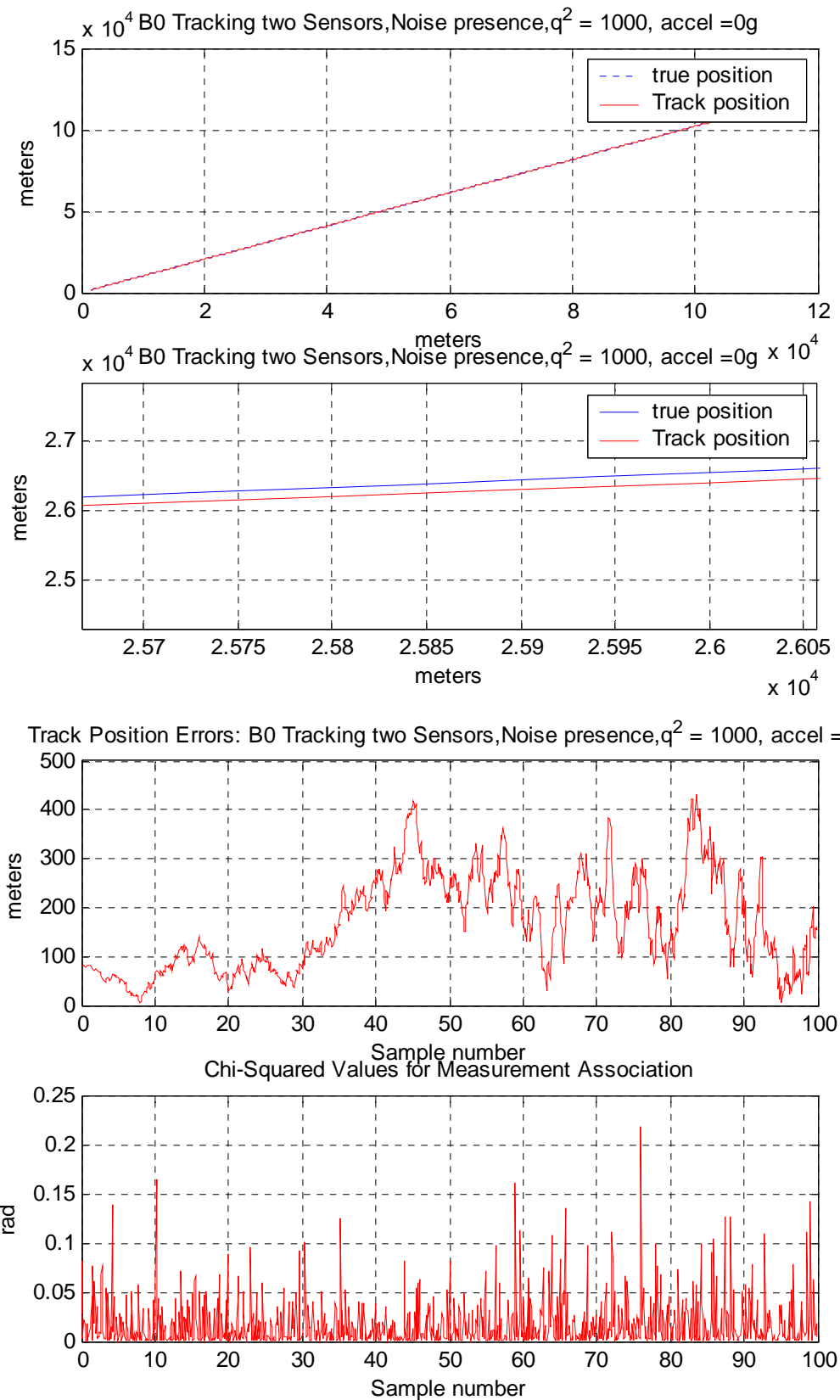


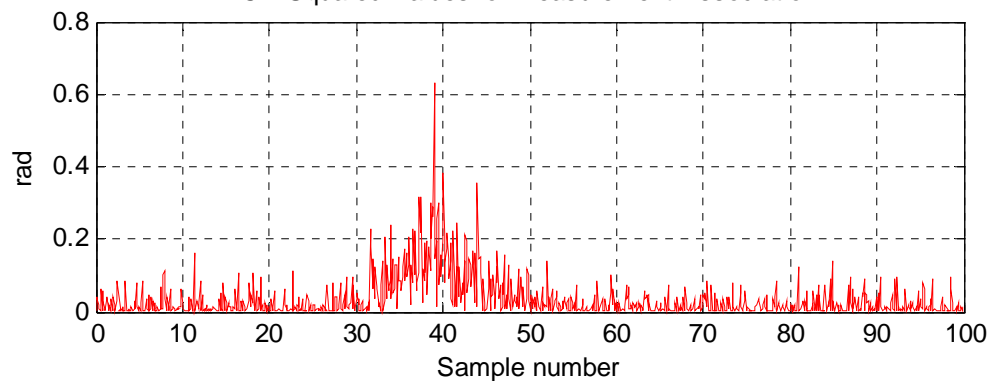
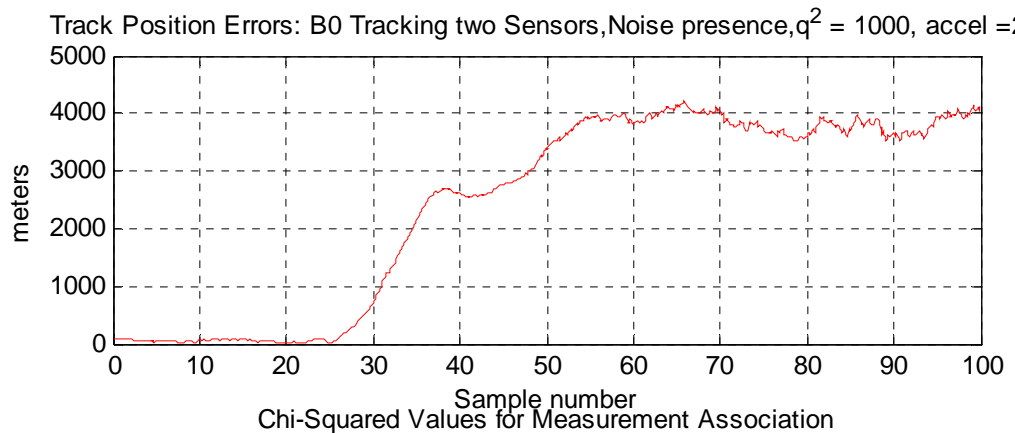
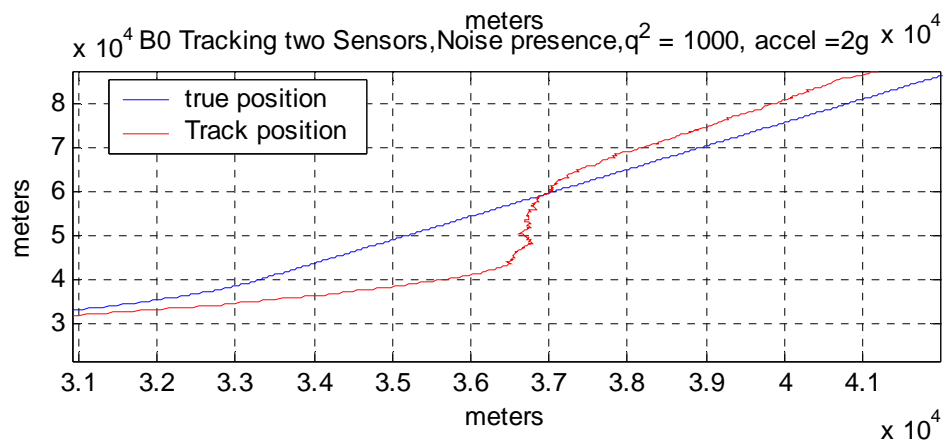
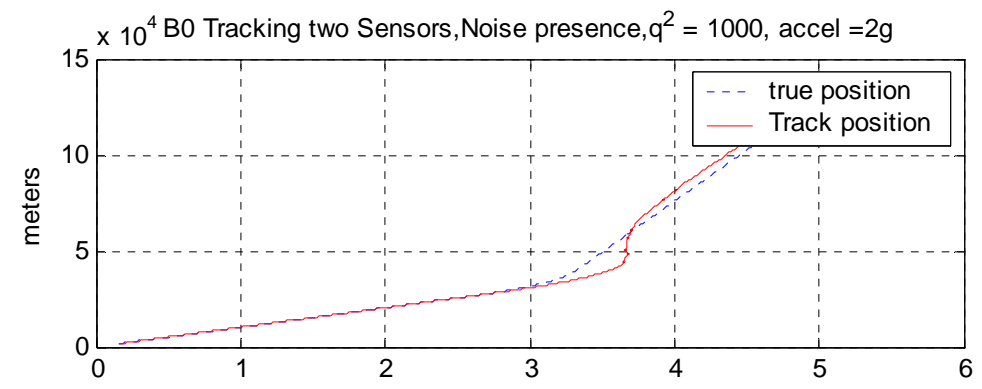


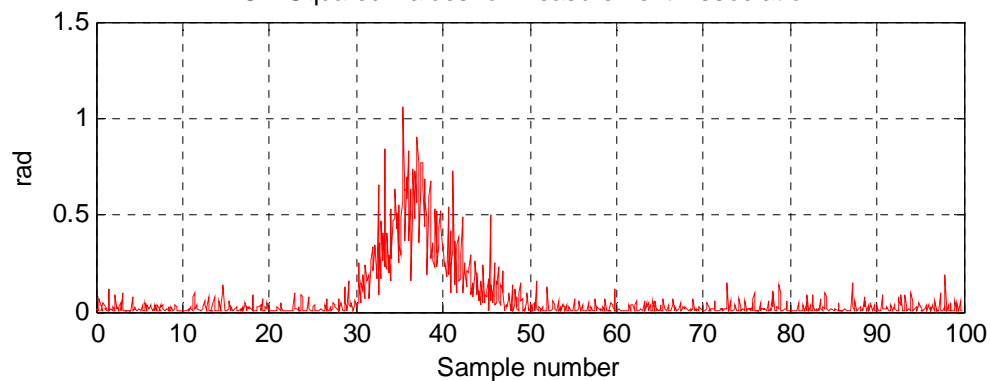
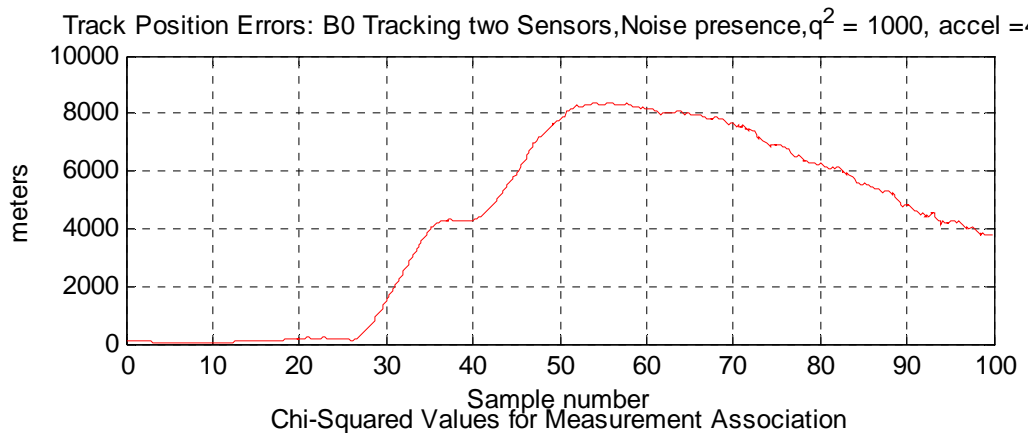
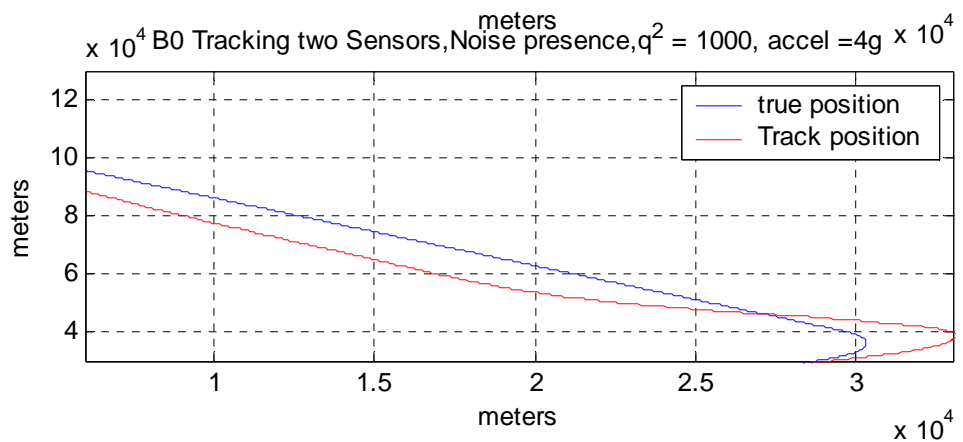
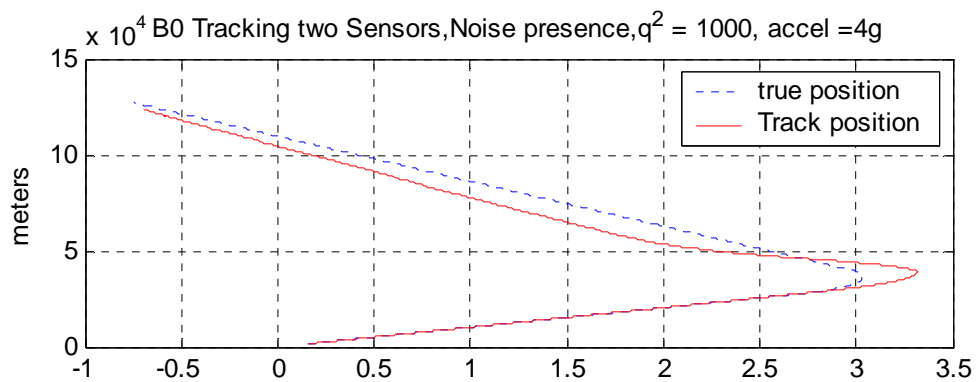


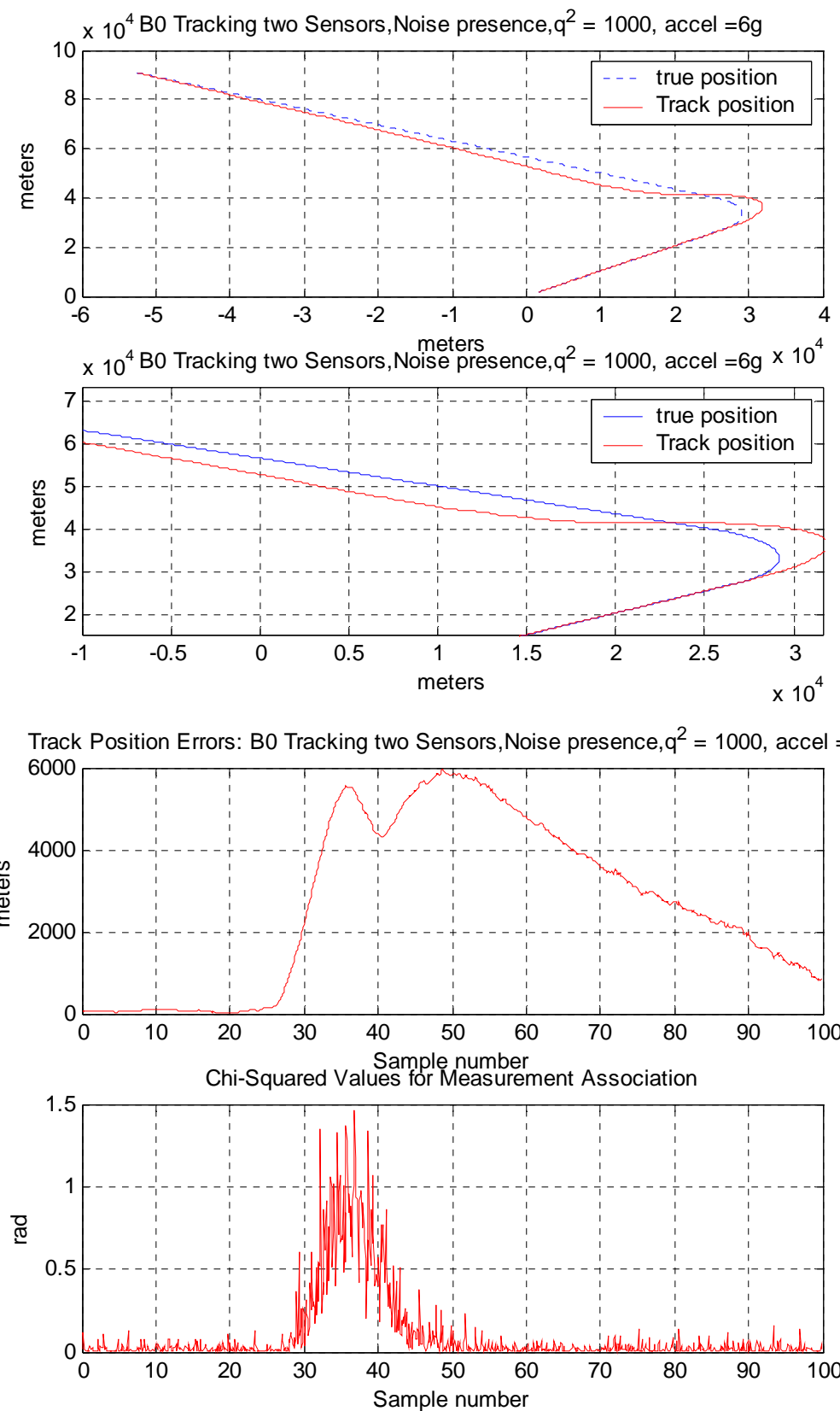


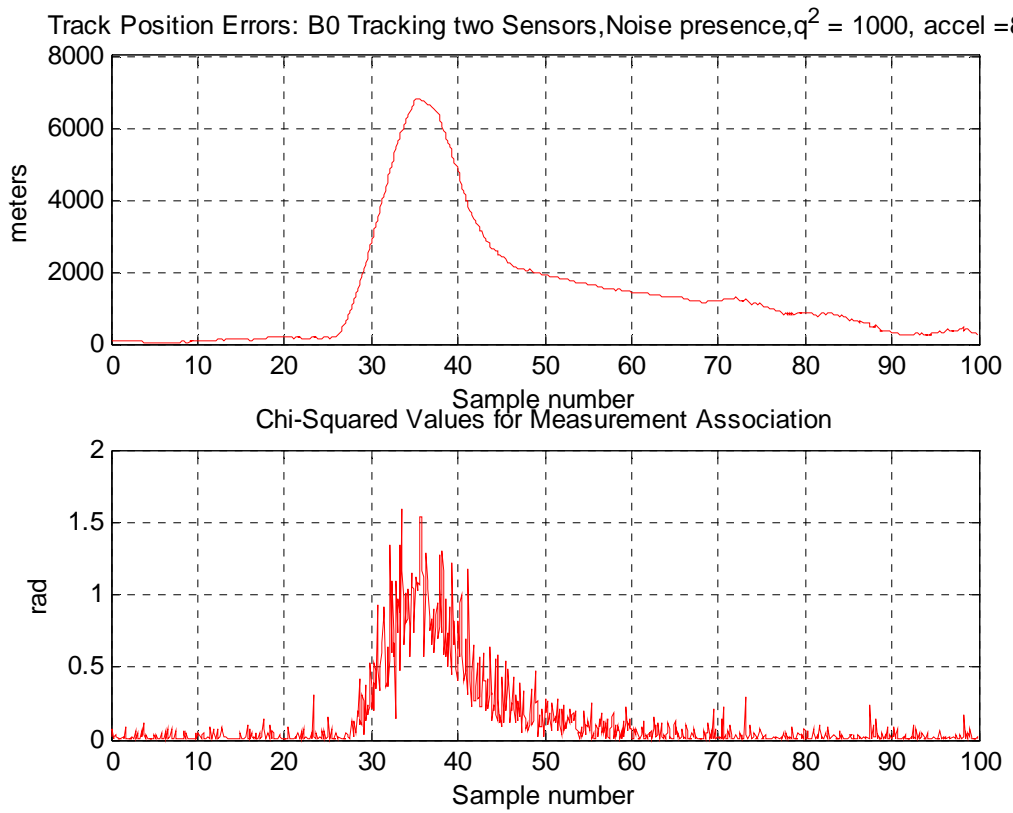
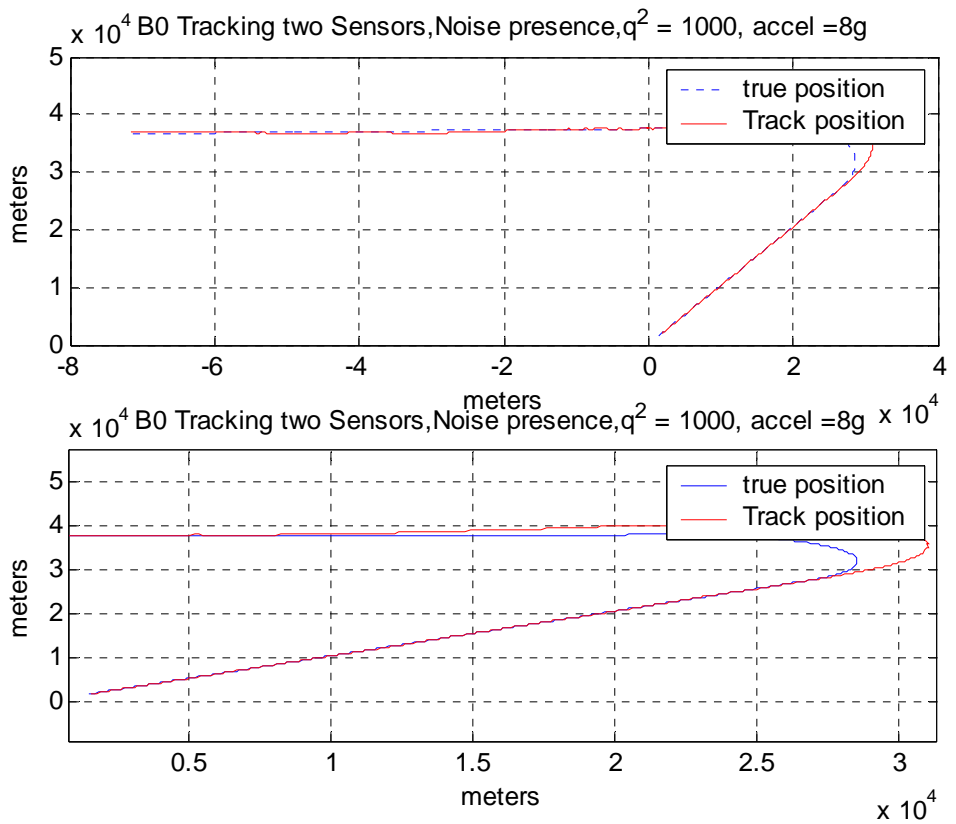












LIST OF REFERENCES

- [1] B.F. Levine, "Quantum well infrared photodetectors", *J. Appl. Phys.*, Vol. 74, No. 8, pp. R1-R61, 1993.
- [2] D.D. Coon and R.P.G. Karunasiri, "New mode of IR detection using quantum wells", *Appl. Phys. Lett.*, Vol. 45, No. 6, pp. 649-651, 1986.
- [3] D. Sarath, J. Gunapala, K. Liu, Jin S. Park, Mani Sundaram, Craig A. Shott, Ted Hoelter, True-Lon Lin, S. T. Massie, Paul D. Maker, Richard E. Muller, and Gabby Sarusi, "9 μ m cutoff 256x256 GaAs/Al_xGa_{1-x}As quantum well infrared photodetector hand-held camera", *IEEE Trans. Electron. Devices*, Vol. 44, pp. 51-57, 1997.
- [4] D. Sarath, J. Gunapala, Sumith V. Bandara, K. Liu, Winn Hong, Mani Sundaram, Paul D. Maker, Richard E. Muller, Craig A. Shott, and Ronald Carralejo, "Long-wavelength 640x486 GaAs/Al_xGa_{1-x}As quantum well infrared photodetector snap-shot camera", *IEEE Trans. Electron. Devices*, Vol. 45, pp. 1890-1897, 1998.
- [5] <http://www.iaf.fraunhofer.de/eng/kk/design-sensor-qwip.htm>, April 2005.
- [6] S. V. Bandara, S. D. Gunapala, D. Z. Y. Ting, S. B. Rafol, and J. K. Liu, "GaAs/AlGaAs multi-quantum-well based far infrared detectors for astronomy application", Jet Propulsion Laboratory, California Institute of Technology, 2001.
- [7] http://www.three-fives.com/latest_features/webzine_features/march05_feature.html, April 2005.
- [8] S. D. Gunapala, S. V. Bandara, J. K. Liu, W. Hong, M. Sundaram, P. D. Maker, R. E. Muller, C. A. Shott, and R. Carralejo, "Quantum well infrared photodetector (QWIP) focal plane arrays", *Infra. Phys. and Technology*, Vol. 45, pp. 197-282, 2000.
- [9] E. Metzbacker, *Quantum Mechanics*, 2nd Edition, ch. 7, Wiley, New York, 1970.
- [10] G. Bastard, E. E. Mendez, L.L Chang and L. Esaki, "Variational calculation on a quantum well in an electric field", *Phys. Rev B*, Vol. 28, No. 6, pp 3241-3245, 1983.
- [11] D. Ahn and S.L. Chuang, "Variational calculation of subbands in a quantum well with a uniform electric field Gram Schmidt: orthogonalization approach", *Appl. Phys Lett.*, Vol. 49, No. 21, pp 1450-1452, 1986.
- [12] J. Singh, "A new method of solving a ground state problem in arbitrary quantum wells: Application to electron hole quasi bound levels in quantum wells under high electric field", *Appl. Phys Lett.*, Vol 48, No. 6, pp. 434-436, 1986.
- [13] K. Hayata, M. Koshiba, K. Nakamura, and A. Shimizu, "Eigenstate calculations of quantum well structures using finite elements", *Electron Lett*, Vol. 24, No. 10, pp. 614-616, 1988.

[14] A. Harwit, J.S. Harris Jr. , and A. Kapitulnic, “Calculated quasi-eigenstates and quasi eigenenergies of quantum well superlattices in an applied electric field”, *J. Appl. Phys.*, Vol. 60, No. 9, pp. 3211-3213, 1986.

[15] A. Erdellyi , *Asymptotic Expansions*, California Institute of Technology.

[16] S. Vatania and G. Gildenblat, “Airy’s function implementation of the transfer matrix method for resonant tunneling in variably spaced finite superlattices”, *IEEE J. Quantum Electronics*, Vol. 32, No. 6, pp. 1093-1105, 1996.

[17] D. Ahn and S.L. Chuang, “Exact calculations of quasi bound states of an isolated quantum well with uniform electric field: Quantum well stark response” *Phys. Rev B*, Vol. 34, No. 12, pp. 9034-9037, 1986

[18] S. Fafard, “Energy levels in quantum wells with capping barrier layer of finite size: Bound states and oscillatory behavior of the continuum states” *Phys. Rev. B*, Vol. 46, No. 8, pp. 4659-4666, 1992.

[19] J. Gallaway, “Optical Absorption in an Electric Field”, *Phys. Rev.*, Vol. 130, No. 2, pp. 549-553, 1962.

[20] L.I. Schiff, *Quantum Mechanics*, Third Edition, pp. 56-58, McGraw-Hill, New York, 1995

[21] W. Trzeciakowski and M. Gurioli “Electric field effects in semiconductor quantum wells” , *Phys. Rev B*, Vol. 44, No. 8, pp. 3880-3890, 1991.

[22] M.P. Touse, G. Karunasiri and K.R. Lantz, “Near and mid-infrared detection using $GaAs / In_xGa_{1-x} / In_yGa_{1-y}As$ multiple step quantum wells”, *Appl. Phys. Lett.*, Vol. 86, pp. 093501/1 – 093501/3, 2005.

[23] K.K. Choi, *The Physics of Quantum Well Infrared Photodetectors*, Vol. 7, pp. 18-19, World Scientific, 1997.

[24] John S. Townsend, “A Modern Approach to Quantum Mechanics”, pp. 425-430, University Science Books, Sausalito CA, 2000.

[25] K.R. Lantz, *Two color photodetector using an asymmetric quantum well structure*, Master’s thesis, Naval Postgraduate School, Monterey California, 2002.

[26] M.P. Touse, *Demonstration of a near and mid infrared detector using multiple step quantum wells*, Master’s thesis, Naval Postgraduate School, Monterey California, 2003.

[27] Yeo Hwee Tiong, *High responsivity tunable step quantum well infrared photodetector*, Master’s thesis, Naval Postgraduate School, Monterey California, 2004.

[28] M. Abramowitz and I. Stegun, *Handbook of Mathematical Functions*, p. 446, U.S Government Printing Office, 1964.

[28] Yaakov Bar-Shalom and Xiao-Rong Li, *Estimation with Applications to Tracking and Navigation*, pp 161-177, Wiley-Interscience, New York, 2001.

[29] Branko Ristic, Sanjeev Arulampalam, and Neil Gordon, *Beyond the Kalman Filter: Particle Filters for Tracking Applications*, pp. 103-151, Artech House, Boston MA, 2004.

[30] R.G. Hutchins, Notes for EC3310 (Optimal Estimation), Naval Postgraduate School, Monterey CA, 2002 (unpublished).

[31] Volkan Cevher and James H. McClellan, "Sensor Array Calibration via Tracking with the Extended Kalman Filter", CSIP, School of ECE, Georgia Tech, Atlanta, GA 30332-0250

[32] <http://www.public.asu.edu/~achhetri/files>, April 2005

[33] G.N. Watson, *Theory of Bessel Functions*, Cambridge Univ. Press, 1922

THIS PAGE INTENTIONALLY LEFT BLANK

INITIAL DISTRIBUTION LIST

1. Defense Technical Information Center
Ft. Belvoir, Virginia
2. Dudley Knox Library
Naval Postgraduate School
Monterey, California
3. Chairman, Department of Physics, Code PH/Lu
Naval Postgraduate School
Monterey, California
4. Chairman, Department of Electrical and Computer Engineering, Code EC
Naval Postgraduate School
Monterey, California
5. Professor Gamani Karunasiri
Department of Physics
Naval Postgraduate School
Monterey, California
6. Professor James Luscombe
Department of Physics
Naval Postgraduate School
Monterey, California
7. Professor Robert Hutchins
Department of Electrical and Computer Engineering
Naval Postgraduate School
Monterey, California
8. Professor John Powers
Department of Electrical and Computer Engineering
Naval Postgraduate School
Monterey, California
9. Embassy of Greece, Naval Attaché
Washington, DC
10. Eftychios Psarakis
192 Kydonias st. Chania Crete
73100, Greece